EFFECTS OF STRESS PATH ON TRIAXIAL STRENGTH

AND ELASTICITY OF MAHA SARAKHAM SALT

Kiattisak Artkhonghan

A Thesis Submitted in Partial Fulfillment of the Requirements for the

Degree of Doctor of Philosophy of Engineering in Geotechnology

Suranaree University of Technology

Academic Year 2014

ผลกระทบของวิถีความเค้นต่อความแข็งและความยืดหยุ่นในสามแกน
ของเกลือหินชุดมหาสารคาม

นายเกียรติศักดิ์ อาจคงหาญ

วิทยานิพนธ์นี้เป็นส่วนหนึ่งของการศึกษาตามหลักสูตรปริญญาวิศวกรรมศาสตรดุษฎีบัณฑิต

สาขาวิชาเทคโนโลยีธรณี

มหาวิทยาลัยเทคโนโลยีสุรนารี

ปีการศึกษา 2557

EFFECTS OF STRESS PATH ON TRIAXIAL STRENGTH AND

ELASTICITY OF MAHA SARAKHAM SALT

Suranaree University of Technology has approved this thesis submitted in partial fulfillment of the requirements for the Degree of Doctor of Philosophy.

Thesis Examining Committee

_____

(Dr. Prachya Tepnarong)

Chairperson

_____

(Prof. Dr. Kittitep Fuenkajorn)

Member (Thesis Advisor)

_____

(Dr. Decho Phueakphum)

Member

_____

(Dr. Anisong Chitnarin)

Member

_____

(Assoc. Prof. Ladda Wannakao)

Member

_____   _____

(Prof. Dr. Sukit Limpijumnong)   (Assoc. Prof. Flt. Lt. Dr. Kontorn Chamniprasart)

Vice Rector for Academic Affairs   Dean of Institute of Engineering

and Innovation

เกียรติศักดิ์ อาจคงหาญ : ผลกระทบของวิถีความเค้นต่อความแข็งและความยืดหยุ่นในสาม
แกนของเกลือหินชุดมหาสารคาม (EFFECTS OF STRESS PATH ON TRIAXIAL
STRENGTH AND ELASTICITY OF MAHA SARAKHAM SALT) อาจารย์ที่ปรึกษา :
ศาสตราจารย์ ดร.กิตติเทพ เฟื่องขจร, 118 หน้า.

วัตถุประสงค์ของการศึกษานี้คือเพื่อหาค่ากำลังกดและความยืดหยุ่นของเกลือหินภายใต้วิถี
ความเค้นที่แตกต่างกันในห้องปฏิบัติการ โดยโครงกดทดสอบในสามแกนจริง ระบบการทดสอบมี
สามคุณลักษณะคือ สภาวะการกดในสามแกน สภาวะการกดในหลายแกน และสภาวะการดึงใน
สามแกน ภายใต้ความดันล้อมรอบที่คงที่และค่าเฉลี่ยของความเค้นที่คงที่ ระผลการทดสอบระบุว่า
ค่ากำลังกดในสามแกนเพิ่มขึ้นเชิงเส้นตรงกับค่าเฉลี่ยของความเค้นสำหรับวิถีความเค้นทุกชนิด ค่า
กำลังกดของเกลือหินภายใต้ความเค้นเฉลี่ยคงที่จะต่ำกว่าค่ากำลังกดภายใต้ความดันล้อมรอบที่คงที่
เสมอ ภายใต้ความเค้นเฉลี่ยที่เท่ากัน ค่ากำลังเฉือนที่ได้จากการกดในสามแกนจะมีค่าสูงสุด ในขณะ
ที่การทดสอบแบบดึงในสามแกนจะให้ค่าน้อยที่สุด ซึ่งลักษณะนี้จะเป็นจริงในสภาวะความเค้น
ล้อมรอบคงที่และความเค้นเฉลี่ยคงที่ เกณฑ์การแตกสองเกณฑ์ได้นำเสนอคือ เกณฑ์การแตกที่
พัฒนาจากค่ากำลังเฉือนในสามแกน และเกณฑ์การแตกที่พัฒนาจากพลังงานความเครียดเบี่ยงเบน
ผลที่ได้ระบุว่า เกณฑ์พลังงานความเครียดเบี่ยงเบนที่จุดบวมตัวของเกลือภายใต้ความเค้นเฉลี่ยคงที่
จะให้ค่าในเชิงอนุรักษ์มากที่สุด เนื่องจากเกณฑ์นี้พิจารณาทั้งความเค้นและความเครียดในเกลือหิน
การศึกษานี้ได้สาธิตการนำเกณฑ์การแตกทั้งสอง ไปประยุกต์ใช้ เพื่อกำหนดความดันต่ำสุดที่
ปลอดภัยของโพลงเกลือที่ใช้กักเก็บพลังงานอากาศอัด ปิโตรเลียมเหลว และก๊าซธรรมชาติ

สาขาวิชา เทคโนโลยีธรณี   ลายมือชื่อนักศึกษา _____

ปีการศึกษา 2557   ลายมือชื่ออาจารย์ที่ปรึกษา _____

KIATTISAK ARTKHONGHAN : EFFECTS OF STESS PATH ON
TRIAXIAL STRENGTH AND ELASTICITY OF MAHA SARAKHAM
SALT. THESIS ADVISOR : PROF. KITTITEP FUENKAJORN, Ph.D.,
P.E., 118 PP.

STRESS PATH/COMPRESSION/POLYAXIAL/EXTENSION/STRAIN ENERGY

The objective of this study is determine compressive strength and stiffness of rock salt under different stress paths in the laboratory using a true triaxial load frame. The test schemes are triaxial compression, polyaxial compression and triaxial extension with constant σ_3 and constant σ_m conditions. The results indicate that the octahedral shear strength linearly increases with the mean stress for all stress paths. The salt strengths under constant σ_m are always lower than those under constant σ_3 condition. Under the same mean stress, the octahedral shear strengths obtained from triaxial compression are largest while the triaxial extension yields the lowest values. This is true for both under constant σ_3 and constant σ_m conditions. Two empirical strength criteria are proposed: octahedral shear strength and distortional strain energy criteria. The distortional strain energy at dilation with constant σ_m is the most conservative, as it considers both stresses and strains of the salt. It is demonstrated here that the proposed criteria can be applied to determine the safe minimum storage (cushion) pressure of the CAES, LPG and natural gas caverns in salt mass.

School of   Geotechnology   Student's Signature_____

Academic Year 2014   Advisor's Signature_____

ACKNOWLEDGMENTS

I would like to express my sincere thanks to Prof. Dr. Kittitep Fuenkajorn for his valuable guidance and efficient supervision. I appreciate his strong support, encouragement, suggestions and comments during the research period. My heartiness thanks are also extended to Dr. Prachya Tepnarong, Dr. Decho Phueakphum, Dr. Anisong Chitnarin, and Assoc. Prof. Ladda Wannakao, who served on the thesis committee and commented on the manuscript. Grateful thanks are given to all staffs of Geomechanics Research Unit, Institute of Engineering who supported my work.

Finally, I would like to thank beloved parents for their love, support and encouragement.

Kiattisak Artkhonghan

TABLE OF CONTENTS

TABLE OF CONTENTS (Continued)

TABLE OF CONTENTS (Continued)

TABLE OF CONTENTS (Continued)

LIST OF TABLES

LIST OF TABLES (Continued)

LIST OF FIGURES

LIST OF FIGURES (Continued)

LIST OF FIGURES (Continued)

LIST OF FIGURES (Continued)

LIST OF FIGURES (Continued)

LIST OF FIGURES (Continued)

SYMBOLS AND ABBREVIATIONS

σ_1 =   Compressive strength at failure

σ_2 =   Intermediate stress

σ_3 =   Minor principal stress

σ_m =   Mean stress

τ_{oct} =   Octahedral shear stresses

γ_{oct} =   Octahedral shear strain

$\tau_{oct,f}$ =   Octahedral shear stresses at failure

$\tau_{oct,d}$ =   Octahedral shear stresses at dilation

$\sigma_{m,d}$ =   Mean stress at dilation

$\varepsilon_{v,e}$ =   Volumetric strain at dilation

G =   Shear modulus

λ =   Lime's constant

K =   Bulk modulus

E =   Young modulus

ν =   Poisson's ratio

E_1 =   Elastic moduli along the major directions

E_2 =   Elastic moduli along directions

E_3 =   Elastic moduli along minor directions

ε_1 =   Major principal strains

ε_2 =   Intermediate principal strains

SYMBOLS AND ABBREVIATIONS (Continued)

ε_3	=	Minor principal strains
σ_c	=	Uniaxial compressive strength
μ	**=**	Lode parameter
A	=	Empirical constant for equation (6.2)
B	=	Empirical constant for equation (6.2)
A$'$	=	Empirical constant for equation (6.3)
B$'$	=	Empirical constant for equation (6.3)
α	=	Empirical constant for equation (6.4)
β	=	Empirical constant for equation (6.4)
α'	=	Empirical constant for equation (6.5)
β'	=	Empirical constant for equation (6.5)
α_1	=	Empirical constant for equation (6.6)
α_2	=	Empirical constant for equation (6.6)
α'_1	=	Empirical constant for equation (6.7)
α'_2	=	Empirical constant for equation (6.7)
β_1	=	Empirical constant for equation (6.8)
β_2	=	Empirical constant for equation (6.8)
β'_1	=	Empirical constant for equation (6.9)
β'_2	=	Empirical constant for equation (6.9)
W_d	=	Distortional strain energy density
$W_{d,d}$	=	Distortional strain energy density at dilation

SYMBOLS AND ABBREVIATIONS (Continued)

W_m	=	Mean strain energy density
C	=	Empirical constant for equation (6.16)
D	=	Empirical constant for equation (6.16)
C'	=	Empirical constant for equation (6.17)
D'	=	Empirical constant for equation (6.17)
χ	=	Empirical constant for equation (6.18)
ω	=	Empirical constant for equation (6.18)
χ'	=	Empirical constant for equation (6.19)
ω'	=	Empirical constant for equation (6.19)
χ_1	=	Empirical constant for equation (6.20)
χ_2	=	Empirical constant for equation (6.20)
χ'_1	=	Empirical constant for equation (6.21)
χ'_2	=	Empirical constant for equation (6.21)
ω_1	=	Empirical constant for equation (6.22)
ω_2	=	Empirical constant for equation (6.22)
ω'_1	=	Empirical constant for equation (6.23)
ω'_2	=	Empirical constant for equation (6.23)

CHAPTER I

INTRODUCTION

1.1 Background and rationale

The reliable strength estimation of a rock salt is necessary to develop safe and economical designs for solution mining, cavern air energy storage and underground salt mining. Rock salt is an inhomogeneous and anisotropic material with complex behavior. The effects of confining pressures at great depths on the mechanical properties of rocks are commonly simulated in a laboratory by performing triaxial compression testing. A significant limitation of these conventional methods is that the mean stress is not constant during the test. The actual in-situ rock is normally subjected to an anisotropic stress state where the maximum, intermediate and minimum principal stresses are different ($\sigma_1 \neq \sigma_2 \neq \sigma_3$) and mean stress of this condition is always constant. It has been commonly found that compressive strengths obtained from conventional polyaxial load frame or true triaxial load frame can represent the actual in-situ strength where the rock is subjected to an anisotropic stress state.

1.2 Research objectives

The objectives of this study are as follows.

1. Study the mechanism of rock salt specimen under anisotropic stress states.

2. Develop the failure criterion of the rock salt that can be readily applied in the design and stability analysis of geological engineering underground structures.

3. Simulate the storage caverns to demonstrate the effect of anisotropic stresses.to develop two failure criterions of the rocks that can be readily applied in the design and the stability analysis of geologic structures.

1.3 Research methodology

The research methodology shown in Figure 1.1 comprises 6 steps: literature review, sample collection and preparation, design and develop true triaxial testing device, laboratory experiments, data analysis, development of mathematical relations, and thesis writing and presentation.

1.3.1 Literature review

Literature review are carried out to study the previous research on compressive strength in triaxial and polyaxial states, the effect of intermediate principal stress on rock failure, rock deformation and strength in triaxial stress state, conventional stress state and true triaxial stress state. The sources of information are from text books, journals, technical reports and conference papers. A summary of the literature review are given in the thesis.

1.3.2 Sample preparation

Rock samples used here have been obtained from the Middle member of the Maha Sarakham formation in the northeastern Thailand. The rock salt is relatively pure halite. Sample preparation is carried out in the laboratory at Suranaree University of Technology. Samples prepared for compressive strength test are $4.4 \times 4.4 \times 8.8$ cm^3.
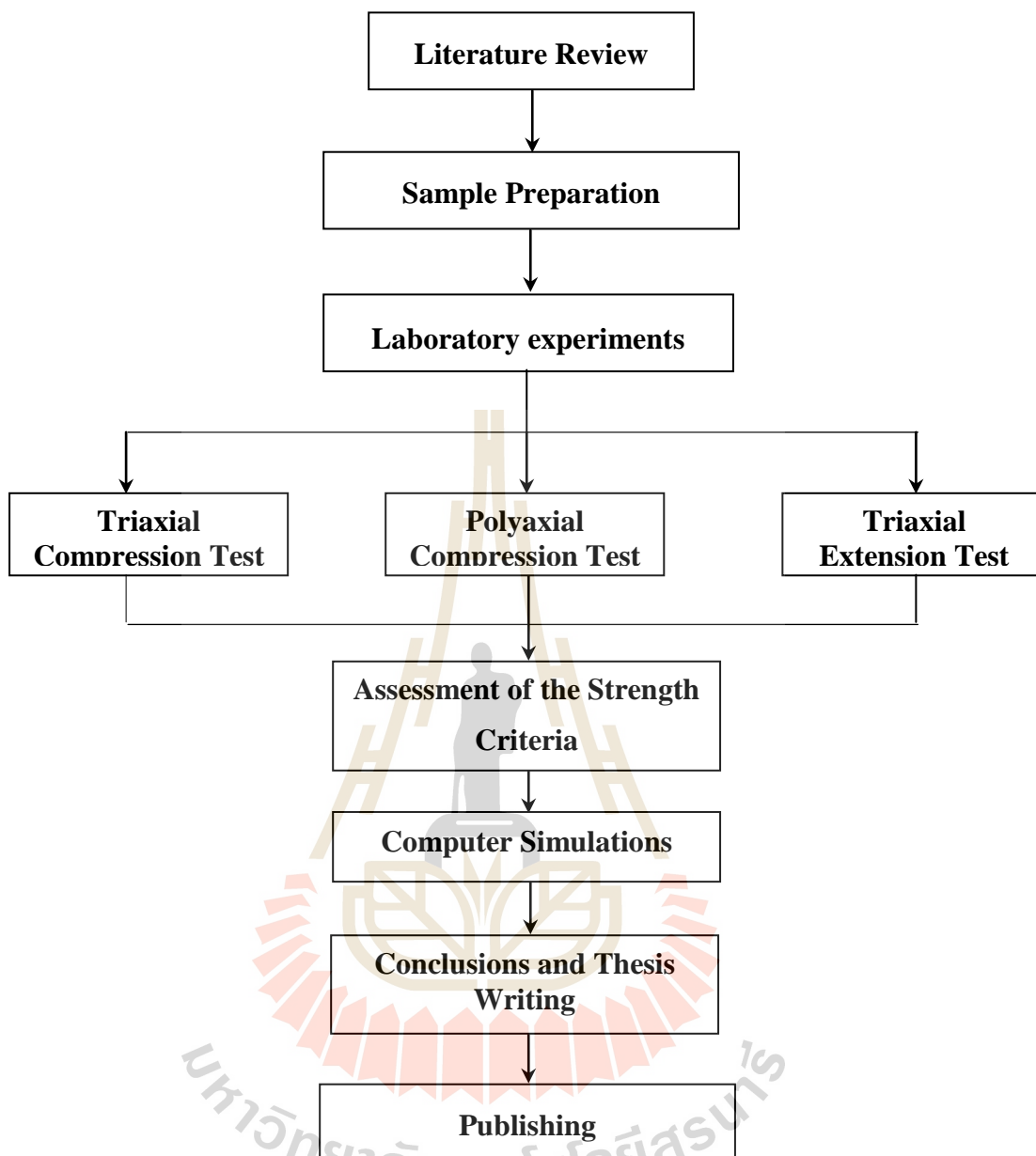
Figure 1.1 Research methodology.

1.3.3 Laboratory experiments

The laboratory experiments include conventional triaxial and polyaxial compressive strength tests. The testing performed to determine the strength and deformation of rock salt subjected to different stresses paths. A true triaxial load frame (Figure 1.2) is used to apply pressures between 20 MPa to 50 MPa. The elastic modulus and compressive strength are investigate. Neoprene sheets are used to minimize the friction at all interfaces between the loading plate and the rock surface. All test results are used to develop failure criterion of the rocks.

1.3.4 Assessment of the Strength Criteria

Results from laboratory measurements in terms of the principal stresses at failure and dilation are used to formulate mathematical relations. The studied strength include strain energy density criteria and octahedral shear stress and mean stress relation.

1.3.5 Computer Simulations

The failure criterion is used to assess the stability of an underground storage cavern by using the finite difference code (FLAC). The multi-axial strength criterion, calibrated from the true triaxial strength test results and the conventional approach of using the uniaxial and triaxial strength test data are used to simulate the stability conditions of the storage cavern.

1.3.6 Conclusions and Thesis Writing

All research activities, methods, and results are documented and complied in the thesis. The research or findings is published in the conference proceedings or journals.

1.4   Scope and limitations

The scope and limitations of the research include as follows.

1. Laboratory testing will be conducted on specimens prepared from the Maha Sarakham salt.

2. The samples were dry-cut to obtain rectangular blocks with normal dimensions of about 4.4×4.4×8.8 cm.

3. Testing will be performed with constant mean stresses.

4. The testing will be divided into three conditions, triaxial compression test ($\sigma_1 \neq \sigma_2 = \sigma_3$), true triaxial compression test ($\sigma_1 \neq \sigma_2 \neq \sigma_3$), and triaxial extension test ($\sigma_1 = \sigma_2 \neq \sigma_3$).

5. All tests will be conducted under ambient temperature and dry condition.

6. No field testing will be conducted.

7. The research findings will be published in conference paper or journal.

1.5   Thesis contents

This research thesis is divided into six chapters. The first chapter includes background and rationale, research objectives, research methodology, and scope and limitations. **Chapter II** presents results of the literature review to improve an understanding of rock compressive strength as affected by the intermediate principal stress. **Chapter III** describes sample collection and preparation. **Chapter IV** describes the laboratory testing; triaxial compression, triaxial extension, and polyaxial compression test. **Chapter V** presents test results. **Chapter VI** is results analysis and strength criteria. **Chapter VII** is computer simulation. **Chapter VIII** is discussions,

conclusions and future studies.   **Appendix A** provides detailed of technical publications.
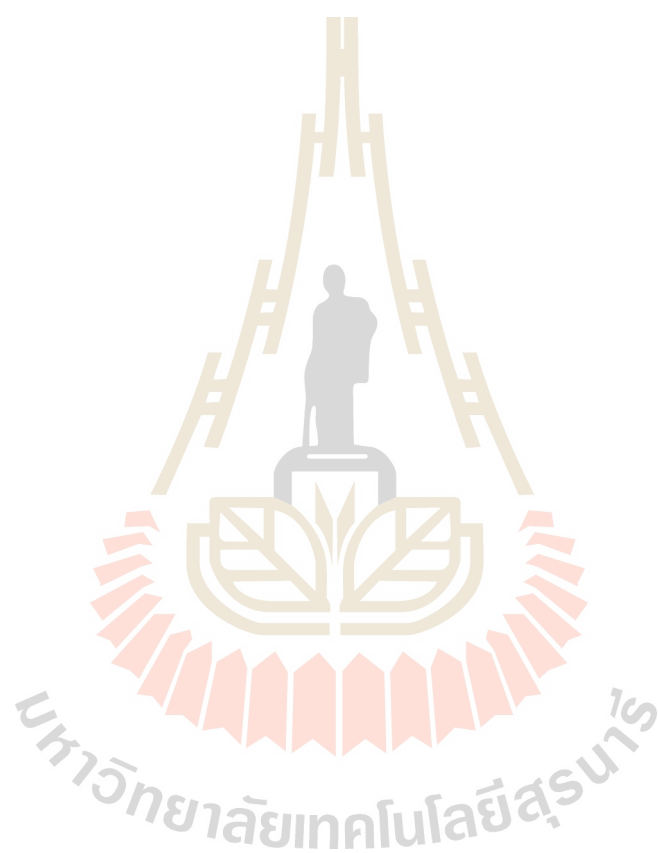
CHAPTER II

LITERATURE REVIEW

2.1 Introduction

Relevant topics and previous research results are reviewed to improve an understanding of rock compressive strength in triaxial and polyaxial compression tests. This review also includes the investigation of the effects of stress path and intermediate principal stress on rock strengths, some polyaxial compression.

2.2 Laboratory testing on rock salt

Mellegard et al. (2007) were studied in effect of the Lode angle on the creep of salt. The steady-state creep rate of salt is typically described using only the maximum and minimum principal stresses and is generally considered to be independent of the intermediate principal stress; thus, the steady-state creep rate of salt is expected to be the same under both compressive and extensile states of stress. However, little experimental evidence has been obtained regarding the transient nature of salt under alternating states of stress between triaxial compression and triaxial extension; i.e. alternating Lode angles. Multistage creep tests were performed to investigate the time-dependent behavior of salt at two Lode angles. The data show that Lode angle does not affect the steady-state strain rate of salt; however, each time the Lode angle was changed, a significant transient response was observed. This transient response to changes in Lode angle

is not predicted by constitutive models commonly used to evaluate natural gas storage caverns.

The value of the intermediate principal stress (represented here by the Lode angle) does not have a significant effect on the steady-state strain rates exhibited by salt. However, a change in the Lode angle does affect the transient behavior of salt. The test results presented here provide insight into the role of the intermediate principal stress as it relates to the creep and hardening of salt. Creep constitutive model development or review should be considered to assess the best way of incorporating Lode angle effects into those models. The numerical simulations and laboratory tests presented here provide a thought-provoking topic and further illustrate the complex behavior of salt. Additional experimental and microstructural studies are likely to provide the key to explain the intriguing behavior exhibited by these laboratory tests. An area where accurate prediction of this uncharacterized behavior of salt could have an impact is geomechanical modeling of natural gas storage caverns. Previous cavern evaluations have shown that the state of stress in the salt changes from triaxial compression to triaxial extension, depending on the pressure in the cavern. The significance of this behavior is a topic for future research.

Walsri et al. (2009) developed polyaxial load frame (Figure 2.1) to determine the compressive and tensile strengths of three types of sandstone under true triaxial stresses. Results from the polyaxial compression tests on rectangular specimens of sandstones suggest that the rocks are transversely isotropic. The measured elastic modulus in the direction parallel to the bedding planes is slightly greater than that normal to the bed. Poisson's ratio on the plane normal to the
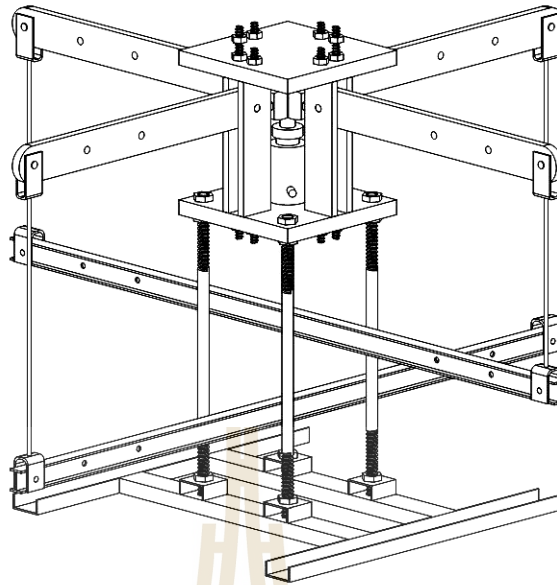
Figure 2.1 Polyaxial load frame developed for rock testing under true triaxial stresses (Walsri et al., 2009).

bedding planes is lower than those on the parallel ones. Under the same σ_3, σ_1 at failure increases with σ_2. Results from the Brazilian tension tests under axial compression reveal the effects of the intermediate principal stress on the rock tensile strength. The Coulomb and modified Wiebols and Cook failure criteria derived from the characterization test results predict the sandstone strengths in term of $J_2^{1/2}$ as a function of J_1 under true triaxial stresses. The modified Wiebols and Cook criterion describes the failure stresses better than does the Coulomb criterion when all principal stresses are in compressions. When the minimum principal stresses are in tension, the Coulomb criterion over-estimate the second order of the stress invariant at failure by about 20% while the modified Wiebols and Cook criterion fails to describe the rock tensile strengths.

Sriapai et al. (2011) have used polyaxial load frame to determine true triaxial compressive strength of Maha Sarakham (MS) salt. The load frame equipped with two pairs of cantilever beam is used to apply the constant lateral stress (σ_2 and σ_3) to salt specimen while the axial stress (σ_1) is increased at 0.5-1.0 MPa/s until failure occurs. The deformations induced along the three loading directions are monitored and used to calculate the tangent elastic modulus and Poisson's ratio of the salt. For the Coulomb criterion the internal friction angle determined from the triaxial loading condition ($\sigma_2 = \sigma_3$). The effect σ_2 of on the salt strengths can be best described by the modified Wiebols and Cook criterion. The empirical (power law) Mogi criterion tends to underestimate the salt strengths particularly under high σ_3 values. The modified Lade criterion overestimates the actual strengths at all levels of σ_3. The Coulomb and Hoek and Brown criteria cannot describe the salt strengths beyond the condition where $\sigma_2 = \sigma_3$, as they cannot incorporate the effects of σ_2. Both circumscribed and inscribed Drucker-Prager criteria severely underestimate σ_1 at failure for all stress conditions.

Sriapai et al. (2012) used the strain energy density criterion to describe the salt strength and deformability under different temperatures. It is assumed that under a given mean strain energy and temperature the distortional strain energy required to fail the salt specimens is constant. Regression on the test results shows that the distortional strain energy (W_d) increases linearly with the mean strain energy (W_m). It is interesting to note that the rates of the increase of W_d with respect to W_m are virtually the same for all temperature levels.

Fuenkajorn et al. (2012) were proposed empirical strength criteria base on the strain energy density principle of rock salt. Uniaxial and triaxial compression tests

have been performed to assess the influence of loading rate on the compressive strength and deformability of the Maha Sarakham alt. The salt specimens with a nominal dimension of 5.4×5.4×5.4 cm3 are compressed to failure using a polyaxial load frame. The lateral confining pressures are maintained constant at 0, 3, 7, 12, 20 and 28 MPa while the axial stresses are increased at onstant rates of 0.001, 0.01, 0.1, 1.0 and 10 MPa/s until failure occurs. The salt elasticity and strength increase with the loading rates. The elastic (tangent) modulus determined at about 40% of the failure stress varies from 15 to 25 GPa, and the Poisson's ratio from 0.23 to 0.43. The elastic parameters tend to be independent of the confining pressures. The strains induced at failure decrease as the loading rate increases. Various multiaxial formulations of loading rate dependent strength and deformability are derived. The variation of the octahedral shear stresses and strains induced at dilation and at failure with the applied shear stress rates can be best described by power relations. The distortional strain energy at dilation and at failure from various loading rates varies linearly with the mean normal stress. The proposed empirical criteria are applied to determine the safe maximum withdrawal rate of a compressed-air energy storage cavern in the Maha Sarakham salt formation. The strain energy criterion that considers both distortional and mean stress–strains at dilation tends to give the most conservative results.

Sartkaew and Fuenkajorn (2013) have been performed the uniaxial compression test to assess the effects of loading rate on compressive strength and deformability of the Maha Sarakham salt under temperatures ranging from 273 to 373 Kelvin. The variation of the octahedral shear strength with the stress rates and temperatures can be described by logarithmic relations. The distortion strain energy criterion is proposed to describe the salt strength under varied stress rates

and temperatures. The criterion can be used to determine the stability of salt around compressed-air energy storage caverns, where the loading rates and temperatures are continuously varied during air injection and retrieval periods.

The testing is assumed to be under isothermal conditions (constant temperature with time during loading). The decrease of the salt strength as the temperature increases suggests that the applied thermal energy before the mechanical testing makes the salt weaker, and more plastic, failing at lower stress and higher strain with lower elastic and shear moduli.

2.3   Polyaxial compressive strength tests

Wiebols and Cook (1968) investigate the effect of σ_2 on rock strength, based on the earlier testing results. Early attempts to examine the influence of σ_2 on rock strength were made in 1960s by Murrell (1963) and Handin et al. (1967). They compared the results from a series of triaxial tests conducted in marble, limestone, dolomite, and glass [triaxial compression tests ($\sigma_1 > \sigma_2 = \sigma_3$) and triaxial extension test ($\sigma_1 = \sigma_2 > \sigma_3$)] and noted that the rock strength for any given σ_3 was larger in triaxial extension than in triaxial compression, thus suggesting that the intermediate principal stress does, in fact, affect mechanical properties (Figure 2.2). Handin and coworkers carried out several triaxial compression and triaxial extension tests in Solenhofen limestone, Blaire dolomite and Pyrex glass. They obtained results similar to those of Murrell's showing that rock strength was higher when the larger intermediate principal stress ($\sigma_2 = \sigma_1$) was applied (Figure 2.3). Based on these earlier experimental results, Wiebols and Cook pursued a theoretical approach to further investigate the effect of σ_2 on rock strength. They
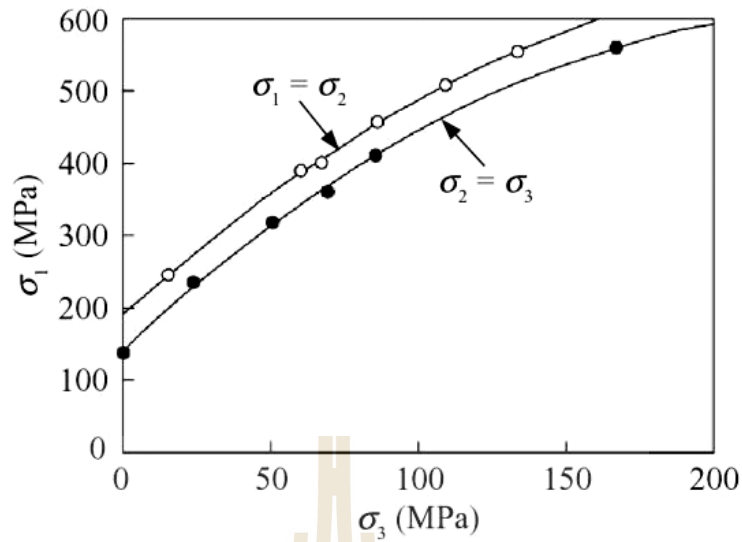
Figure 2.2 Strtength differences between Carrara marble specimens tested under conventional triaxial compression and those under conventional triaxial extension (Wiebols and Cook, 1968).
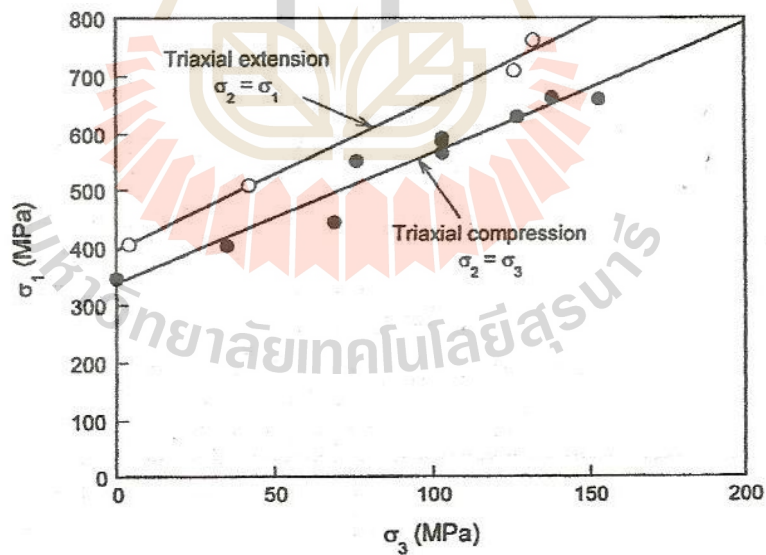
Figure 2.3 Strength differences between Solenhofen limestone specimens tested under conventional triaxial compression and those under conventional extension (Wiebols and Cook, 1968).

derived a strength criterion based on the strain energy stored by the rock in the absence of discontinuities, and the additional strain energy around Griffith cracks as a result of sliding of crack surfaces over each other. They found that under true triaxial (polyaxial) compressive stress conditions the intermediate principal stress has a pronounced effect, predictable if the coefficient of sliding friction between crack surfaces is known. In particular, Wiebols and Cook determined from their model that if σ_3 is held constant and σ_2 is increased from $\sigma_2 = \sigma_3$ to $\sigma_2 = \sigma_1$ the strength first increases, reaches a maximum at some value of σ_2 and then decreases to a level higher than that obtained in a triaxial test, i.e. when $\sigma_2 = \sigma_3$ (Figure 2.4).
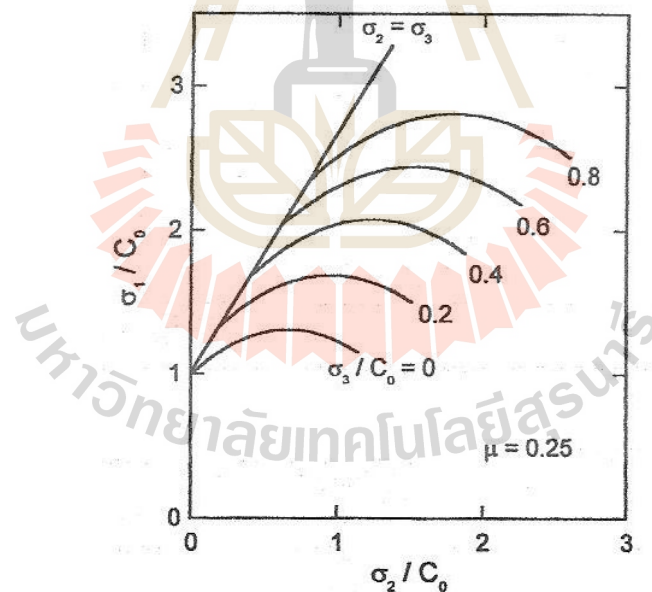
Figure 2.4 Normalized compressive strength of σ_1/c_0 plotted as a function of σ_2/c_0, for various values of σ_3/c_0 (Wiebols and Cook, 1968).

Wawersik et al. (1997) develop the true-triaxial apparatus (Figure 2.5) that makes use of conventional triaxial pressure vessels in combination with specially configured, high-pressure hydraulic jacks inside these vessels. The development combines advantages not found in existing facilities, including a compact design, pore-pressure and flow-through capabilities, the ability to attain high principal stresses and principal stress differences, direct access to parts of the sample, and provisions to relatively large deformations without developing serious stress field in homogeneities.

Colmenares and Zoback (2002) examine seven different failure criteria by comparing them to published polyaxial test data ($\sigma_1 \neq \sigma_2 \neq \sigma_3$) for five different rock types at a variety of stress states. A grid search algorithm was employed to find the best set of parameters that describe failure for each criterion and the associated misfit. Overall, the polyaxial criteria Modified Wiebols and Cook and Modified Lade achieved a good fit to most of the test data. And this is especially true for the rocks with a highly σ_2 – dependent failure behavior (e.g. Dunham dolomite, Solenhofen limestone). However, for some rock types (e.g. Shirahama sandstone, Yuubari shale), the intermediate stress hardly affects failure and the Mohr-Coulomb and Hoek and Brown criteria fit these test data equally well or even better than the more complicated polyaxial criteria. The details of the failure criteria that are referred above to provide a good fit for different rock types are below.

Hoek and Brown criterion

$$\sigma_1 = \sigma_3 + C_0 \, (m\sigma_3 / c_0 + s)^{1/2} \tag{2.1}$$
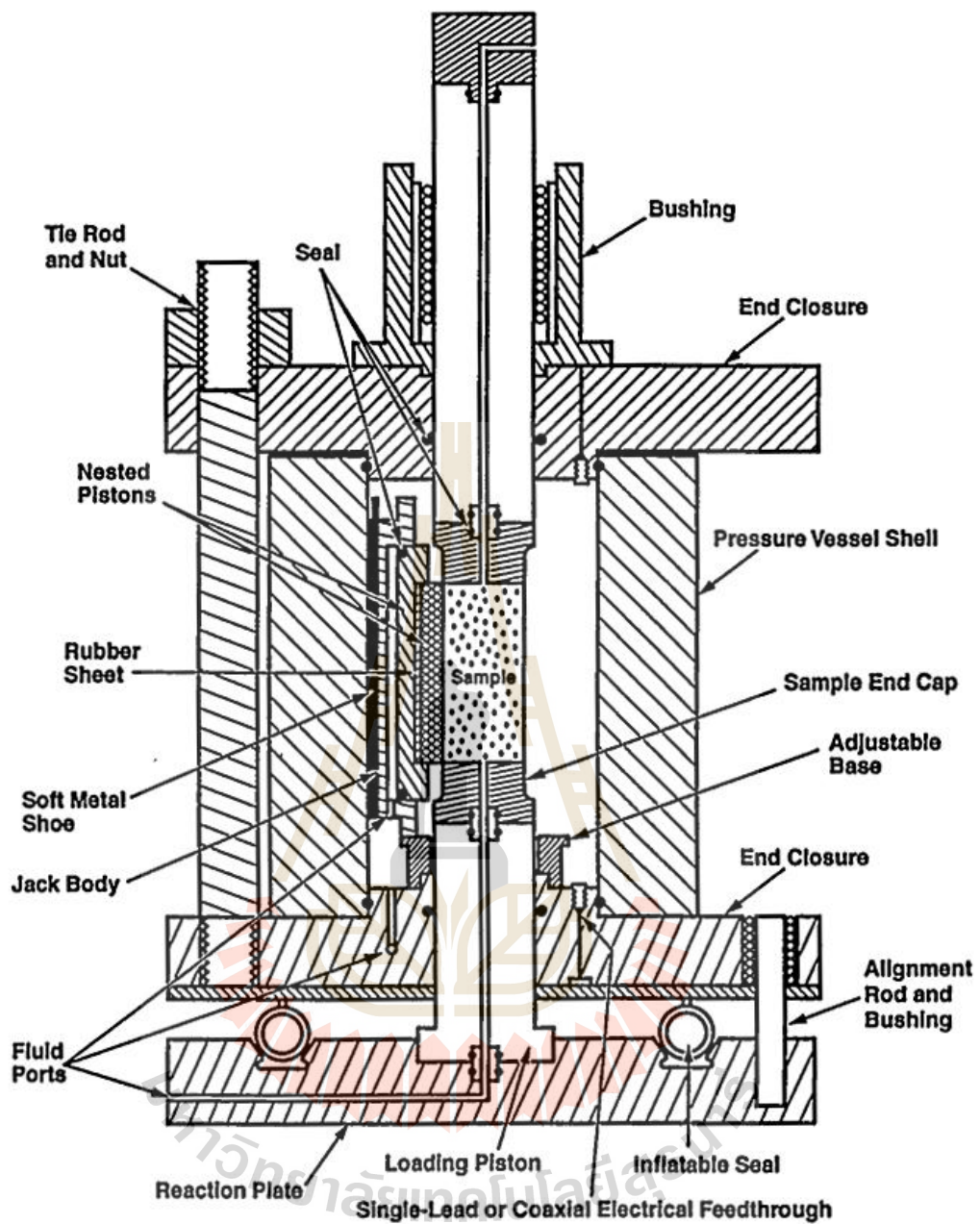
Figure 2.5 Sandia true-triaxial testing system with "floating" pressure vessel shell (Wawersik et al., 1997).

where σ_1 = major principal stress at failure

σ_3 = least principal stress at failure

C_0 = uniaxial compressive strength

m and s are dimensionless strength parameters (m depends on rock type and s depends on the characteristics of rock mass).

Ranges of m-values for some characteristic rock types are as follows.

5<m<8 = Carbonate rocks with well-developed crystal cleavage (dolomite, limestone, marble)

4<m<10 = Lithified argillaceous rocks (mudstone,siltstone, shale, slate)

15<m<24 = Arenaceous rocks with strong crystals and poorly developed crystal cleavage (sandstone, quartzite)

16<m<19 = Fine-grained polyminerallic igneous crystalline rocks (andesite, dolerite, diabase, rhyolite)

22<m<33 = Coarse-grained polyminerallic igneous and metamorphic rocks (amphibolite, gabbro, gneiss, granite, norite, quartz-diorite)

For the parameters:

s = 1 for intact rock

s = 0 for a completely granulated specimen or a rock aggregate

Mohr-Coulomb criterion

$$\tau = S_0 + \mu\sigma_n \qquad\qquad (2.2)$$

where τ = shear stress

S_0 = shear strength or cohesion

μ = coefficient of internal friction of the material

σ_n = normal stress

Another linearized form of Mohr-Coulomb to be written:

$$\sigma_1 = C_0 + q\sigma_3 \qquad (2.3)$$

where σ_1 = major principal stress at failure

σ_3 = least principal stress at failure

C_0 = uniaxial compressive strength

q = $[(\mu^2 + 1)^{1/2} + \mu]^2 = \tan^2(\pi/4 + \phi/2)$

(Assume: σ_2 has no influence on failure)

Modified Lade criterion

$$(I_1')^3 / I_3' = 27 + \eta \qquad (2.4)$$

where I_1' = $(\sigma_1+S)+(\sigma_2+S)+(\sigma_3+S)$

I_3' = $(\sigma_1+S)(\sigma_2+S)(\sigma_3+S)$

S = $S_0 / \tan\phi$

η = $4(\tan\phi)^2 (9\ 7\sin\phi) / (1-\sin\phi)$

$\tan\phi = \mu$

S_0 = $C_0 / (2q^{1/2})$ and

q = $[(\mu^2 + 1)^{1/2} + \mu]^2 = \tan^2(\pi/4 + \phi/2)$

(S and η are material constants: S related to cohesion of rock; η representing the internal friction)

Modified Wiebols and Cook criterion

$$J_2^{\frac{1}{2}} = A + BJ_1 + C J_1^2 \qquad\qquad (2.5)$$

where J_1 = $(1/3)\cdot(\sigma_1+\sigma_2+\sigma_3)$

$J_2^{\frac{1}{2}}$ = $[1/6 ((\sigma_1- \sigma_2)^2+ (\sigma_1- \sigma_3)^2+ (\sigma_2- \sigma_3)^2)]^{1/2} = (3/2)^{1/2} \tau_{oct}$

τ_{oct} = $1/3 [(\sigma_1- \sigma_2)^2+ (\sigma_2- \sigma_3)^2+ (\sigma_3- \sigma_1)^2]^{1/2}$

A = $C_0/3^{1/2} - BC_0/3 - CC_0^2/9$

B = $3^{1/2} (q-1)/(q+2) - C/3(2C_0 + (q+2)\sigma_3)$

C = $[27^{1/2}/(2C_1 + (q-1)\sigma_3 - C_0]\times [[(C_1 + (q - 1)\sigma_3 - C_0)/(2C_1 +(2q+1)\sigma_3 - C_0)] - [(q-1)/(q+2)]]$

C_1 = $(1 + 0.6\mu) C_0;\ q = [(\mu^2 + 1)^{1/2} + \mu]^2 = \tan^2 (\pi/4 + \phi/2)$

The values of C_0 (uniaxial compressive strength) yielded by the Inscribed and the Circumscribed Drucker–Prager criteria bounded the C_0 (uniaxial compressive strength) value obtained using the Mohr–Coulomb criterion as expected. In general, the Drucker–Prager failure criterion did not accurately indicate the value of σ_1 at failure. The value of the misfits achieved with the empirical 1967 and 1971 Mogi criteria were generally in between those obtained using the triaxial and the polyaxial criteria. The disadvantage of these failure criteria is that they cannot be related to strength parameters such as C_0: They also found that if only data from triaxial tests are available, it is possible to incorporate the influence of σ_2 on failure by using a polyaxial failure criterion. The results for two out of three rocks that could be analyzed in this way were encouraging.

Kwasniewski et al. (2003) use prismatic samples of medium-grained sandstone from Śląsk Colliery for testing under uniaxial compression, conventional triaxial compression and true triaxial compression conditions. Results of the studies show that confining pressure strongly inhibited dilatant behavior of rock samples tested under conventional triaxial compression conditions; the increasing confinement resulted in the growing compaction of the rock material. The effect of dilatancy was also highly suppressed by the intermediate principal stress. While important dilatant, negative volumetric strain corresponded to the peak differential stress at low intermediate principal stress conditions, at high intermediate stresses the rock material was damaged to much lesser extent. As a result, faulting of rock samples in the post-peak region was much more violent and was accompanied by a strong acoustic effect.

Alexeev et al. (2004) present two generations of true triaxial loading (TTAL) apparatus. First generation was intended primarily for true stress state imitation in rock or mineral specimens. Advanced second-generation is designed to provide precise measurements in any stress and simulation of rock outburst at sudden relief of one sample face. Both TTAL apparatuses can apply pressure up to 250 MPa, corresponding to earth depth about 10,000 m, independently along each of three axes. Experimental results are given on effect of absorbed water on ultimate state in coal as well as adsorbed methane influence on simulated coal outbursts.

Tiwari and Rao (2004) described physical modeling of a rock mass under a true triaxial stress state by using block mass models having three smooth joint sets. The testing used true-triaxial system (TTS) developed by Rao and Tiwari (2002), shown in Figure 2.6. The test results show the strength of rock mass (σ_1) and deformation modulus (E_j) increase significantly which is confirmed by fracture shear
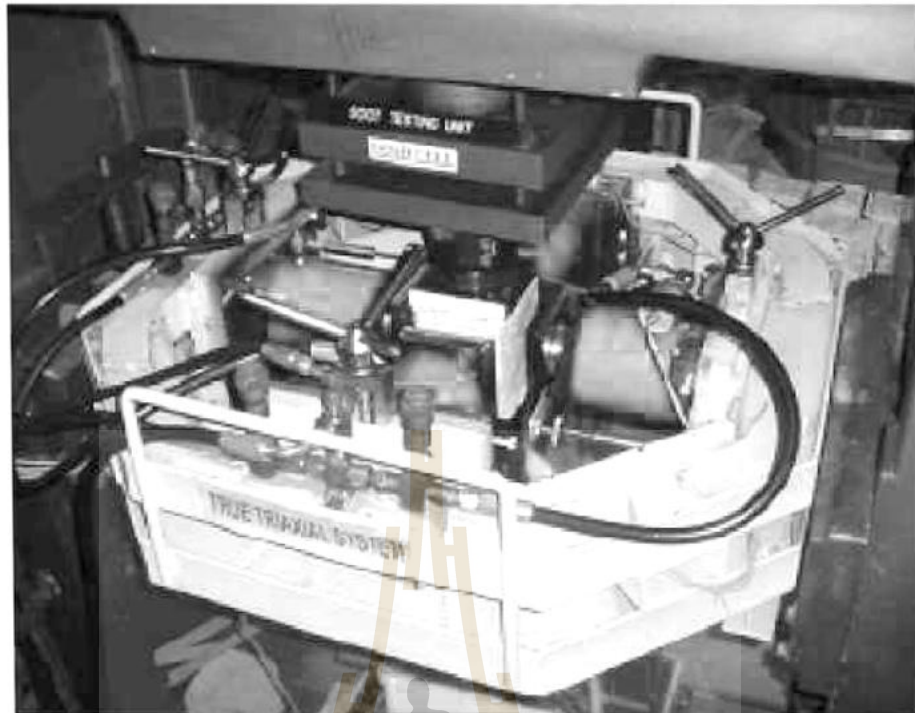
11.5

Figure 2.6 True triaxial system used for study (Tiwari and Rao, 2004).

planes developed on σ2 face of specimen. Most of the specimens failed in shearing with sliding in some cases. The effect of interlocking and rotation of principal stresses σ_2 and σ_3 on strength and deformation response was also investigated.

Chang and Haimson (2005) discuss the non-dilatants deformation and failure mechanism under true triaxial compression. They conducted laboratory rock strength experiments on two brittle rocks, hornfels and metapelite, which together are the major constituent of the long valley Caldera (California, USA) basement in the 2025 – 2996 m depth range. Both rocks are banded, very high porosity. Uniaxial compression test at different orientations with respect to banding planes reveal that the hornfels compressive strength nearly isotropic, the metapelite possesses distinct anisotropy. Conventional triaxial tests in these rocks reveal that their respective strengths in a specific orientation increase approximately linearly with confining

pressure. True triaxial compressive experiments in specimens oriented at a consistent angle to banding, in which the magnitude of the least (σ_3) and the intermediate (σ_2) principal stress are different but kept constant during testing while the maximum principal stress is increased until failure, exhibit a behavior unlike that previously observed in other rocks under similar testing conditions. For a given magnitude of σ_3, compressive strength σ_1 does not vary significantly in both regardless of the applied σ_2, suggesting little or no intermediate principal stress effect. Strains measured in all three principal directions during loading were used to obtain plots σ_1 versus volumetric strain. These are consistently linear almost to the point of rock failure, suggesting no dilatants.

Haimson (2006) describes the effect of the intermediate principal stress (σ_2) on brittle fracture of rocks, and on their strength criteria. Testing equipment emulating Mogi's but considerably more compact was developed at the University of Wisconsin and used for true triaxial testing (Figure 2.7) of some very strong crystalline rocks. Test results revealed three distinct compressive failure mechanisms, depending on loading mode and rock type: shear faulting resulting from extensile microcrack localization, multiple splitting along the axis, and nondilatant shear failure. The true triaxial strength criterion for the KTB amphibolite derived from such tests was used in conjunction with logged breakout dimensions to estimate the maximum horizontal in situ stress in the KTB ultra deep scientific hole.

Alexeev et al. (2008) determine the effect of stress state factor on fracture of sandstone under true triaxial loading. Experimental results on rock deformation revealed a misfit between strain state and stress state, strain state varying from generalized compression to generalized shear at $\sigma_3 = 0$. This misfit can lead to data
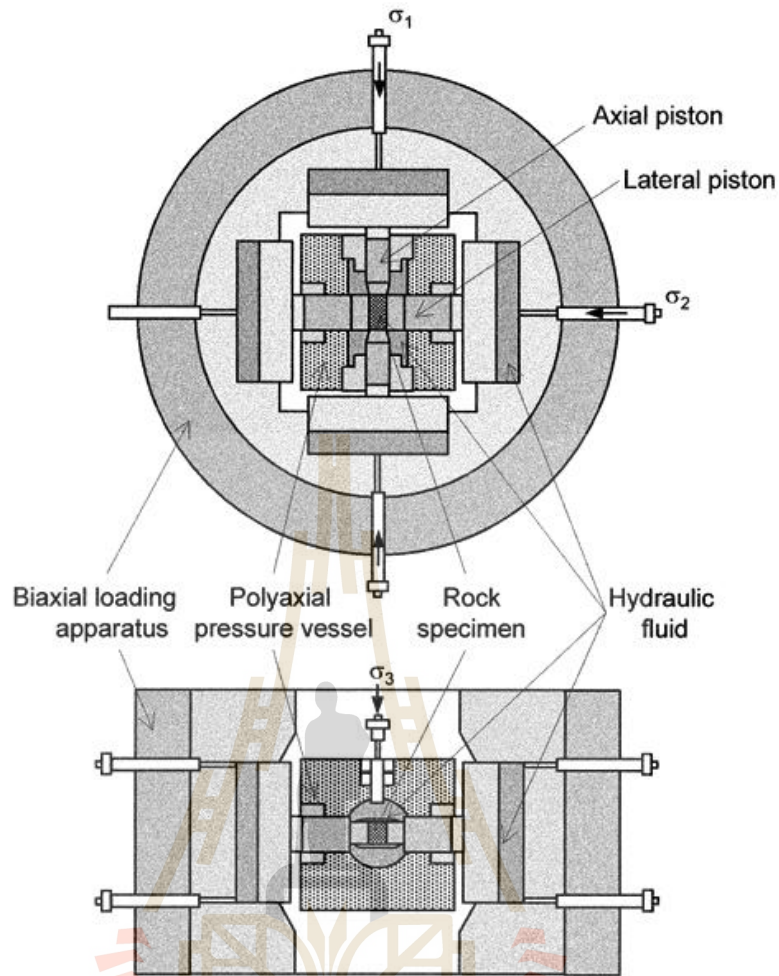
Figure 2.7   Schematic diagram of true triaxial testing system (Haimson, 2006).

misinterpretation during the stress field reconstruction after loading. Fracture of rock specimens under true triaxial compression occurs by a combined longitudinal/ transverse shear and produces the highest dilatancy effect.

An increase in the hydrostatic pressure level diminishes limiting values of shear strains and suppresses the dilatancy effect. A maximum of dilatancy coincides with a maximum of fresh surface area formed during the fracture of rock. The generalized cleavage of rocks becomes energetically disadvantageous in a true triaxial compressive stress field. Some sandstone becomes more brittle under true triaxial

compression ($\sigma_2 \neq 0$) at low values of the minimal stress component (σ_3) due to high initial porosity and dilatancy. The embrittlement effect found experimentally is inconsistent with the conclusion of Mogi (1971) and Haimson and Chang (2000) who found an additive effect of minimal compressive stress σ_3 and intermediate compressive stress σ_2 on strength of rocks. This discrepancy is obviously caused by the high initial porosity and dilatancy of some sandstone.

Cai (2008) study the influence of the intermediate principal stress on rock fracturing and strength near excavation boundaries, using a FEM/DEM combined numerical tool. At the boundary in an underground setting, the intermediate principal stress is often parallel to the tunnel axis, the minimum stress is zero, and the maximum principal stress is the tangential stress. A loading condition of $\sigma_3 = 0$, $\sigma_1 \neq 0$, and $\sigma_2 \neq 0$ thus exists at the boundary (Figure 2.8). It is seen from the simulation that the generation of tunnel surface parallel fractures (onion skins, spalling and slabbing) is attribute to the existence of moderate intermediate principal stress and low to zero minimum confinement (Figure 2.9). Material heterogeneity also plays a major role as local tensile stresses need to be generated for crack initiation and propagation. The intermediate principal stress confines the rock in such a way that fractures can only be developed in the direction parallel to σ_1 and σ_2. This fracturing process changes the rock behavior from the original isotropic state to an anisotropic.

You (2008) reviewed some strength criteria which include the role of the intermediate principal stress, and proposed a new criterion. Strength criteria of the form $\sigma_{oct} = f_n (\sigma_{oct})$, such as Drucker–Prager represent a rotation surface in the principal stress space, symmetric to the line $\sigma_1 = \sigma_2 = \sigma_3$ in the meridian plane. Because $\sigma_{oct} = f_n (\sigma_{oct})$ must fit the pseudo-triaxial compressive strength, it will have a
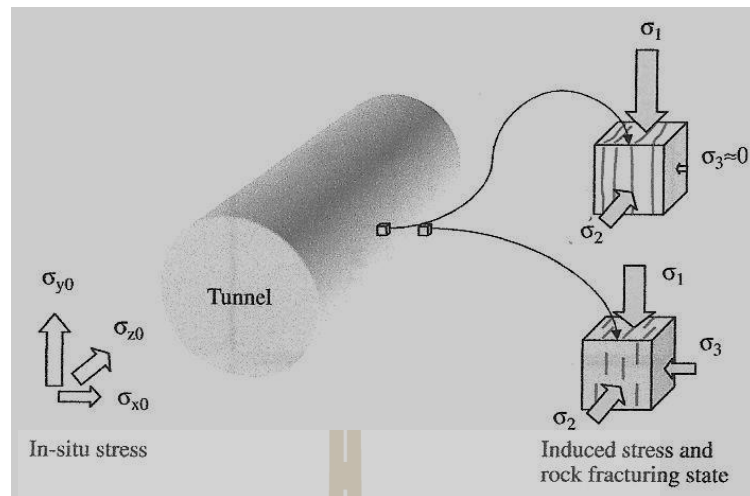
Figure 2.8 Stress and rock fracturing condition near the tunnel boundary σ_{x0}, σ_{y0}

and σ_{z0} are the far field stress components (Cai, 2008).

Figure 2.9 A granite slab show the layered fracturing that occurred at the Mine-by

tunnel at URL. The stress-induced fractures are parallel to the tunnel

surface. (Cai, 2008).

non-physical outcome for triaxial extension. Mogi's criteria, $\sigma_{oct} = g_1 (\sigma_{m,2})$ and $\sigma_{max} = g_2 (\sigma_b)$ are able to fit experimental data reasonably well, but the prediction of strength is not good and sometimes problematic. Strength criterion with the form $\lambda(\sigma_1, \sigma_2, \sigma_3) = F[\eta(\sigma_1, \sigma_2, \sigma_3)]$, or a curve of two variables which can be decided by fitting pseudo-triaxial experimental data, is not expected to describe the strength under various stress states, no matter how high the correlation coefficient of λ and η is, or how low the misfit of the equation $\lambda = F(\eta)$ is, as these seemingly good correlations usually result from the dominant influence of the maximum principal stress in the metrics of λ and η. The intermediate principal stress may improve the strength of rock specimen, but its influence will be restricted by σ_3. Also when σ_2 is high enough to cause failure in the $\sigma_2 - \sigma_3$ direction, the strength will decrease with the increasing σ_2. The new strength criterion with exponent form has just such a character, and gives much lower misfits than do all seven criteria discussed by Colmenares and Zoback (2002). A statistical evaluation of intact rock failure criteria constrained by polyaxial test data for five different rocks.

2.4   Effect of stress path on rock strength

The strength and deformation behavior of rock material are dependent on the loading path, which have been widely investigated in the past decades to understand and explore the fracture mechanism of various rock engineering (such deep underground rock engineering, and tunnel rock engineering, etc.) under different loading paths (Jaeger, 1967; Swanson and Brown, 1971; Crouch, 1972; Yao et al., 1980; Xu and Geng, 1986; Ferfera et al., 1997; Lee et al., 1999; Cai, 2008; Wang et al., 2008; Yang et al., 2011; Yang et al., 2012). In the previous studies, two kinds of

loading paths, i.e. conventional triaxial compression (Path I) and confining pressure reduction (Path III) (Figure 2.10) (detailed definition can be referred in the paper (Yang et al., 2011), are often adopted to analyze the strength and deformation behavior of all kinds of rock material. On the influence of the loading path on the strength of rock, there are two kinds of contradictory opinions. One opinion regarded that the strength of the rock was independent to the stress loading path by carrying out triaxial compression experiment for granite and norite (Swanson and Brown, 1971; Crouch, 1972). Another opinion regarded that the loading path had a significant influence on the loading path.

Xu and Geng (1986) studied the various loading paths causing strength, deformation and failure in hard and soft rocks. His results showed that the effect of two loading paths (Paths I and III) on the peak strength was related to lithologic character. Wang et al. (2008) thought that the cohesion of marble under Path III was distinctly lower than that under Path I, but the internal friction angle of marble under Path III had no obvious difference with that under Path I. But on the influence of the loading path on the deformation behavior of rock, Yao et al. (1980) carried out triaxial experiment for gabbro and marble under Paths I and III, which showed that the gabbro under Path III was more brittle than that under Path I, but marble under Path III could appear some brittle fracture even though under higher confining pressure.

Yang (2013) performed triaxial compression test of red sandstone to investigated its strength and deformation behavior. The conditions of testing were under simple and complex loading path. In this research, tested confining pressure was in the range from 5 to 35 MPa. Under simple loading path, the peak strength, residual strength and critical damage of samples all increase with the confining pressure,
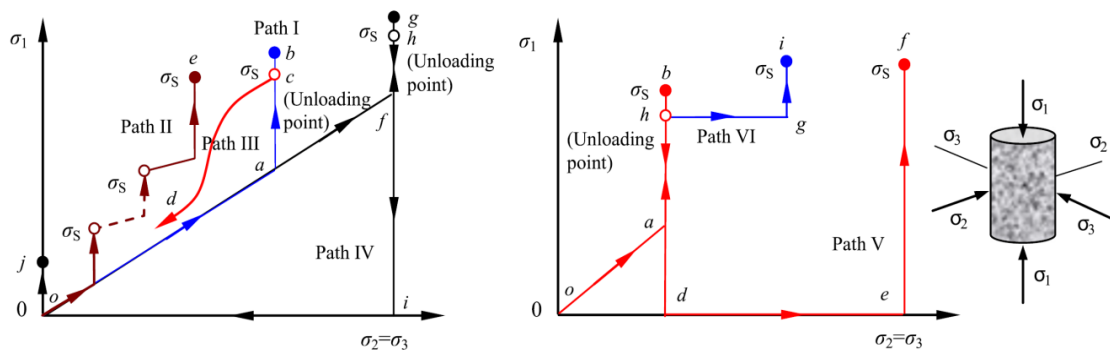
Figure 2.10 Six different loading paths presented in the principal stress space (σ_3, σ_1) (Yang et al., 2011).

which are in good agreement with the linear Mohr–Coulomb criterion. The differences of strength and deformation parameters of red sandstone between simple and complex loading paths are evaluated detailed. The elastic moduli under those loading paths all increase nonlinearly with the confining pressure. It is suggested and recommended to predict the peak strength of rock under simple loading path by adopting complex loading path A (increasing gradually the confining pressure) not complex loading path B (reducing gradually the confining pressure). On the basis of the linear Mohr–Coulomb criterion, a kind of new method is put forward to revise the peak strength of red sandstone under complex loading path A, which is testified to be right and reasonable. Some noticeable result shown in Figure 2.11, the influence of confining pressure on the elastic modulus of red sandstone under complex loading path B.

Yang et al. (2011) have investigated the mechanical behavior of coarse marble under six different loading paths. A series of triaxial compression experiments preformed for the samples by the rock mechanics servo-controlled testing system. Based on the experimental results of complete stress-strain curves, the influence of
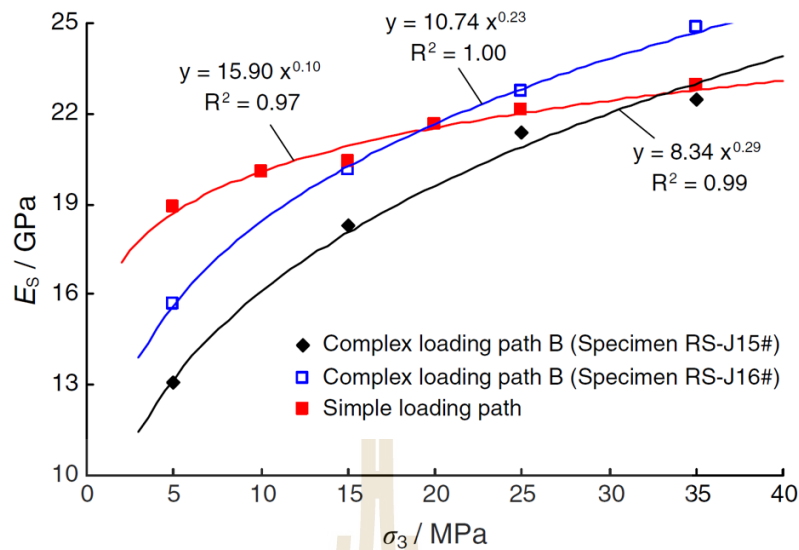
Figure 2.11 Effect of confining pressure on elastic modulus of red sandstone under complex loading path B.

loading path on the strength and deformation failure behavior of coarse marble is made a detailed analysis. Three loading paths (Paths I–III) are put forward to confirm the strength parameters (cohesion and internal friction angle) of coarse marble in accordance with linear Mohr-Coulomb criterion. Compared among the strength parameters, two loading paths are suggested to confirm the triaxial strengths of rock under different confining pressures by only one sample, which is very applicable for a kind of rock that has obvious plastic and ductile deformation behavior. In order to investigate re-fracture mechanical behavior of rock material, three loading paths (Paths IV–VI) are also put forward for flawed coarse marble. The peak strength and deformation failure mode of flawed coarse marble are found depending on the loading paths (Paths IV–VI). Under lower confining pressures, the peak strength and Young's modulus of damage sample (compressed until post-peak stress under higher confining pressure) are all lower compared with that of flawed sample. Mechanical parameter

of damage sample is lower for the larger compressed post-peak plastic deformation of coarse marble. However under higher confining pressures (e.g. σ 3 = 30 MPa), the axial supporting capacity and elastic modulus of damage coarse marble (compressed until post-peak stress under lower confining pressure) is not related to the loading path, while the deformation modulus and peak strain of damage sample depend on the difference of initial confining pressure and post-peak plastic deformation. The friction among crystal grains determines the strength behavior of flawed coarse marble under various.

Yang et al. (2011) have investigated the mechanical behavior of coarse marble under six different loading paths. A series of triaxial compression experiments preformed for the samples by the rock mechanics servo-controlled testing system. Based on the experimental results of complete stress-strain curves, the influence of loading path on the strength and deformation failure behavior of coarse marble is made a detailed analysis. Three loading paths (Paths I–III) are put forward to confirm the strength parameters (cohesion and internal friction angle) of coarse marble in accordance with linear Mohr-Coulomb criterion. Compared among the strength parameters, two loading paths are suggested to confirm the triaxial strengths of rock under different confining pressures by only one sample, which is very applicable for a kind of rock that has obvious plastic and ductile deformation behavior. In order to investigate re-fracture mechanical behavior of rock material, three loading paths (Paths IV–VI) are also put forward for flawed coarse marble. The peak strength and deformation failure mode of flawed coarse marble are found depending on the loading paths (Paths IV–VI). Under lower confining pressures, the peak strength and Young's modulus of damage sample (compressed until post-peak stress under higher confining

pressure) are all lower compared with that of flawed sample. Mechanical parameter of damage sample is lower for the larger compressed post-peak plastic deformation of coarse marble. However under higher confining pressures (e.g. $\sigma 3 = 30$ MPa), the axial supporting capacity and elastic modulus of damage coarse marble (compressed until post-peak stress under lower confining pressure) is not related to the loading path, while the deformation modulus and peak strain of damage sample depend on the difference of initial confining pressure and post-peak plastic deformation. The friction among crystal grains determines the strength behavior of flawed coarse marble under various loading paths. In the end, the effect of loading path on failure mode of intact and flawed coarse marble is also investigated. The present research provides increased understanding of the fundamental nature of rock failure under different loading path

A change of stress state in the rock mass causes the accumulation of damage at macro- but also at micro scale. Hence, the damage that has been created in the past, remains in the rock and represents a 'fingerprint' of the completed loading history (Lavrov, 2005). In this way, the former stress path influences the response of the rock material in future loadings. The Kaiser effect (Lavrov et al., 2002) is a well known expression of this phenomenon. In its easiest form, the Kaiser effect can be observed in rocks during their cyclic uniaxial loading by acoustic emission (AE) monitoring. As soon as the load achieves its previously reached peak value, a noticeable increase in acoustic emission activity takes place. As such, it is used to determine the peak stresses and principal stress orientations of rock material in the past. Another example of the influence of the stress path is linked to core drilling (Holt et al., 2000). As the drilling of cores causes a stress evolution, the characteristics of the drilled core material are affected by the drilling. If these cores are to be tested, laboratory tests

may be performed in away that limits core damage effects. In this reasoning, Holt et al. (2000) propose among others the use of a specific stress path for UCS (uniaxial compressive strength) determination and the use of multiple loading cycles to determine the compaction modulus of drilled cores. The stress path dependency of the response of the rock material manifests itself also at large scale, such as fracture development in underground mines, tunnels and on slopes. Recent research projects have focused on the study of the stress path: in-situ measuring of stress path around excavations (Kaiser et al., 2001), laboratory tests to investigate the effect of stress path on the response of rock material (Der-Her Lee et al. 1999; Vervoort 2003) and numerical modelling (Eberhardt 2001; Alassi et al. 2006). Eberhardt (2001) reports that in the case of an advancing tunnel face in rock material (calculated with a three-dimensional finite difference code), the principal stresses change in magnitude as well as in orientation. He demonstrates that around an advancing tunnel face, the principal stress components can change from a situationwith three principal stresses in compression to a situation where one principal stress is tension. The paper describes and discusses the influence of the stress path on micro-damage. Two specific situations are considered. First, samples successively damaged by macro-compressive and tensile stresses are studied. Second, samples successively damaged by macro-tensile and compressive stresses are studied and compared to the first case. In this way, the influence of the succession of the compressive and tensile stresses is quantified. Most of the study is based on a systematic observation of thin slices and recorded AE.

2.5   True-triaxial testing techniques

The deformation and failt1re of crust and engineering rock masses are under a stress state with three unequal principal stresses, i.e., a true triaxial stress state. One of the major goals of rock mechanics testing in a laboratory is to characterize deformation and strength behaviors under in-situ stress states. The Karman-type triaxial test (Figure 2.12) proposed by Karman (1911), in which a short, cylindrical specimen is loaded axially, has been widely used in experimental rock mechanics because of the simplicity of the equipment and the convenient preparation of specimens. In a Karman-type triaxial test, the intermediate and minimum principal stresses are equal, and therefore, it is also called a conventional triaxial test (CTT). The characteristics of rock strength, deformation and failure have mainly come from CTT. However, two of the three principal stresses are equal in CTT, which means the stress paths are only confined on a certain plane in the stress space. As a result, the intermediate principal stress has no effect on rock failure and this is the key assumption in conventional triaxial tests. This point is typically illustrated by the Mohr-Coulomb criterion.

A large number of in-situ stress measurements have shown that an actual stress state is almost anisotropic. Thus, in the CTT initiated by Karman (1911) and Boker (1915), besides that the compressive strength of brittle rocks is very dependent on confining pressure, which is well explained by the Mohr-Coulomb and Griffitn theories, the strengths of Carrara marble determined from compression ($\sigma_1 > \sigma_2 = \sigma_3$) and extension ($\sigma_1 = \sigma_2 > \sigma_3$) tests under the same confining pressure are slightly different. The unconformity of Mohr's envelopes between compression and tension under the same confining pressure was reconfirmed by Murrell (1965) and
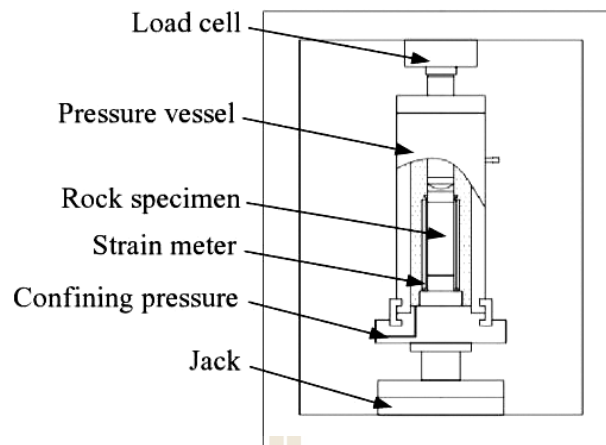
Figure 2.12 Schematic of a CTT apparatus.

Handin et al. (1967). This finding was the starting point in taking into account the intermediate principal stress σ_2 in the rock failure criterion. Thereafter, scholars became enthusiastic over the development of a compression testing apparatus which could control σ_2 and σ_3 independently in order to examine the effect of σ_2 on rock strength.

Since then, various types of true triaxial test (TTT) apparatuses which can simulate the general stress state ($\sigma_1 > \sigma_2 > \sigma_3$) have been developed one after another and the research on the effect of intermediate principal stress has entered a new phase. Among the true triaxial test apparatuses, the one designed by Mogi (1970) is perhaps the first that permitted the application of three mutually independent and uniform loads to the specimen faces (Haimson & Chang 2000). It was found that the maximum principal stress σ_1, at failure is a function of σ_2 with a concave curve of σ_1 vs. σ_2 under constant σ_3 (e.g., Mogi 1967, Xu & Geng 1985, Kwasniewski & Mogi 1990, Li & Xu 1991, Haimson & Chahg, 2000). The theories and applications which have their roots in true triaxial test have been verified by practical engineering cases such as borehole breakout (e.g., Vernik & Zoback 1992, Haimson & Chahg 2002) and rock-burst (e.g., Xu et al.

2000, Alexeev et al. 2004, He et al. 2007). Moreover, the importance of the effect of the intermediate principal stress on the hydro-mechanical behavior of rocks has been studied by Takahashi et al. (1993), Skoczylas and Henry (1995), King et al. (1995), etc.

However, the true triaxial test techniques for rock testing are far from mature. There is no piece of equipment that is as extensively used as the standard CTT apparatt1ses even though it has undergone vigorous development in the past few decades. The true triaxial test techniques are subject to a number of obstacles and problems such as end friction, blank loading corners, high costs, etc. In addition, no country or academic society associated with rock mechanics has true triaxial test procedures as yet.

In the early stages, hollow cylindrical specimens (e.g., Robertson 1955, Hoskins 1969) were used for compression tests (e.g., Robertson 1955, Hoskins 1969) and for con1bined compression and torsion tests (Handin et al. 1967) in order to obtain true triaxial stress states. In order to overcon1e the stress gradient that exists in a thick hollow cylinder and to achieve a nearly homogeneous stress distribt1tion, a very thin hollow cylinder was used by Handin et al. (1967) as is shown in Figure 2.13. The thickness of the wall of the hollow cylinder used in the tests was 0.7 mm and the confining pressure reached 500 MPa. So1ne valt1able conclusions about the effects of σ_2 on sl1ear strength, fracture angle and brittle-ductile transitional pressure were obtained from Handin's tests. However, such tests did not find a wider application. As was pointed out by Mogi (2007), the experimental data obtained from thin-hollow-cylinder tests are very scattered. The thickness of a Hollow cylinder wall is too thin to be suitable for tests of brittle rocks and furthermore, it is inevitable that microcracks will be generated when fabricating such a thin hollow cylinder. Even so, the method of hollow
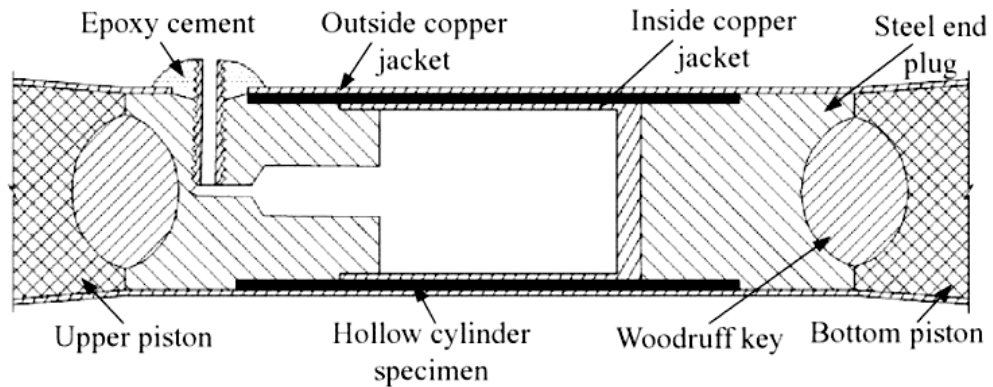
Figure 2.13 Schematic of a hollow cylinder for a torsion test (Handin et al., 1967).

cylinder torsion was the initiation of the true-triaxial testing technique for rocks. It is unique in that it is a compressive test for applying general principal stresses indirectly, and it planted the seed for realizing true triaxial loading.

For the next few decades in the field of true triaxial test, the three principal stresses were applied directly by dozens of true triaxial test apparatuses. According to Takahashi et al. (1989, 2001) and Mogi (2007), the true triaxial test apparatuses can be neatly classified into three types in terms of loading methods, i.e., Type-I: the rigid platen type, Type-II: the flexible mediu1n type ai1d Type-III: the mixed type. Figures 2.14 through 2.16 are present the true triaxial compression apparatuses used in true triaxial testing.
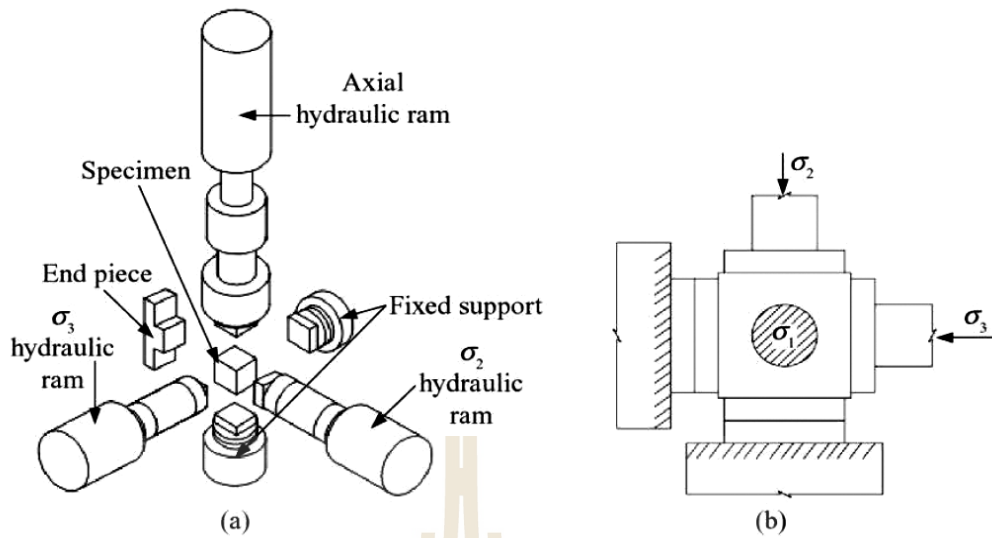
Figure 2.14 Schematic of a true triaxial apparatus by Fuuruzumi and Sugimoto (1986). (a) Conceptual diagram of the apparatus. (b) Force analysis of the specimen.
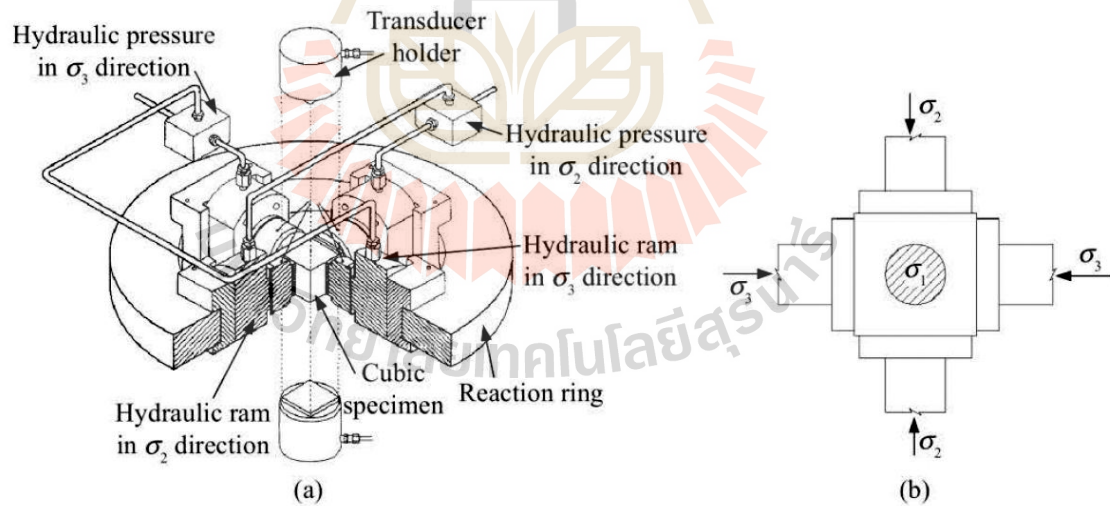
Figure 2.15 Schematic of a true triaxial apparatus by Fing et al. (1995). (a) conceptual diagram of the apparatus. (b) Force analysis of the specimen.
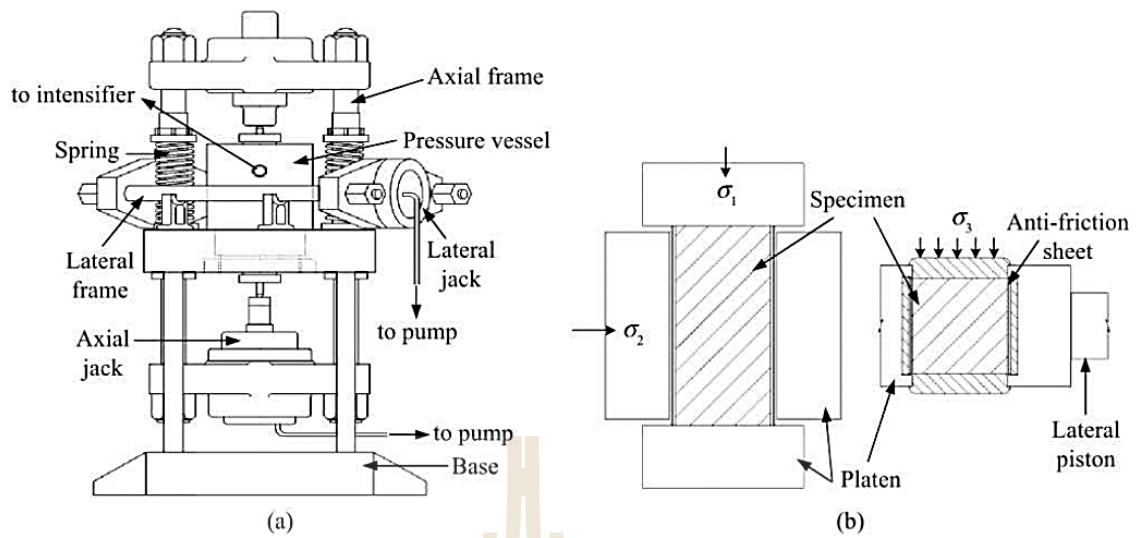
Figure 2.16 Schematic of a true triaxial apparatus by Mogi (1970). (a) Front view of

the apparatus. (b) Assembly of a specimen and platens.

CHAPTER III

SAMPLE PREPARATION

This chapter describes the rock sample preparation. The rock samples used in this study is rock salt. The salt specimens tested here are obtained from the Middle members of the Maha Sarakham formation in the northeastern Thailand. This salt member has dedicate by THAI KALI Company Limited. The core specimens with a nominal diameter of 63 mm tested here were drilled from depths ranging between 150 and 330 m. The rectangular block specimens are cut and ground to have a nominal dimension of $4.5 \times 4.5 \times 9.0$ cm^3 as shown in Figure 3.1. Sample preparation is conducted in laboratory facility at the Suranaree University of Technology. Table 3.1 summarizes the specimen number, dimensions and density.
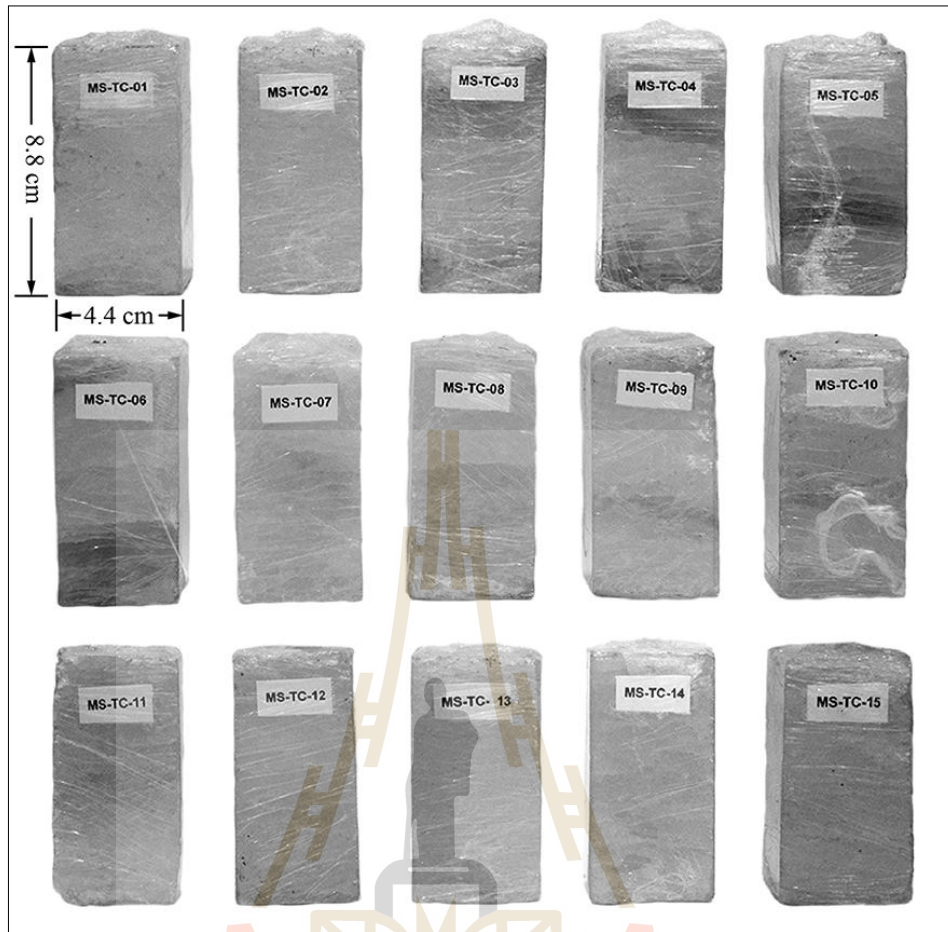
Figure 3.1 Some salt specimens prepared for true triaxial testing. The nominal

dimension is $4.5 \times 4.5 \times 9.0$ cm^3.

Table 3.1 Specimen dimensions prepared for testing.

Specimen No.	Width (mm.)	Length (mm.)	Height (mm.)	Density (g/cc)
MS-PX-01	52.1	54.3	108.6	2.14
MS-PX-02	56.2	57.4	104.8	2.24
MS-PX-03	53.9	52.7	105.4	2.26
MS-PX-04	55.0	55.3	109.6	2.24
MS-PX-05	54.0	55.1	106.2	2.19
MS-PX-06	57.5	55.1	106.2	2.32
MS-PX-07	53.3	54.5	109.0	2.19
MS-PX-08	54.7	51.2	102.4	2.18
MS-PX-09	56.0	54.9	109.7	2.28
MS-PX-10	55.7	56.1	102.2	2.19
MS-PX-11	55.0	54.5	109.0	2.25
MS-PX-12	53.8	54.5	109.0	2.29
MS-PX-13	54.4	53.5	107.0	2.30
MS-PX-14	53.4	54.3	108.6	2.20
MS-PX-15	51.5	55.0	105.0	2.22
MS-PX-16	54.3	55.6	101.2	2.00
MS-PX-17	54.1	54.3	108.6	2.19
MS-PX-18	55.5	55.3	110.6	2.15
MS-PX-19	55.4	54.4	108.8	2.10
MS-PX-20	54.7	54.7	109.4	2.14
MS-PX-21	54.9	57.5	105.0	2.22
MS-PX-22	54.0	56.6	103.2	2.32
MS-PX-23	56.0	56.1	102.2	2.23
MS-PX-24	57.3	55.4	110.8	2.20
MS-PX-25	56.6	54.8	109.6	2.12
MS-PX-26	54.0	54.7	109.4	2.30
MS-PX-27	57.0	55.7	101.4	2.17
MS-PX-28	56.0	56.2	102.4	2.27
MS-PX-29	54.2	55.6	101.2	2.26
MS-PX-30	55.3	57.1	104.2	2.13
MS-PX-31	54.5	56.4	102.8	2.19
MS-PX-32	56.9	56.1	102.2	2.16
MS-PX-33	57.1	53.5	107.0	2.35
MS-PX-34	54.9	54.5	109.0	2.18
MS-PX-35	56.1	56.7	103.4	2.23
MS-PX-36	55.7	56.2	102.4	2.28
MS-PX-37	54.0	54.3	108.6	2.25

Table 3.1 Specimen dimensions prepared for testing (cont.).

Specimen No.	Width (mm.)	Length (mm.)	Height (mm.)	Density (g/cc)
MS-PX-38	55.4	55.1	107.2	2.12
MS-PX-39	56.8	55.9	101.8	2.05
MS-PX-40	55.0	55.3	107.6	2.01
MS-PX-41	53.7	54.2	108.4	2.22
MS-PX-42	54.0	56.5	103.0	2.15
MS-PX-43	54.5	55.2	106.4	2.34
MS-PX-44	54.0	54.6	109.2	2.15
MS-PX-45	55.6	55.6	101.2	2.05
MS-PX-46	53.7	53.9	107.8	2.22
MS-PX-47	53.8	53.1	106.2	2.32
MS-PX-48	56.1	56.5	103.0	2.35
MS-PX-49	55.2	55.5	101.0	2.13
MS-PX-50	53.4	54.6	109.2	2.21
Average				2.20 ± 0.09

CHAPTER IV

TEST PROCEDURE

4.1 Introduction

The objective of this study is to examine the influence of stress paths on rock deformation and failure. Multi-axial compression tests are performed on rock salt specimens to examine the effects of stress paths. Six different stress paths are planned on this laboratory test. The failure stresses are recorded and the elastic parameters calculated. This chapter describes the testing methods and equipment.

4.2 Test equipment

The main equipment for the multi-axial compression tests is the true triaxial load frame. Figure 4.1 shows the isometric drawing of the true triaxial loading device and the picture of this device during the tests. This device is developed to test the rock specimens with soft to medium strengths under polyaxial stress states. During the test each set of the three load frames will apply independent loads to provide different principal stresses on to the rock specimens. The main components of measurement system are pressure transducer, displacement transducer, switching box, and data logger. This loading device can accommodate the cubic or rectangular specimens of different sizes by adjusting the distances between the opposite steel loading platens. For this study, the rock specimens have the nominal dimensions of $4.5 \times 4.5 \times 9.0$ cm^3.

(a)   (b)
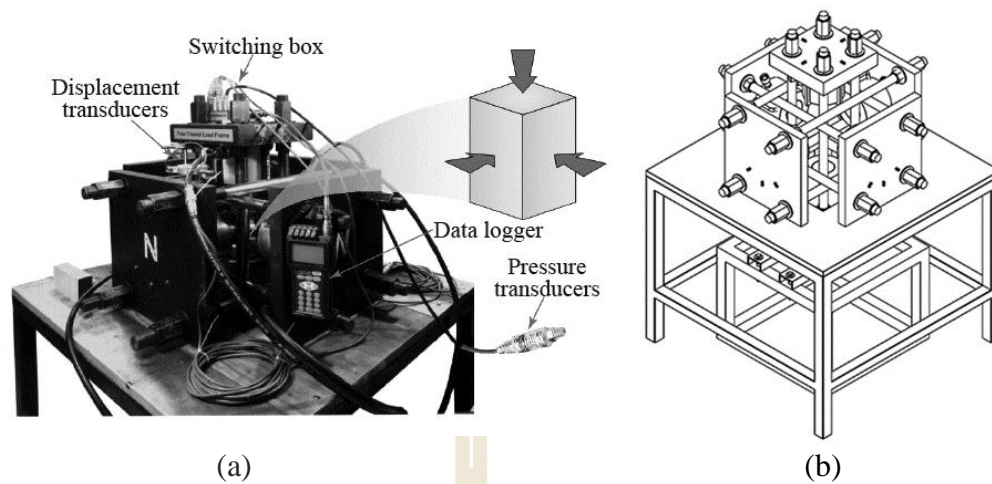
Figure 4.1   True triaxial load frame (a) general isometric drawing (b).

4.3   Test schemes

Three test scheme and six different stress paths have been implemented. The intermediate (σ_2) and minimum (σ_3) principal stresses depend on the stress paths while maximum principal stresses (σ_1) are increased until failure occurs. The three test schemes are briefly describe as follows.

The triaxial compression test ($\sigma_1 \neq \sigma_2 = \sigma_3$) is divided into two stresses paths. Stress path (1.1) is triaxial compression test with constant minimum principal stress; σ_3 (compression [σ_3], σ_1 increases while σ_2 and σ_3 are equally maintained constant). Stress path (1.2) is triaxial compression test with constant mean stress (σ_m) (compression [σ_m], σ_1 increases while σ_2 and σ_3 are simultaneously decreases). The constant σ_3 is varied from 1.0 to 28.0 MPa, and σ_m from 17.4 to 69.4 MPa.

The polyaxial compression test ($\sigma_1 \neq \sigma_2 \neq \sigma_3$) is divided into two stresses paths. Stress path (2.1) is the polyaxial compression test with constant σ_3 (polyaxial [σ_3], σ_1 and σ_2 increases while σ_3 maintained constant). Stress path (2.2) is the polyaxial

compression test with constant σ_m (polyaxial [σ_m], σ_1 increases while σ_2 maintain

constant and σ_3 decreases). The constant σ_3 is varies from 1.0 to 7.0 MPa, and σ_m is

from 23.3 to 79.4 MPa.

The triaxial extension test ($\sigma_1=\sigma_2\neq\sigma_3$) divided into two stresses paths. Stress

path (3.1) is triaxial extension test with constant σ_3 (extension [σ_3], σ_1 and σ_2 equally

increase while σ_3 is maintained constant). Stress path (2.2) is the triaxial extension

test with constant σ_m (extension [σ_m], σ_1 and σ_2 equally increase while σ_3 decreases).

The constant σ_3 is varied from 0 to 10.0 MPa, and σ_m from 20.6 to 65.0 MPa.

Figure 4.2 shows the applied principal stress directions for all test schemes.

Table 4.1 summarizes the test plan for all stress paths. For all tests, neoprene sheets

are used to minimize the friction at all interfaces between the loading platens and the

specimen surfaces. The measured deformations are measured to insument ± 10

microns used to determine the strains along the principal axes during loading. The

failure stresses are recorded.
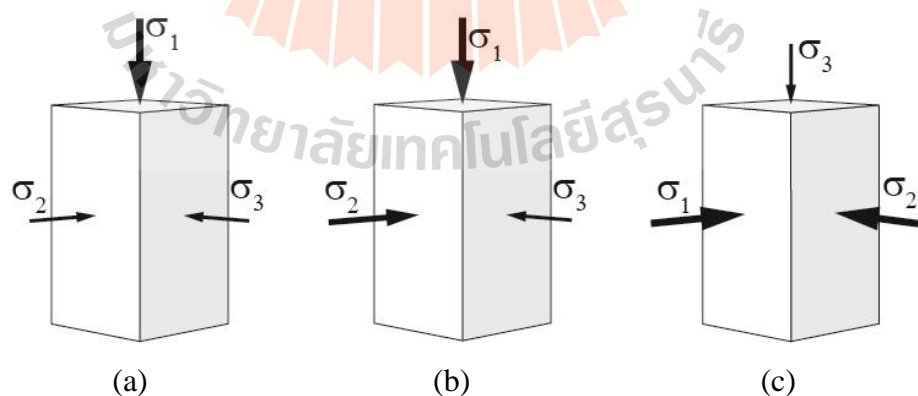
Figure 4.2 Directions of loading with for all test schemes: triaxial compression test

(a), polyaxial compression test (b), and triaxial extension test (c).

Table 4.1 Test plan for all stress paths.

Test schemes	Stress path	
	Constant [σ_3]	**Constant [σ_m]**
Scheme 1 Compression ($\sigma_1 \neq \sigma_2 = \sigma_3$)	 $\sigma_3 = 1.0$ to 28.0 MPa	 $\sigma_m = 17.4$ to 69.4 MPa
Scheme 2 Polyaxial ($\sigma_1 \neq \sigma_2 \neq \sigma_3$)	 $\sigma_3 = 1.0$ to 7.0 MPa	 $\sigma_m = 23.3$ to 79.4 MPa
Scheme 3 Extension ($\sigma_1 = \sigma_2 \neq \sigma_3$)	 $\sigma_3 = 0.0$ to 10.0 MPa	 $\sigma_m = 20.6$ to 65.0 MPa

CHAPTER V

TEST RESULTS

5.1 Introduction

This section describes test results in terms of the stress-strain curves, strength and elasticity for all test schemes. The measured deformations are used to determine the strains along the principal axes during loading. The failure loads are recorded and mode of failure examined.

5.2 Stress-strain curves

5.2.1 Test scheme 1: compression test

Figures 5.1 and 5.2 show all stress-stain curves for the test scheme 1. The results of triaxial compression tests of the test scheme 1 are shown in Table 5.1. The results indicate that stress path 1.1 (constant σ_3) provide higher strengths than those of stress path 1.2 (constant σ_m). Both paths show non-linear relation between stress and strain.

5.2.2 Test scheme 2: polyaxial test

The stress-strain curves of test scheme 2 are shown in Figures 5.3 and 5.4. For this test scheme the salt specimens are tested under polyaxial stress condition ($\sigma_1 \neq \sigma_2 \neq \sigma_3$). The stress path 2.1 maintains constant σ_3 during loading until failure while stress path 2.2 maintains constant σ_m. Table 5.2 shows the polyaxial compression test results for both stress paths.
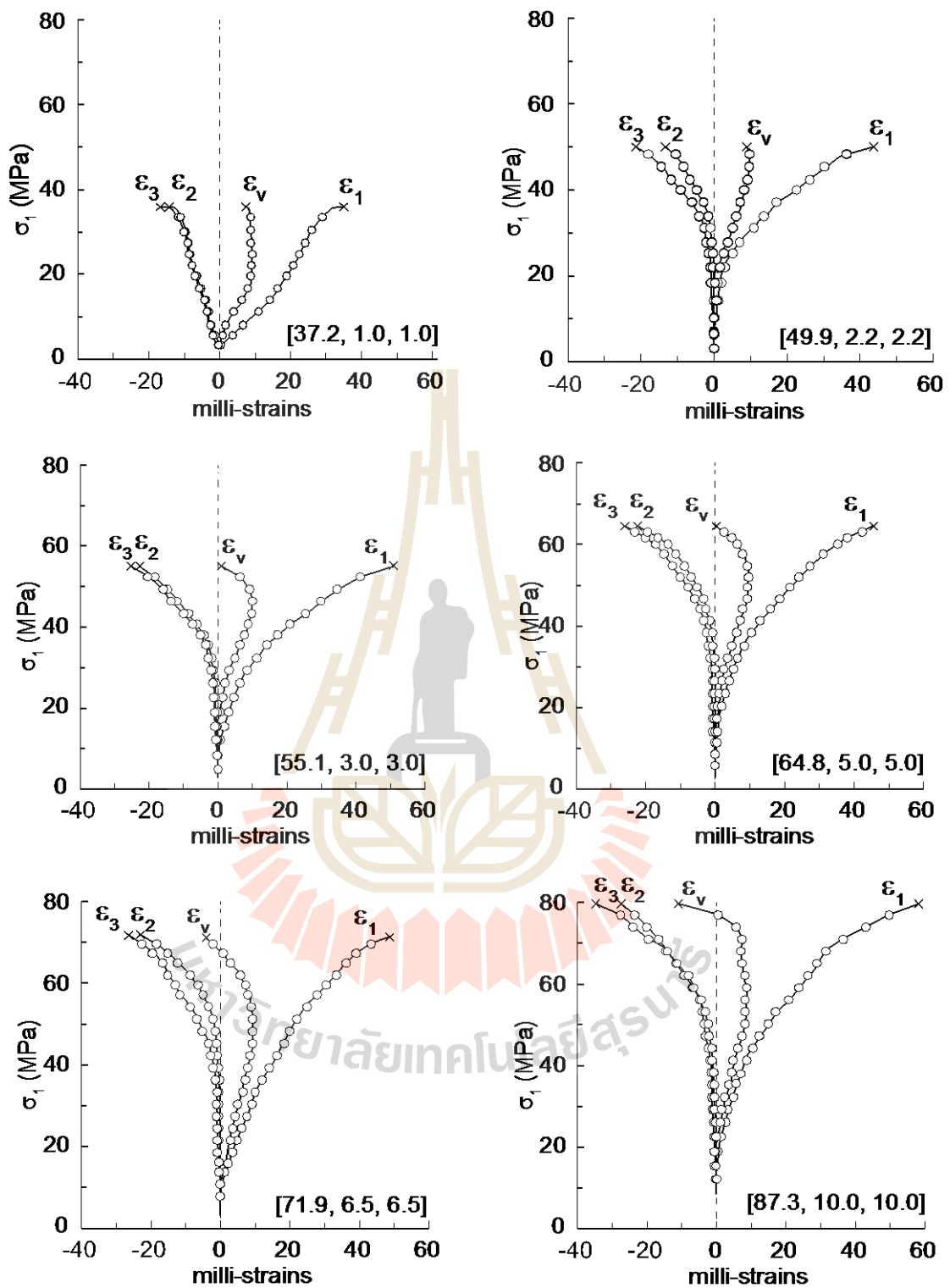
Figure 5.1 Stress-strain curves for triaxial compression test for stress path 1.1

constant σ_3. The numbers in the bracket represent $[\sigma_1, \sigma_2, \sigma_3]$ at failure.
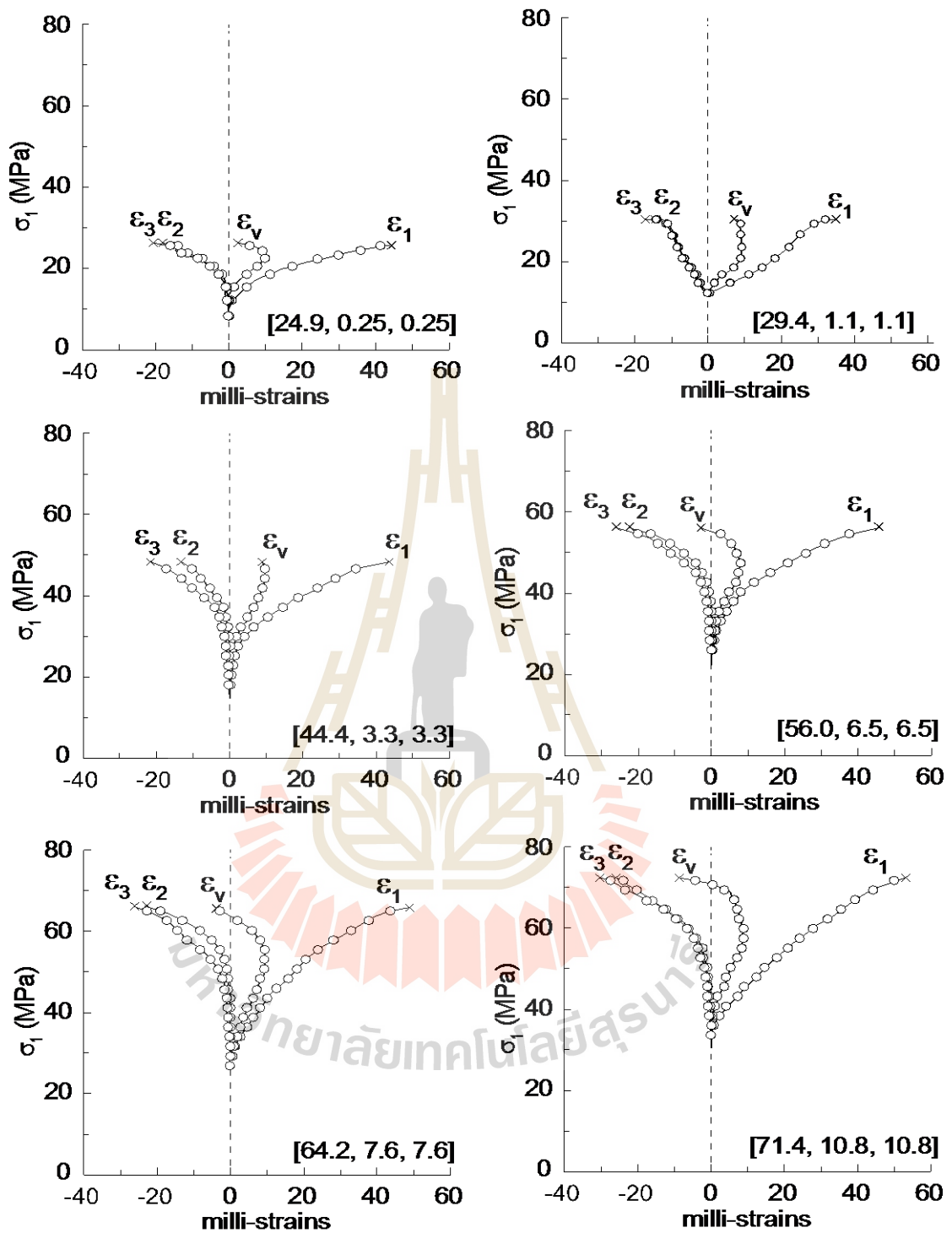
Figure 5.2 Stress-strain curves for triaxial compression test for stress path 1.2 constant σ_m. The numbers in the bracket represent [$\sigma_1, \sigma_2, \sigma_3$] at failure.
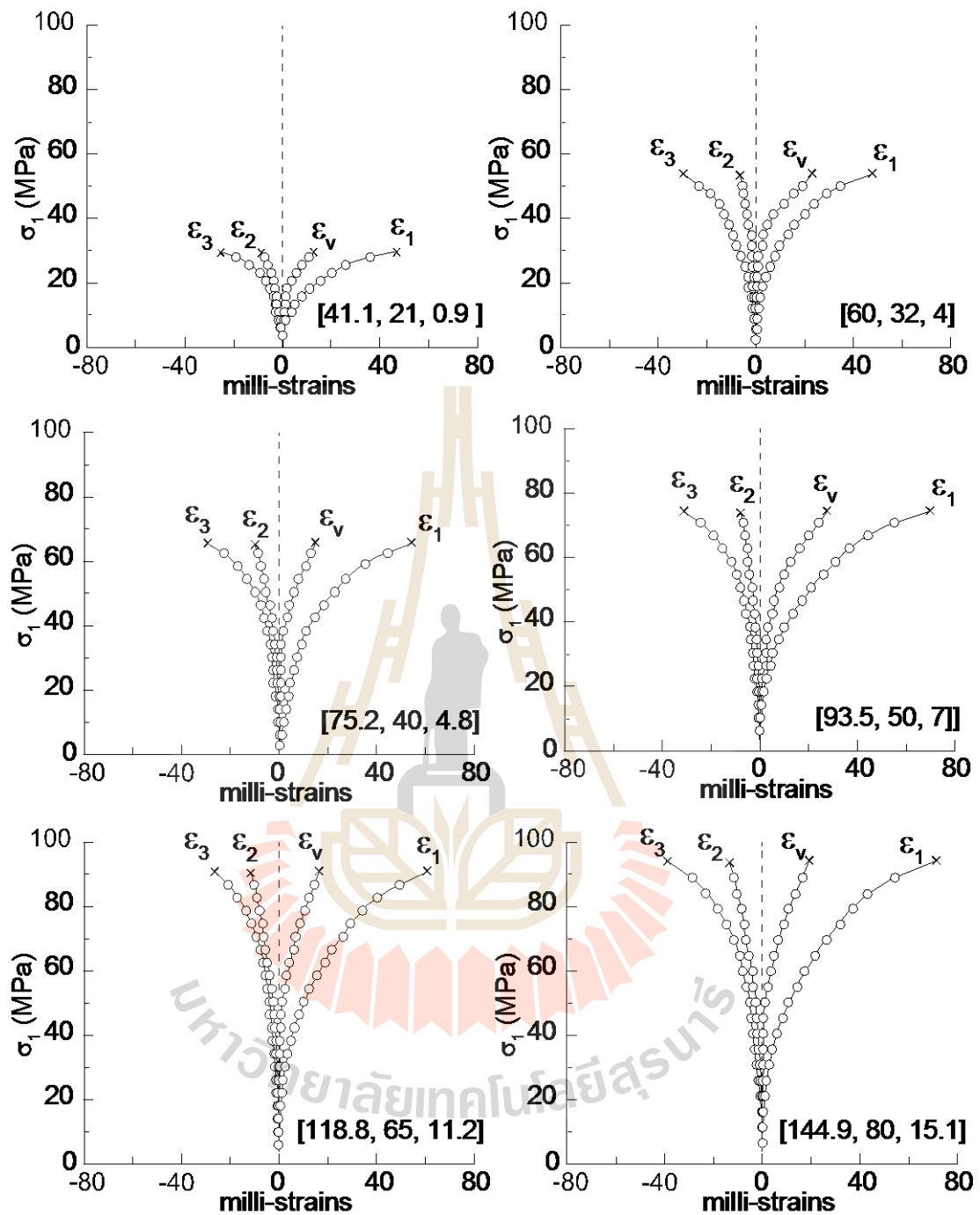
Figure 5.3 Stress-strain curves for polyaxial compression test of stress path 2.1 constant σ_3. The numbers in the bracket represent $[\sigma_1, \sigma_2, \sigma_3]$ at failure.
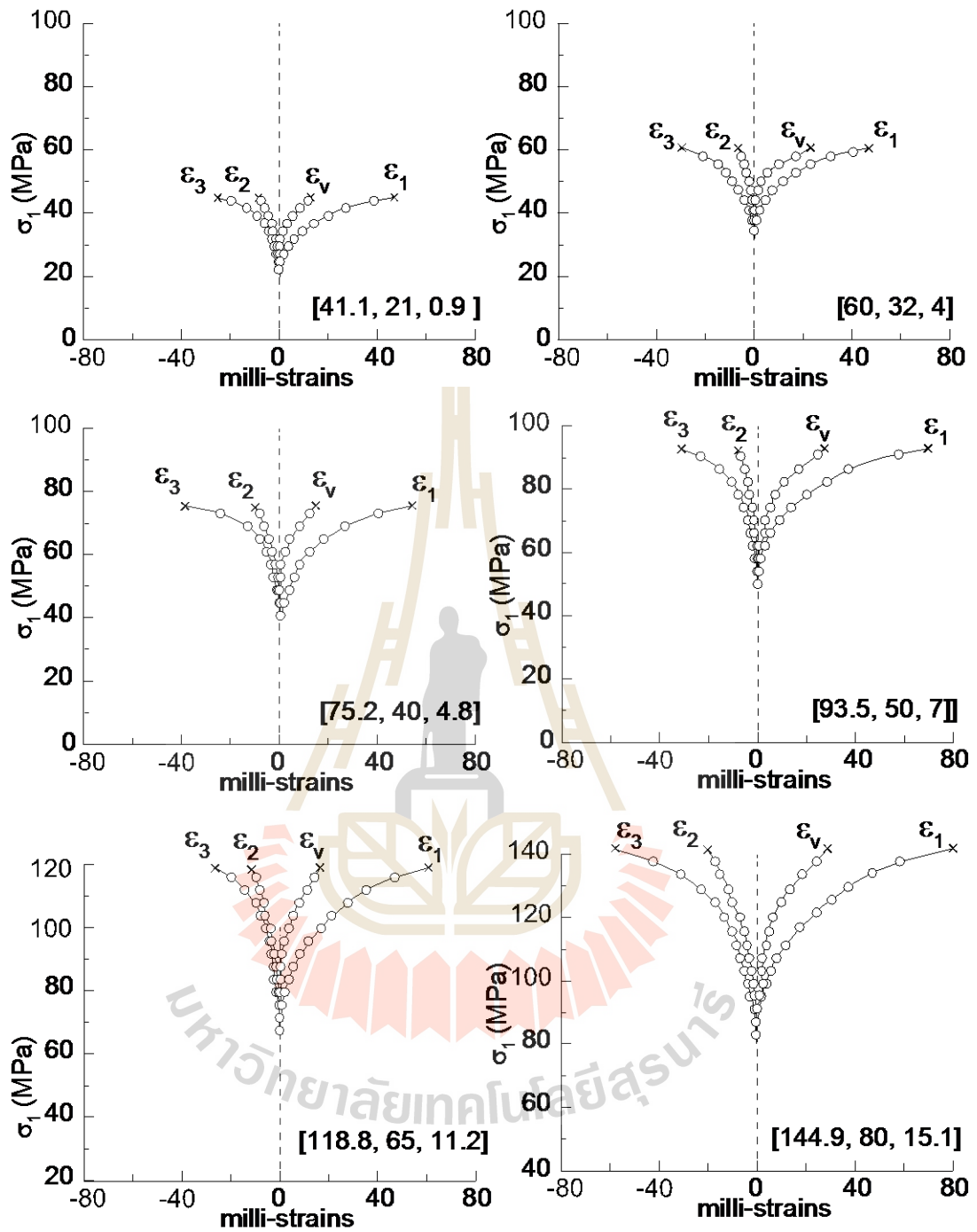
Figure 5.4 Stress-strain curves for polyaxial compression test of stress path 2.2 constant σ_m. The numbers in the bracket represent [σ_1, σ_2, σ_3] at failure.

Table 5.1 Strength results of triaxial compression tests (scheme 1).

Stress path (1.1) (constant σ_3)		Stress path (1.2) (constant σ_m)	
$\sigma_2 = \sigma_3$ (MPa)	σ_1 (MPa)	$\sigma_2 = \sigma_3$ (MPa)	σ_1 (MPa)
1.0	37.2	0.25	24.9
2.2	49.9	1.1	29.4
3.0	55.1	3.3	44.4
5.0	64.8	6.5	56.0
6.5	71.9	7.6	64.2
10.0	87.3	10.8	71.4
12.0	94.1	15.2	88.1
20.0	120.0	19.5	110.8
22.8	138.9	25.2	129.7
28.0	167.2	30.4	148.5

Table 5.2 Strength results of polyaxial compression tests (scheme 2).

Stress path (2.1) (constant σ_3)			Stress path (2.2) (constant σ_m)		
σ_3 (MPa)	σ_2 (MPa)	σ_1 (MPa)	σ_3 (MPa)	σ_2 (MPa)	σ_1 (MPa)
1.0	7.0	30.2	0.9	21.0	41.1
1.0	35.0	55.5	4.0	32.0	60.0
3.0	25.0	65.1	4.8	40.0	75.2
3.0	40.0	75.2	7.0	50.0	93.5
5.0	50.0	90.6	11.2	65.0	118.8
7.0	50.0	99.5	15.1	80.0	144.9
7.0	65.0	119.5			

5.2.3 Test scheme 3: extension test

Figures 5.5 and 5.6 show the stress-stain curves from start loading until failure for test scheme 3. Table 5.3 summarizes the strength results. For triaxial triaxial extension tests, stress path 3.1 yields higher strengths of specimens, compared to the stress path 3.2. From Table 5.3, for σ_3 equals to 6.5 MPa, the sample shows failure stress of 89.1 MPa under stress path 3.1, and of 73.5 MPa under stress path 3.2.

5.3   Octahedral shear stress-strain relations

An attempt is made here to compare the stress-strain relations obtained from different stress paths. To combine the principal stress and principal strain, a muti-axial form of stress-strain relation is needed. Here the octahedral shear stress (τ_{oct}) are calculated as a function of octahedral shear strain (γ_{oct}). The results are show in Figure 5.7. Jaeger et al. (2007) give the solutions for calculating these parameters, as follows;

$$\tau_{oct} = (1/3)[(\sigma_1 - \sigma_2)^2 + (\sigma_1 - \sigma_3)^2 + (\sigma_2 - \sigma_3)^2]^{1/2} \qquad (5.1)$$

$$\gamma_{oct} = (1/3)[(\varepsilon_1 - \varepsilon_2)^2 + (\varepsilon_1 - \varepsilon_3)^2 + (\varepsilon_2 - \varepsilon_3)^2]^{1/2} \qquad (5.2)$$

From the τ_{oct} - γ_{oct} diagrams (Figure 5.7) it is clear that the stress-strain relation for all stress paths are non-linear, where the non-lineality is greatest for the test scheme 1 (compression test). Under extension condition, the stress-strain curves show less non-linearly. For all stress paths, the strain at failure clearly increase with σ_3 and σ_m.
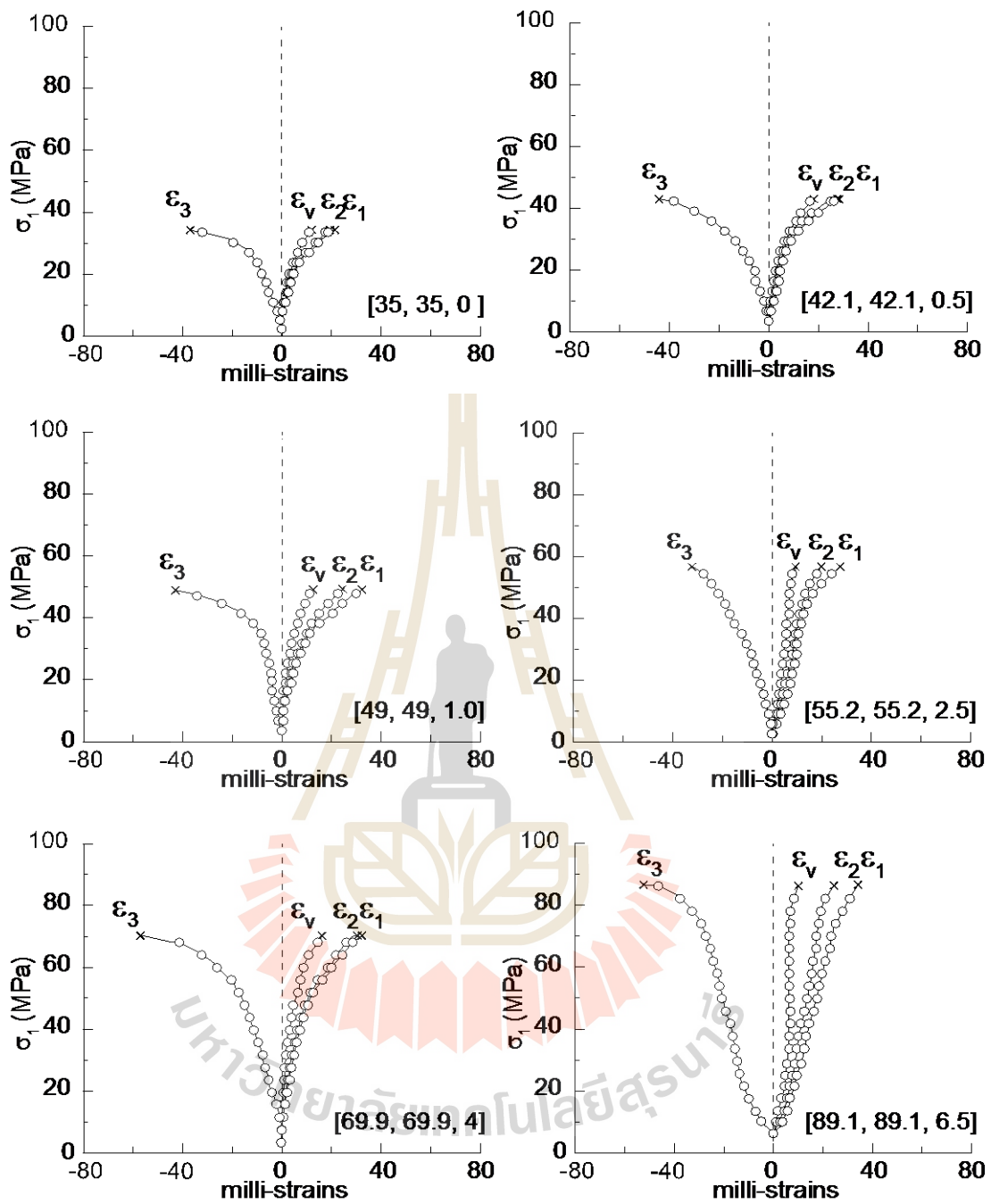
Figure 5.5 Stress-strain curves for triaxial extension test stress path 3.1 constant σ_3.

The numbers in the bracket represent $[\sigma_1, \sigma_2, \sigma_3]$ at failure.
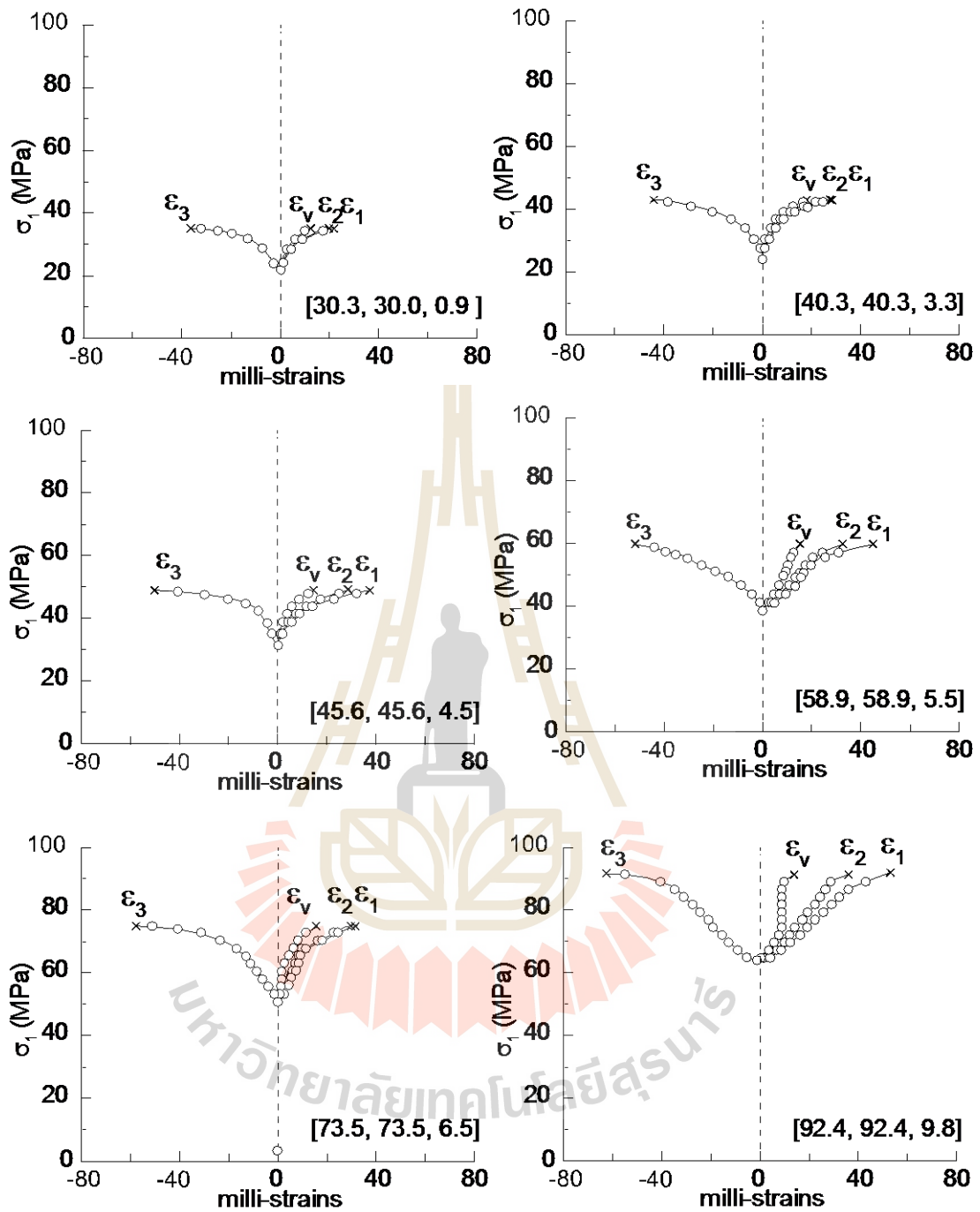
Figure 5.6 Stress-strain curves for triaxial extension test stress path 3.2 constant σ_m.

The numbers in the bracket represent $[\sigma_1, \sigma_2, \sigma_3]$ at failure.

Table 5.3 Strength results of triaxial extension tests (scheme 3).

Stress path (3.1) (constant σ_3)		Stress path (3.2) (constant σ_m)	
σ_3 (MPa)	$\sigma_1 = \sigma_2$ (MPa)	σ_3 (MPa)	$\sigma_1 = \sigma_2$ (MPa)
0.0	35.0	0.9	30.3
0.5	42.1	3.3	40.3
1.0	49.0	4.5	45.6
2.5	55.2	5.5	58.9
4.0	69.9	6.5	73.5
6.5	89.1	9.8	92.4
8.0	112.0	11.9	106.7
10.0	127.0	12.9	121.1

5.4 Octahedral shear strengths

For each specimen the octahedral shear stress at failure ($\tau_{oct,f}$) and at dilation ($\tau_{oct,d}$) are calculated from the principal stresses as follows:

$$\tau_{oct,f} = (1/3)[(\sigma_{1,f} - \sigma_{2,f})^2 + (\sigma_{1,f} - \sigma_{3,f})^2 + (\sigma_{2,f} - \sigma_{3,f})^2]^{1/2} \tag{5.3}$$

$$\tau_{oct,d} = (1/3)[(\sigma_{1,d} - \sigma_{2,d})^2 + (\sigma_{1,d} - \sigma_{3,d})^2 + (\sigma_{2,d} - \sigma_{3,d})^2]^{1/2} \tag{5.4}$$

$$\sigma_m = (\sigma_{1,f} + \sigma_{2,f} + \sigma_{3,f}) / 3 \tag{5.5}$$

$$\sigma_{m,d} = (\sigma_{1,d} + \sigma_{2,d} + \sigma_{3,d}) / 3 \tag{5.6}$$

where $\sigma_{1,f}$, $\sigma_{2,f}$ and $\sigma_{3,f}$ are the major, intermediate and minor principal stresses at the point where the failure occurs respectively. Three principal stresses equivalent to the dilation point are also represented by $\sigma_{1,d}$, $\sigma_{2,d}$ and $\sigma_{3,d}$.
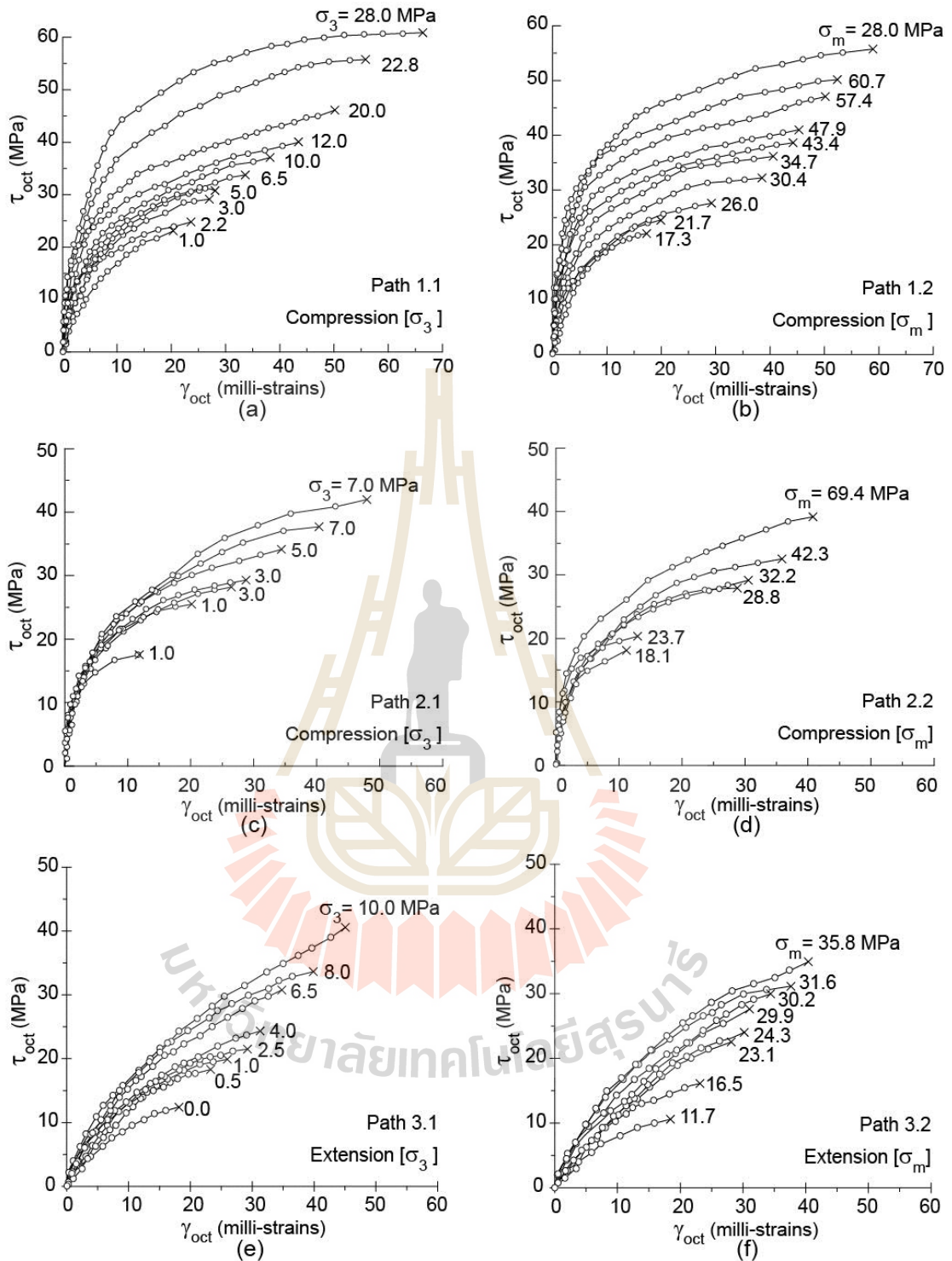
Figure 5.7 Octahedral shear stress – strain of all specimens for different stress paths.

Figure 5.8 shows how to determine the $\sigma_{1,d}$, $\sigma_{2,d}$ and $\sigma_{3,d}$ from the test results. Table 5.4 lists the mean stresses and octahedral shear strength values. For all stress paths, the octahedral shear stresses at failure and at dilation are plotted as a function of mean stress in Figure 5.9. The octahedral shear strength linearly increases with the mean stress for both failure and dilation. The dash and solid lines as shown in Figure 5.9 indicate the magnitudes of octahedral shear strength at failure ($\tau_{oct,f}$) and at dilation ($\tau_{oct,d}$) respectively.
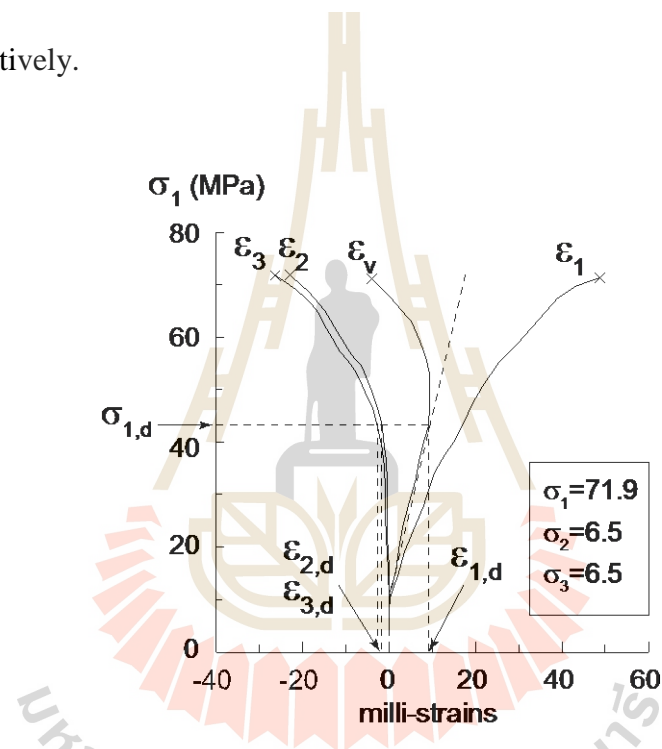
Figure 5.8 Stress-strain diagrams showing how principal stresses at dilation are determined from test results.

Table 5.4 Summary of strength results from different stress paths.

Test schemes	Stress path	Sample number	σ_1	σ_2	σ_3	σ_m	$\tau_{oct,f}$	$\sigma_{m,d}$	$\tau_{oct,d}$
Scheme 1 Compression ($\sigma_1 \neq \sigma_2 = \sigma_3$)	Path 1.1: Constant [σ_3]	TC-01	37.2	1.0	1.0	13.0	17.0	11.7	15.1
		TC-02	49.9	2.2	2.2	18.1	22.5	14.5	17.3
		TC-03	55.1	3.0	3.0	20.3	24.5	16.0	18.4
		TC-04	64.8	5.0	5.0	25.0	28.3	19.3	20.3
		TC-05	71.9	6.5	6.5	28.3	30.8	22.4	22.5
		TC-06	87.3	10.0	10.0	35.7	36.3	29.3	27.3
		TC-07	94.1	12.0	12.0	39.3	38.7	36.3	34.4
		TC-08	120.0	20.0	20.0	53.3	47.1	47.8	39.3
		TC-09	138.9	22.8	22.8	61.9	55.2	54.6	45.0
		TC-10	167.2	28.0	28.0	74.3	65.5	65.3	52.8
	Path 1.2: Constant [σ_m]	TC-11	24.9	0.25	0.25	8.5	11.7	8.5	11.0
		TC-12	29.4	1.1	1.1	10.5	13.3	10.5	12.4
		TC-13	44.4	3.3	3.3	17.0	19.4	17.0	17.0
		TC-14	56.0	6.5	6.5	23.0	23.3	23.0	20.5
		TC-15	64.2	7.6	7.6	26.5	26.7	26.5	23.7
		TC-16	71.4	10.8	10.8	31.0	28.5	31.0	25.4
		TC-17	88.1	15.2	15.2	39.5	34.4	39.5	31.5
		TC-18	110.8	19.5	19.5	50.0	43.1	50.0	38.9
		TC-19	129.7	25.2	25.2	60.0	49.3	60.0	43.8
		TC-20	148.5	30.4	30.4	70.0	55.7	70.0	49.7
Scheme 2 Polyaxial ($\sigma_1 \neq \sigma_2 \neq \sigma_3$)	Path 2.1: Constant [σ_3]	PX-01	30.2	7.0	1.0	17.1	12.5	11.8	11.5
		PX-02	55.5	35.0	1.0	32.8	22.3	25.3	20.5
		PX-03	65.1	25.0	3.0	33.2	25.7	28.9	23.5
		PX-04	75.2	40.0	3.0	39.3	29.4	36.7	27.0
		PX-05	90.6	50.0	5.0	48.1	35.0	44.9	31.6
		PX-06	99.5	50.0	7.0	51.7	37.8	48.3	34.0
		PX-07	119.5	65.0	7.0	60.5	45.9	59.6	42.1
	Path 2.2: Constant [σ_m]	PX-08	41.1	21.0	0.9	21.0	16.4	21.0	15.5
		PX-09	60.0	32.0	4.0	32.0	22.9	32.0	20.4
		PX-10	75.2	40.0	4.8	40.0	28.7	40.0	26.9
		PX-11	93.5	50.0	7.0	50.0	35.1	50.0	31.3
		PX-12	118.8	65.0	11.2	65.0	43.9	65.0	41.0
		PX-13	144.9	80.0	15.1	80.0	53.0	80.0	49.0

Table 5.4 Summary of strength results from different stress paths (cont.).

Test schemes	Stress path	Sample number	σ_1	σ_2	σ_3	σ_m	$\tau_{oct,f}$	$\sigma_{m,d}$	$\tau_{oct,d}$
Scheme 3 Extension ($\sigma_1 = \sigma_2 \neq \sigma_3$)	Path 3.1: Constant [σ_3]	TE-01	35.0	35.0	0.0	23.3	16.5	16.1	11.4
		TE-02	42.1	42.1	0.5	28.2	19.6	19.5	13.4
		TE-03	49.0	49.0	1.0	33.0	22.6	22.9	15.5
		TE-04	55.2	55.2	2.5	37.5	24.7	26.1	16.7
		TE-05	69.9	69.9	4.0	48.0	31.1	33.5	20.9
		TE-06	89.1	89.1	6.5	61.5	38.9	43.1	25.9
		TE-07	112.0	112.0	8.0	76.0	48.1	54.2	32.7
		TE-08	127.0	127.0	10.0	88.0	55.2	61.7	36.6
	Path 3.2: Constant [σ_m]	TE-09	30.3	30.3	0.9	20.5	13.9	20.5	11.7
		TE-10	40.3	40.3	3.3	28.0	17.4	28.0	14.6
		TE-11	45.6	45.6	4.5	32.0	19.4	32.0	16.2
		TE-12	58.9	58.9	5.5	41.0	25.2	41.0	21.0
		TE-13	73.5	73.5	6.5	51.0	31.6	51.0	26.4
		TE-14	92.4	92.4	9.8	65.0	38.9	65.0	32.4
		TE-15	106.7	106.7	11.9	75.0	44.7	75.0	37.1
		TE-16	121.1	121.1	12.9	85.0	51.0	85.0	42.4
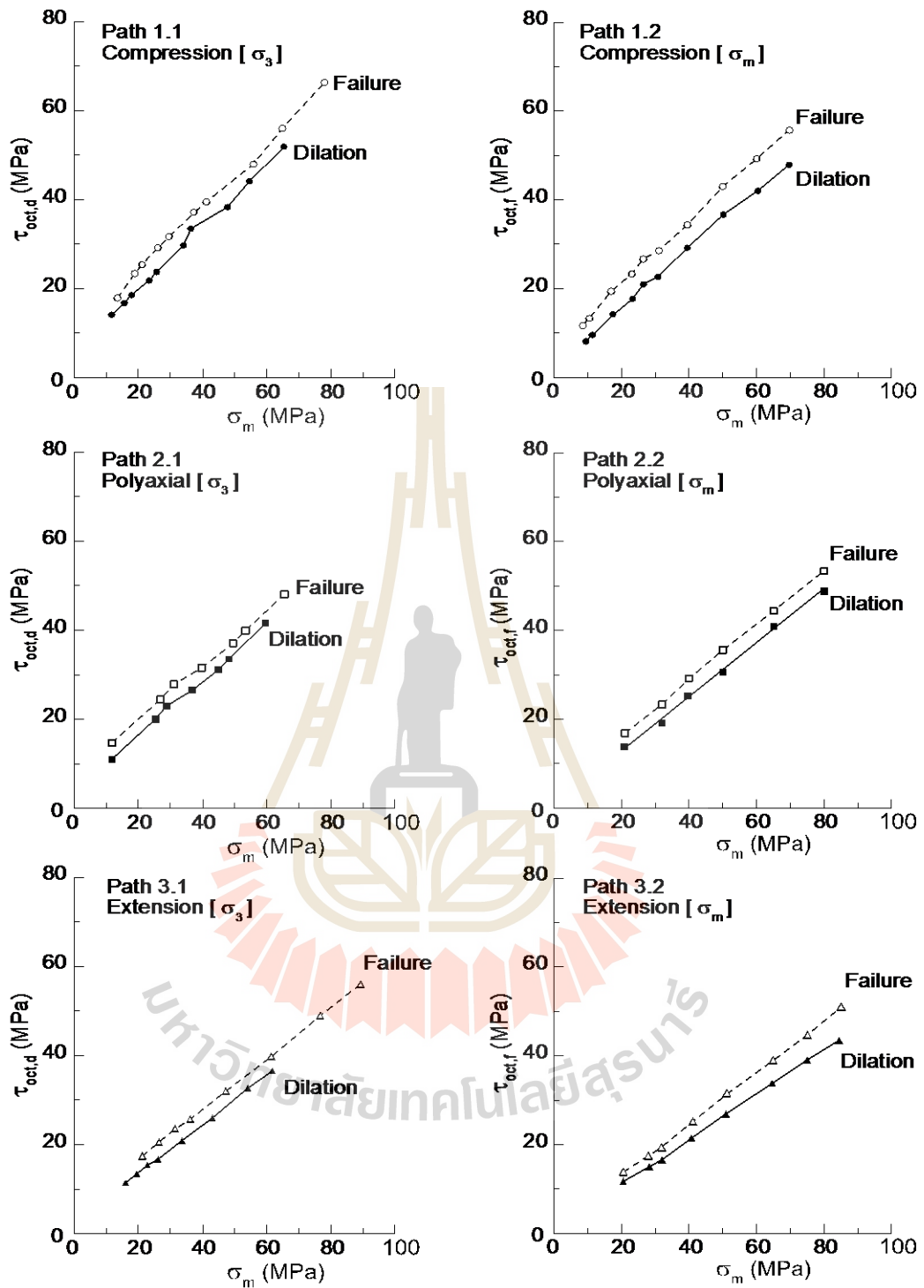
Figure 5.9 Octahedral shear stresses at failure (dash line) and at dilation (solid line)

as a function of mean stress for all stress paths.

5.5   Mode of failure

Post-failure observations suggest that compressive shear failures are predominant in the specimens tested under low σ_2 while splitting tensile fractures parallel to σ_1 and σ_2 directions dominate under higher σ_2. Table 5.5 summarizes mode of failure for each stress path. Stress path 1.1 provides the single shear fracture under low confining pressure and the multiple shear failures occur when confining pressure increases to 20 MPa. The compressive shear failure is the only one failure mode that presented on stress path 1.2.   Under a low σ_3 condition, few factures are observed from the surface on which σ_3 is applied for stress paths 2.1 and 2.2. The fracture patterns at the end of loading for stress path 3.1 show the extensile failures parallel to both σ_1 and σ_2 directions. For the stress path 3.2 the direction of extensile failure surface patterns is similar to that of stress path 3.1, but under low σ_3 the failure plane clearly inclines from the σ_1 and σ_2 axis.

The observed extensile fractures under relatively high σ_2 suggest that the fracture initiation has no influence from the friction at the loading interface in the σ_2 direction. As a result the increase of σ_1 with σ_2 should not be due to the interface friction. Figure 5.10 demonstrates the examples of the modes of failure and failure stresses for six stress paths.

Table 5.5 Summary of the mode of failure**.**

Stress path	σ_m (MPa)	σ_3 (MPa)	Mode of failure
Path 1.1: Compression Constant σ_3	-	1.0	Single shear plane
	-	2.2	Single shear plane
	-	3.0	Single shear plane
	-	5.0	Single shear plane
	-	6.5	Single shear plane
	-	10.0	Single shear plane
	-	12.0	Single shear plane
	-	20.0	Multiple shear plane
	-	22.8	Multiple shear plane
	-	28.0	Multiple shear plane
Path 1.2: Compression Constant σ_m	8.5	-	Single shear plane
	10.5	-	Single shear plane
	17.0	-	Single shear plane
	23.0	-	Single shear plane
	26.5	-	Single shear plane
	31.0	-	Single shear plane
	39.5	-	Single shear plane
	50.0	-	Single shear plane
	60.0	-	Single shear plane
	69.8	-	Single shear plane
Path 2.1: Polyaxial Constant σ_3	-	1.0	Single shear plane
	-	1.0	Single shear plane
	-	3.0	Single shear plane
	-	3.0	Single shear plane
	-	5.0	Single shear plane
	-	7.0	Single shear plane
	-	7.0	Single shear plane

Table 5.5 Summary of the mode of failure (cont.).

Stress path	σ_m (MPa)	σ_3 (MPa)	Mode of failure
Path 2.2: Polyaxial Constant σ_m	21.0	-	Single shear plane
	32.0	-	Single shear plane
	40.0	-	Single shear plane
	50.0	-	Single shear plane
	65.0	-	Single shear plane
	80.0	-	Single shear plane
Path 3.1: Extension Constant σ_3	-	0.0	Extensile failure
	-	0.5	Extensile failure
	-	1.0	Extensile failure
	-	2.5	Extensile failure
	-	4.0	Extensile failure
	-	6.5	Extensile failure
	-	8.0	Extensile failure
	-	10.0	Extensile failure
Path 3.2: Polyaxial Constant σ_m	20.5	-	Single shear plane
	28.0	-	Single shear plane
	31.9	-	Extensile failure
	41.1	-	Extensile failure
	51.2	-	Extensile failure
	64.9	-	Extensile failure
	75.1	-	Extensile failure
	85.0	-	Extensile failure
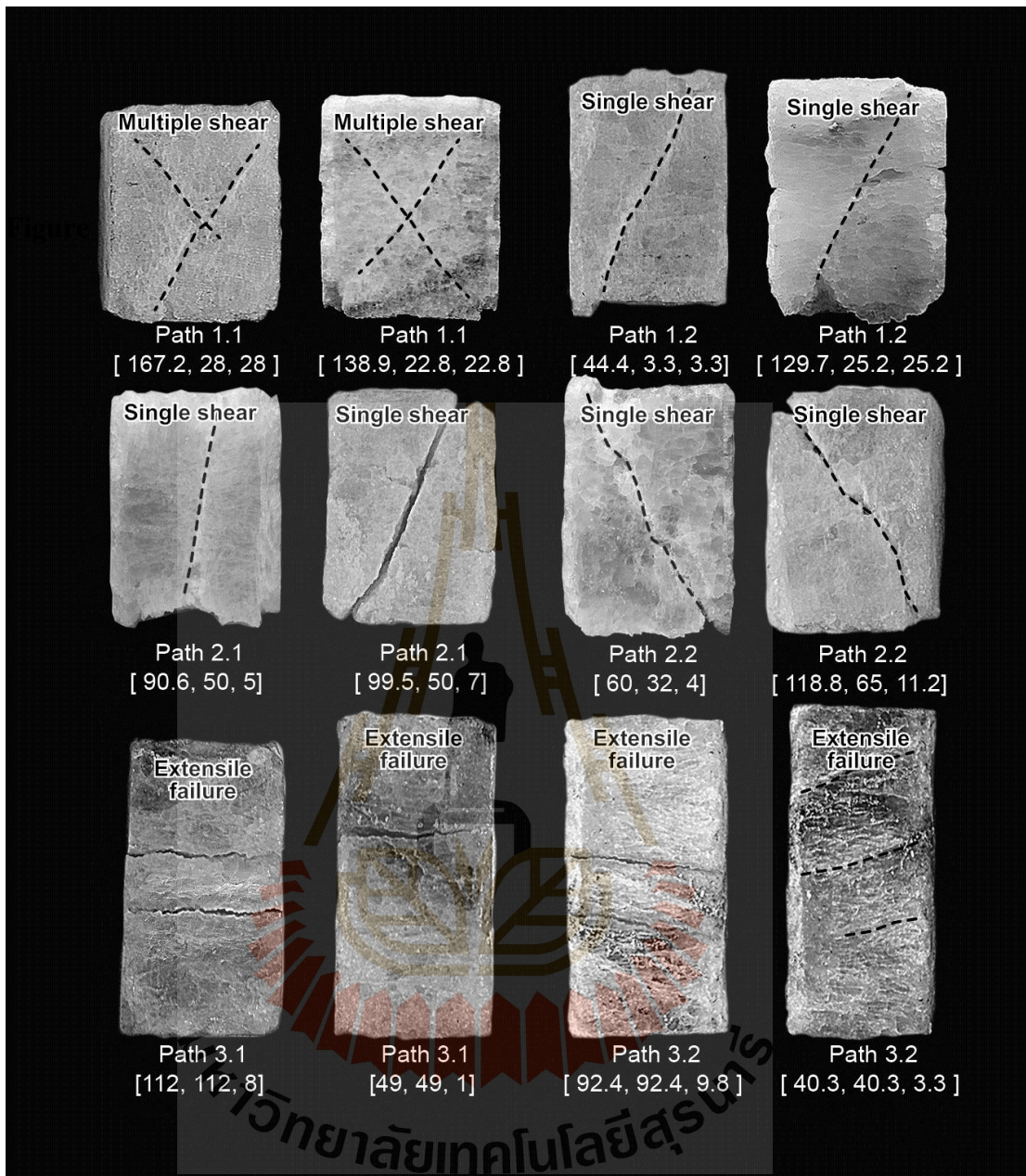
Figure 5.10 Some post-tested specimens. Numbers in blankets indicate [$\sigma_1,\sigma_2,\sigma_3$]

at failure.

5.6 Elastic parameters

The elastic parameters of the salt are determined from the linear portion of the stress-strain curves (before dilation occurs). Assuming that the salt specimen is isotropic, the shear (rigidity) modulus (G), Lame′ constant (λ), Young's modulus (E) and Poisson's ratio (ν) can be calculated from the following relations (Jaeger et al., 2007):

$$G = (1/2) \, (\tau_{oct,e}/\gamma_{oct,e}) \tag{5.4}$$

$$3\sigma_{m,e} = (3\lambda + 2G) \, \varepsilon_{v,e} \tag{5.5}$$

$$E = 2G \, (1 + \nu) \tag{5.6}$$

$$\nu = \lambda/(2(\lambda + G)) \tag{5.7}$$

where $\tau_{oct,e}$, $\gamma_{oct,e}$, $\sigma_{m,e}$ and $\varepsilon_{v,e}$ are the octahedral shear stress and strain, mean stress, and volumetric strain at the point where the elastic parameters are determined.

The elastic parameters are calculated for the three-dimensional principal stress-strain relations. An attempt is made to calculate the elastic moduli along the three loading directions. It is assumed here that the Poisson's ratio of each rock type is the same for all principal planes ($\nu = 0.36$). The elastic moduli along the major, intermediate and minor principal directions can be calculated by (Jaeger et al., 2007):

$$\varepsilon_1 = \sigma_1/ E_1 - \nu \, (\sigma_2/ E_2 + \sigma_3/ E_3) \tag{5.8}$$

$$\varepsilon_2 = \sigma_2/ E_2 - \nu \, (\sigma_1/ E_1 + \sigma_3/ E_3) \tag{5.9}$$

$$\varepsilon_3 = \sigma_3/E_3 - \nu(\sigma_1/E_1 + \sigma_2/E_2) \qquad (5.10)$$

where ε_1, ε_2 and ε_3 are the major, intermediate and minor principal strains, and E_1, E_2 and E_3 are the elastic moduli along the major, intermediate and minor directions. Table 5.6 summarizes these stress and strain values and their corresponding elastic parameters for each specimen. The calculation results are shown in Figure 5.11 which suggest that the elastic moduli along the principal directions are relatively similar, with the standard deviation of about ± 2.0 and ± 1.6. This implies that all rock specimens are isotropic. The discrepancies shown in these figures are probably due to the intrinsic variability of among salt specimens.
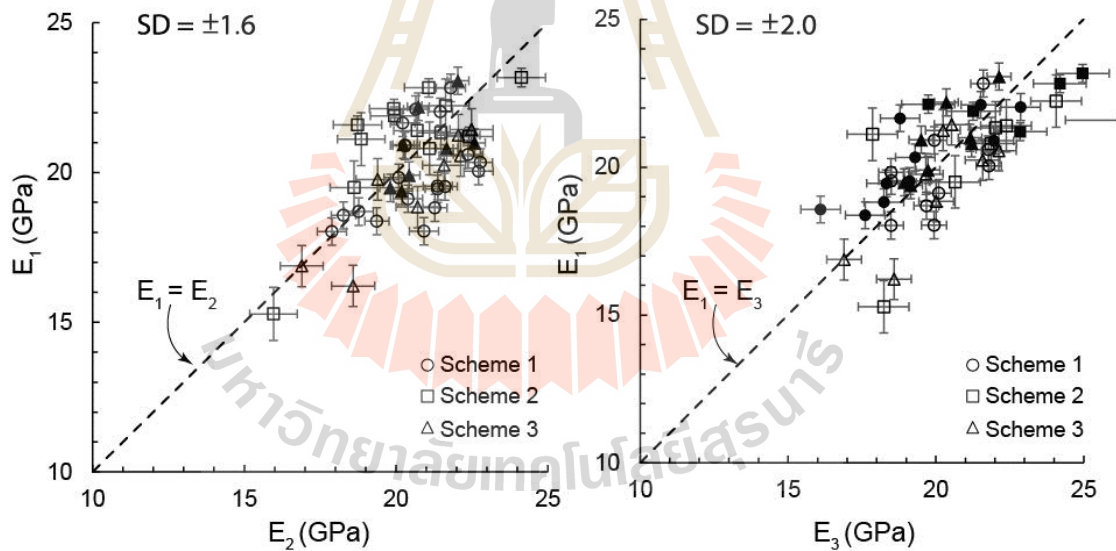
Figure 5.11 Elastic modulus calculated along the major principal axis as a function of intermediate and minor principal axes.

Table 5.6 Summary of the elastic parameters**.**

| Stress path | Sample number | $\varepsilon_{v,e}$ ($\times 10^{-3}$) | E | | | | G | λ | ν |
			E_1	E_2	E_3	Avg.			
Path 1.1 Constant [σ_3]	TC-01	0.70	20.0	21.8	22.7	21.52	7.79	25.11	0.38
	TC-02	0.90	19.1	20.1	20.4	19.87	7.50	13.92	0.33
	TC-03	0.77	18.0	18.5	17.9	18.13	6.73	15.19	0.35
	TC-04	1.50	19.8	18.5	20.1	19.47	7.28	15.05	0.34
	TC-05	1.20	18.7	19.7	18.8	19.05	7.55	18.22	0.36
	TC-06	2.20	20.6	21.8	22.4	21.59	8.02	18.00	0.35
	TC-07	3.80	22.8	21.6	25.6	22.08	7.90	13.53	0.31
	TC-08	4.50	18.0	19.9	20.9	19.63	6.96	31.61	0.41
	TC-09	5.69	19.5	18.5	21.4	19.80	6.88	49.44	0.44
	TC-10	8.00	20.9	20.0	20.3	20.39	7.72	13.78	0.32
Path 1.2 Constant [σ_m]	TC-11	0.76	22.0	22.9	21.5	22.12	7.86	34.41	0.41
	TC-12	0.83	22.1	21.5	20.7	21.43	8.04	16.06	0.33
	TC-13	0.95	20.9	22.0	20.3	21.05	7.58	26.23	0.39
	TC-14	2.30	18.6	16.1	18.3	17.65	6.53	15.40	0.35
	TC-15	3.21	19.5	18.3	21.4	19.72	6.80	27.95	0.40
	TC-16	4.00	18.8	18.2	21.3	19.45	6.84	36.90	0.42
	TC-17	5.10	19.5	19.1	21.6	20.08	6.65	15.78	0.34
	TC-18	6.40	21.7	18.8	20.2	20.22	6.52	22.58	0.38
	TC-19	8.20	20.3	19.3	22.8	20.80	7.38	33.57	0.41
	TC-20	8.66	18.4	17.6	19.4	18.45	6.55	29.13	0.41
Path 2.1 Constant [σ_3]	0.50	22.2	24.1	21.6	22.64	7.98	41.24	0.42	0.50
	2.50	15.3	18.2	16.0	16.49	6.31	10.06	0.31	2.50
	2.64	22.4	22.4	20.7	21.49	7.56	40.89	0.42	2.64
	4.20	21.3	22.0	21.5	21.61	8.03	17.92	0.35	4.20
	5.86	20.8	21.9	21.1	21.26	7.35	60.92	0.45	5.86
	9.00	21.1	17.9	18.9	19.27	6.86	29.22	0.40	9.00
	8.50	19.5	20.7	18.6	19.59	6.99	28.42	0.40	8.50

Table 5.6 Summary of the elastic parameters (cont.).

Stress path	Sample number	$\varepsilon_{v,e}$ ($\times 10^{-3}$)	E				G	λ	ν
			E_1	E_2	E_3	Avg.			
Path 2.2 Constant [σ_m]	PX-08	1.80	22.1	19.7	19.9	20.60	7.61	18.26	0.35
	PX-09	2.20	21.9	21.3	20.0	21.03	7.97	14.15	0.32
	PX-10	3.76	21.6	25.3	18.7	21.87	8.24	15.64	0.33
	PX-11	4.20	22.8	24.2	21.1	22.70	8.53	16.74	0.33
	PX-12	7.02	22.2	22.9	20.4	22.15	8.20	19.18	0.35
	PX-13	8.95	23.2	25.0	24.1	24.09	8.49	43.75	0.42
Path 3.1 Constant [σ_3]	TE-01	0.98	19.8	19.7	19.4	19.61	7.05	24.95	0.39
	TE-02	1.46	21.2	20.2	22.1	21.18	7.50	34.82	0.41
	TE-03	2.08	20.2	21.6	21.6	21.13	7.58	28.03	0.39
	TE-04	3.72	21.4	20.5	22.5	21.08	7.66	23.60	0.38
	TE-05	4.50	20.6	22.1	22.1	21.61	7.59	41.56	0.42
	TE-06	3.83	18.8	20.0	20.7	19.86	7.96	16.78	0.35
	TE-07	5.56	16.2	18.6	18.6	17.79	7.23	13.11	0.33
	TE-08	4.52	16.9	16.9	16.9	16.89	6.59	19.54	0.38
Path 3.2 Constant [σ_m]	TE-09	1.32	20.8	21.2	21.7	21.23	8.39	21.06	0.37
	TE-10	1.34	20.9	19.5	20.2	20.22	7.69	34.47	0.41
	TE-11	2.05	21.0	21.2	22.6	21.58	8.56	20.37	0.36
	TE-12	2.53	19.5	18.9	19.8	19.41	7.56	23.16	0.38
	TE-13	2.92	19.4	19.1	20.2	19.57	7.69	20.93	0.37
	TE-14	2.17	22.2	20.4	20.7	21.09	7.92	46.37	0.43
	TE-15	2.63	23.1	22.1	22.0	22.41	8.58	34.78	0.41
	TE-16	4.06	19.9	19.7	20.4	20.02	7.85	22.10	0.38

CHAPTER VI

STRENGTH CRITERIA

6.1   Introduction

This chapter describes the strength and dilation criteria under multi-axial compression condition. The study offers two empirical criteria, octahedral shear strength and mean stress criterion and strain energy density criterion. An attempt here is to correlate the rock salt strengths with the stress and strain conditions in terms of the octahedral shear strength and distortional strain energy density for all stress paths.

6.2   Lode parameter

The Lode parameter (μ) proposed by Lode (1925), who tested tubes of steel, copper, and nickel under various combinations of longitudinal tension and internal hydrostatics pressure. Lode devised a very sensitive method of differentiating by determining the effect of the intermediate principal stress on yielding. Here, the Lode parameter has been used to define the effect of σ_2 on the strength and deformation of the salt specimens. This parameter has values ranging from -1 to $+1$. The parameter equals to 1 for triaxial compression,-1 for triaxial extension and between -1 to 1 for polyaxial compression. It can be calculated by using the following relation (Lode, 1925).

$$\mu = (2\sigma_2 - \sigma_3 - \sigma_1) / (\sigma_3 - \sigma_1) \tag{6.1}$$

where σ_1, σ_2, and σ_3 are major, intermediate and minor principal stresses applied on the salt. The μ is thus the ratio of the difference between the intermediate stress and the average of largest and smallest stresses to half the difference between the largest and smallest stresses. This parameter will be used here to incorporate into the strength and dilation criteria to be developed.

6.3 Octahedral shear strength and mean stress relation

From the test results in chapter V, the variation of shear strengths can be observed from the τ_{oct} - σ_m diagram, as shown in Figure 6.1. The octahedral shear stresses at failure ($\tau_{oct,f}$) and at dilation ($\tau_{oct,d}$) of rock salt linearly increase with increasing mean stress. The linear relation between the octahedral shear strength and the mean stress at failure and can be best represented by:

$$\tau_{oct,f} = A \cdot \sigma_m + B \tag{6.2}$$

$$\tau_{oct,d} = A' \cdot \sigma_{m,d} + B' \tag{6.3}$$

where A, A' B, and B' are empirical parameters for mean stress multipliers and octahedral shear strength constants for the salt at failure and at dilation, respectively. Good correlations and obtained for all stress paths ($R^2 > 0.95$). Figure 6.1 presents the octahedral shear strength-mean stress diagrams fitted by the equations above for all stress paths. For the Maha Sarakham salt the parameters A, A', B and B' are defined by the regression analysis as summarized in Table 6.1. These parameters trend to decreases when the stress states change from triaxial compression, polyaxial
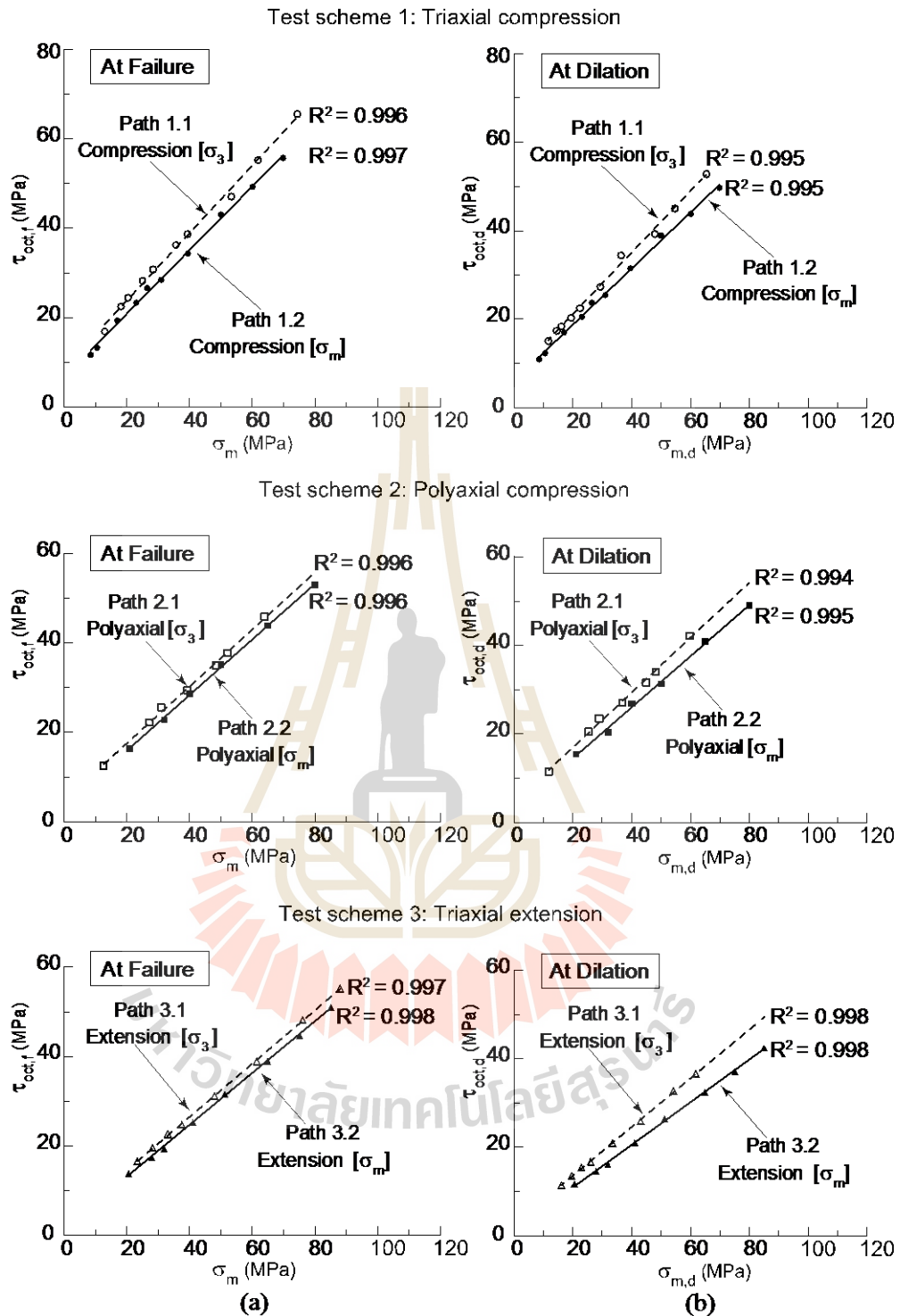
Figure 6.1 Octahedral shear stresses as a function of mean stresses at failure and at dilation for all stress paths.

Table 6.1 Summary of A, B, A′ and B′ parameters.

Test schemes	Stress paths	At Failure			At Dilation		
		A	**B**	R^2	**A′**	**B′**	R^2
Triaxial compression	Path 1.1	0.756	8.68	0.996	0.696	7.16	0.995
	Path 1.2	0.714	6.57	0.997	0.635	6.06	0.995
Polyaxial compression	Path 2.1	0.637	4.80	0.996	0.620	4.54	0.994
	Path 2.2	0.623	3.45	0.996	0.577	2.96	0.995
Triaxial extension	Path 3.1	0.596	2.64	0.997	0.551	2.55	0.998
	Path 3.2	0.580	1.43	0.998	0.480	1.36	0.998

to extension conditions. The stress paths where the σ_3 are maintained constant always shows higher strengths and dilation than those with constant σ_m.

6.4 Octahedral shear strength - Lode parameter criterion

An empirical criterion is proposed to predict the octahedral shear strengths under various stress paths and mean stresses. The relation derived by taking the Lode parameter into consideration. Figures 6.2 through 6.5 show the octahedral shear stress-Lode parameter diagrams at failure and at dilation for constant σ_3 and constant σ_m test conditions. The italic numbers in their Figures represent the magnitudes of σ_m where their locations indicate the corresponding magnitudes of τ_{oct} and μ at failure and at dilation. Set of empirical (linear) equations can be used to determine the variation of octahedral shear stress with Lode parameter at failure and at dilation for
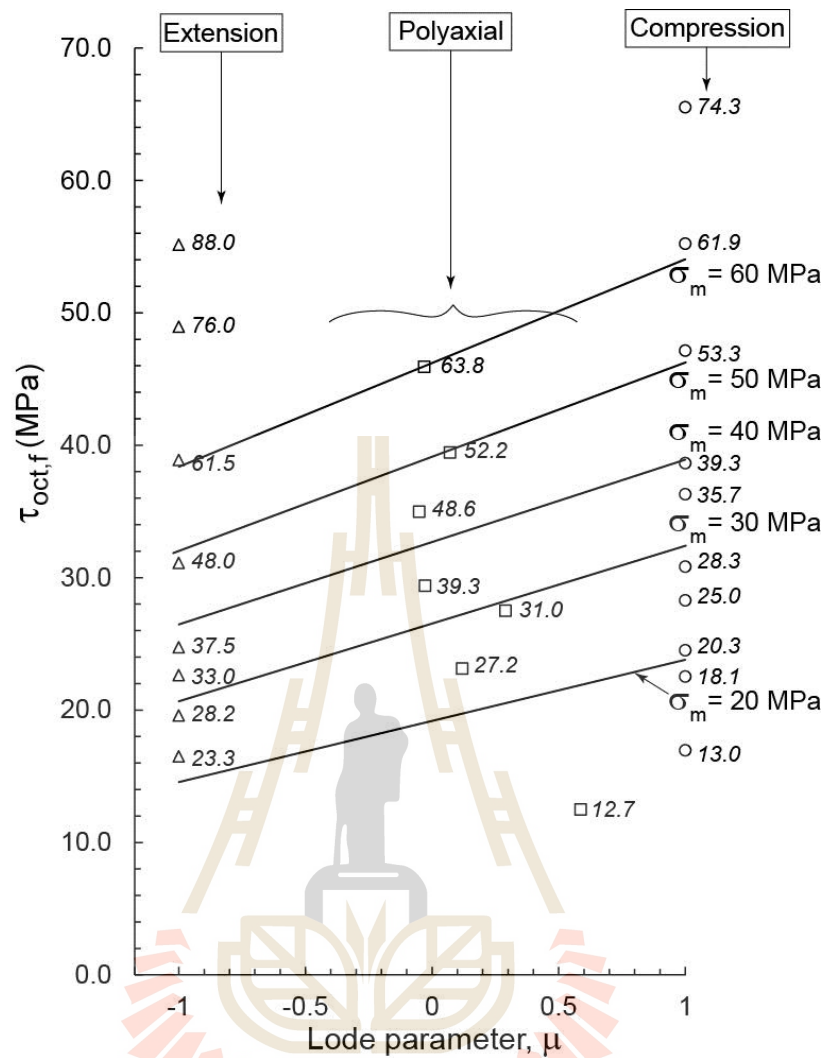
Figure 6.2 Octahedral shear stress at failure ($\tau_{oct,f}$) as a function of Lode parameter (μ) for various mean stresses under constant σ_3 condition. The numbers denote σ_m in MPa for each data point.
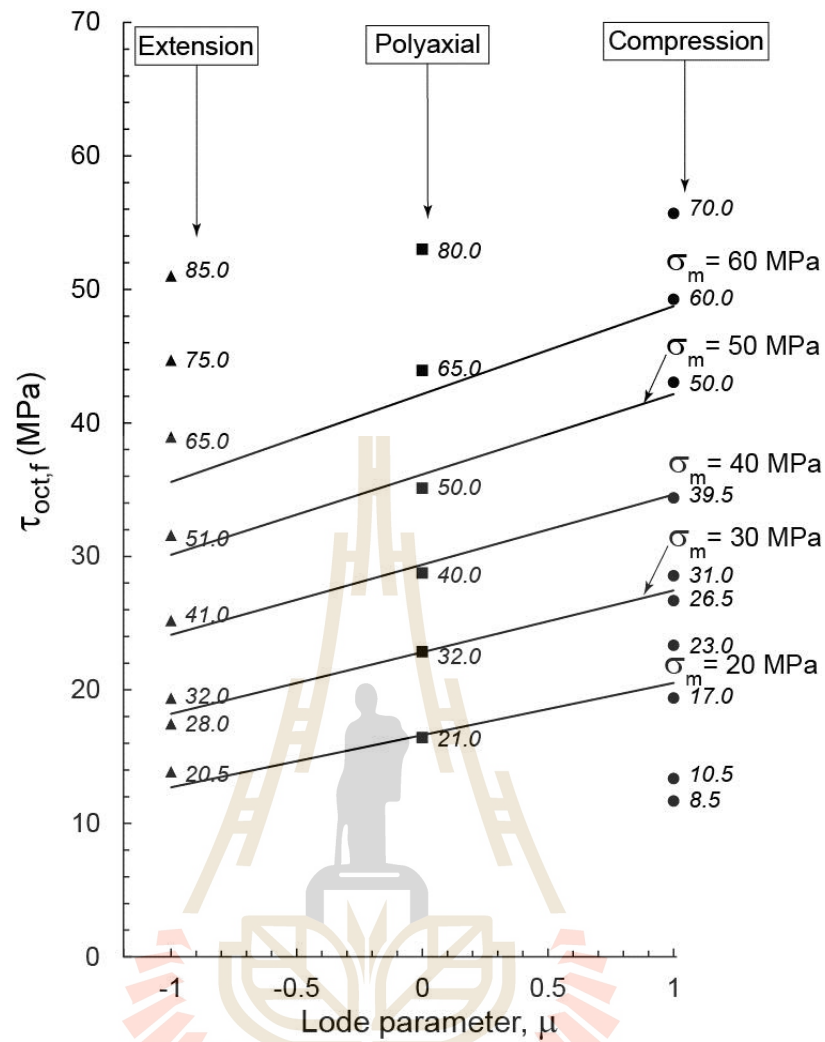
Figure 6.3 Octahedral shear stress at failure ($\tau_{oct,f}$) as a function of Lode parameter (μ) for various mean stresses under constant σ_m condition. The numbers denote σ_m in MPa for each data point.
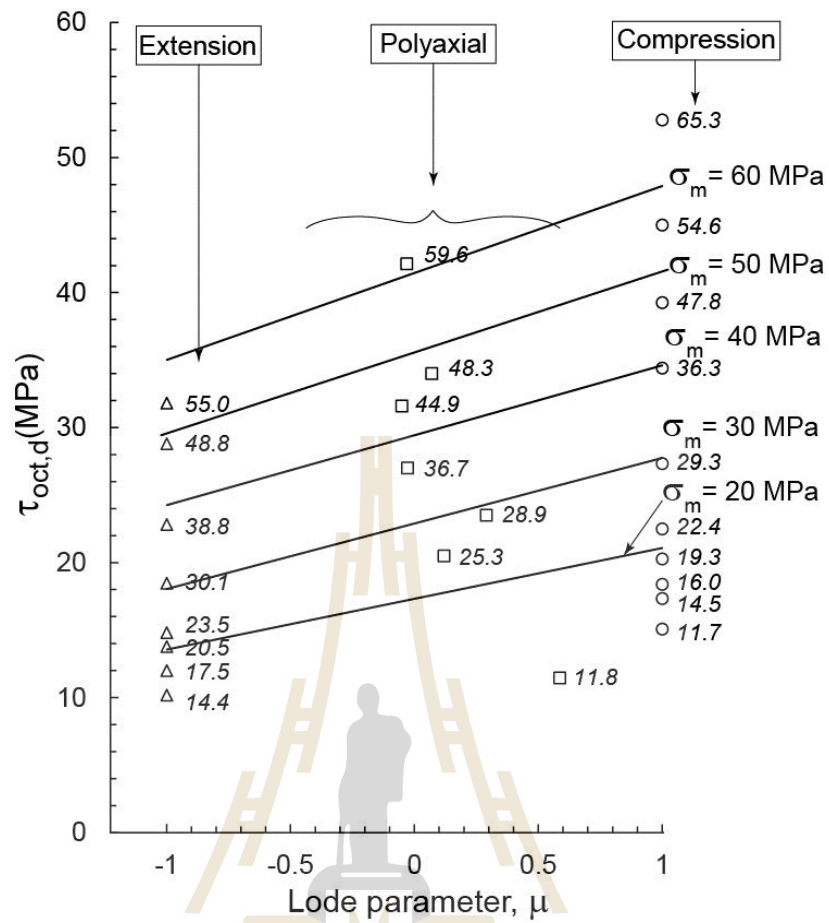
Figure 6.4 Octahedral shear stress at dilation ($\tau_{oct,d}$) as a function of Lode parameter

(μ) for various mean stresses under constant σ_3 condition. The numbers

denote σ_m in MPa for each data point.
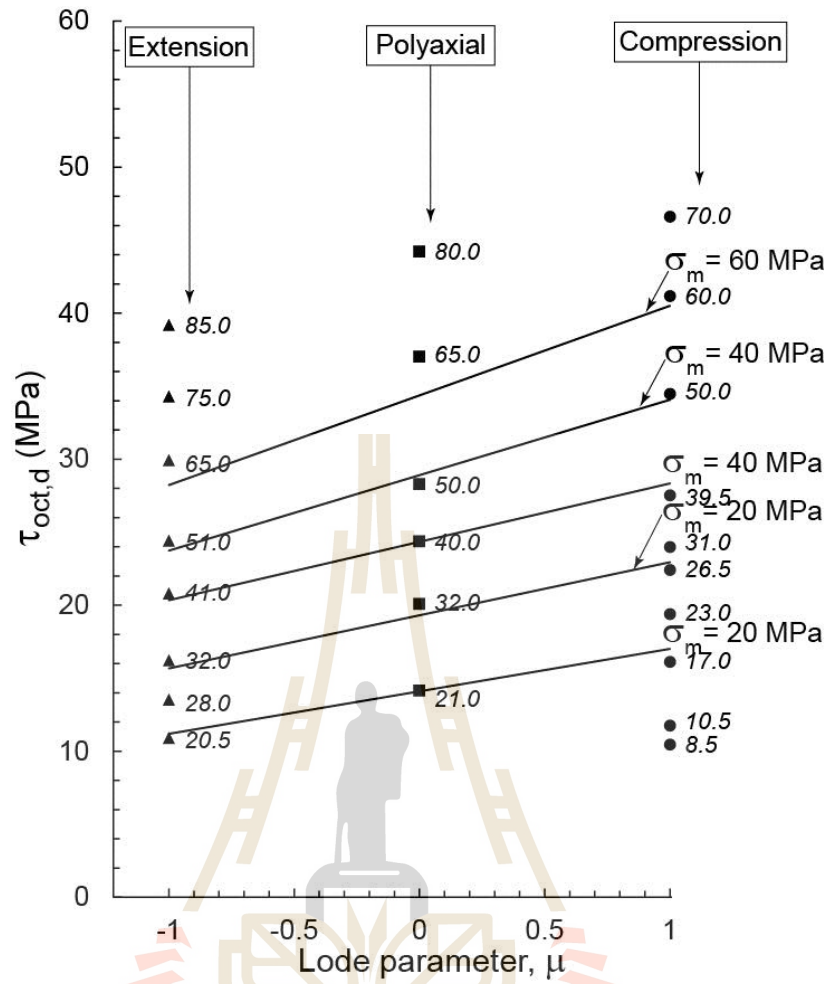
Figure 6.5 Octahedral shear stress at dilation ($\tau_{oct,d}$) as a function of Lode parameter

(μ) for various mean stresses under constant σ_m condition. The numbers

denote σ_m in MPa for each data point.

the selected mean stress magnitudes of 20, 30, 40, 50 and 60 MPa.

$$\tau_{oct,f} = \alpha \cdot \mu + \beta \tag{6.4}$$

$$\tau_{oct,d} = \alpha' \cdot \mu + \beta' \tag{6.5}$$

where α, α', β and β' are Lode parameter multiplier and octahedral shear stress constant for the salt at failure and at dilation, respectively. The diagrams as shown in Figures 6.2 through 6.5 represent the interpolation lines between the data points obtained from testing. These constants are defined by regression analysis of the above equations. They depend on the magnitude of σ_m:

$$\alpha = \alpha_1 \cdot \sigma_m + \alpha_2 \tag{6.6}$$

$$\alpha' = \alpha'_1 \cdot \sigma_{m,d} + \alpha'_2 \tag{6.7}$$

$$\beta = \beta_1 \cdot \sigma_m + \beta_2 \tag{6.8}$$

$$\beta' = \beta'_1 \cdot \sigma_{m,d} + \beta'_2 \tag{6.9}$$

where α_1, α_2, α'_1, and α'_2 are the regression analysis constants of the Lode parameter multiplier for failure and dilation criteria. The parameters β_1, β_2, β'_1, and β'_2 are the regression analysis constant of octahedral shear constant.

By substituting the parameters in equations (6.6) through (6.9) into equations (6.4) and (6.5), the failure and dilation criteria of salt for constant σ_3 and constant σ_m conditions can be presented in the forms of the Lode parameter and mean stress.

$$\tau_{oct,f} = (\alpha_1 \cdot \sigma_m + \alpha_2) \cdot \mu + (\beta_1 \cdot \sigma_m + \beta_2) \tag{6.10}$$

$$\tau_{oct,d} = (\alpha'_1 \cdot \sigma_{m,d} + \alpha'_2) \cdot \mu + (\beta'_1 \cdot \sigma_{m,d} + \beta'_2) \tag{6.11}$$

Table 6.2 gives numerical values of these empirical constants. For all stress paths and loading schemes the salt strengths and dilations increase with increasing the Lode parameters. The proposed linear relations agree well with the test results, as evidenced by the good coefficients of correlation for all curves ($R^2 > 0.9$).

Table 6.2 Numerical values of the empirical constants for octahedral shear strength and dilation criteria.

Stress conditions	At Failure					At Dilation				
	α_1,	α_2	β_1	β_2	R^2	α'_1	α'_2	β'_1	β'_2	R^2
Constant σ_3	0.081	3.02	0.676	5.67	0.985	0.072	2.68	0.653	4.07	0.965
Constant σ_m	0.067	2.57	0.621	3.75	0.987	0.061	2.46	0.564	3.46	0.992

6.5 Strain energy density principle

The strain energy density principle is applied here to describe the salt strength and deformability under different stress paths. The distortional strain energy at failure (W_d) and at dilation ($W_{d,d}$) can be calculated from the octahedral shear stresses and shear modulus (G) for each salt specimen (Table 6.3) using the following equation (Jaeger et al., 2007):

$$W_d = (3/4G) \cdot \tau_{oct,f}^2 \tag{6.12}$$

$$W_{d,d} = (3/4G) \cdot \tau_{oct,d}^{2} \qquad (6.13)$$

where $\tau_{oct,f}$ and $\tau_{oct,d}$ are octahedral shear stress at failure and at dilation, G is shear modulus for each specimen.

The distortion strain energy at failure (W_d) and at dilation ($W_{d,d}$) can be presented as a function of the mean strain energy density at failure (W_m) and at dilation ($W_{m,d}$) which can be calculated from the mean stress at failure (σ_m) and at dilation ($\sigma_{m,d}$) and bulk modulus (K) of the salt as follows:

$$W_m = \sigma_m^{2} / 2K \qquad (6.14)$$

$$W_{m,d} = \sigma_{m,d}^{2} / 2K \qquad (6.15)$$

Figure 6.6 plots the relations between W_d and W_m at failure and at dilation for all stress paths which can be represented by:

$$W_d = C \cdot W_m + D \qquad (6.16)$$

$$W_{d,d} = C' \cdot W_{m,d} + D' \qquad (6.17)$$

where C, C′, D, and D′ are empirical parameters for mean strain energy density multipliers and distortional strain energy density constant for strength and dilation criteria. Table 6.3 shows the strain energy density at failure and at dilation for each specimens.

Table 6.3 Strain energy density at failure and at dilation for each specimens.

Test schemes	Stress path	μ	$W_{m,d}$ (kPa)	$W_{d,d}$ (kPa)	W_m (kPa)	$W_{d,f}$ (kPa)
Scheme 1 Compression ($\sigma_1 \neq \sigma_2 = \sigma_3$)	Path 1.2: Constant [σ_m]	1.0	2.0	22.0	2.0	28.0
			2.9	29.5	4.6	49.8
			3.6	33.2	5.8	59.0
			5.2	40.3	8.8	78.5
			7.0	49.7	11.2	93.3
			12.1	73.4	17.8	129.3
			18.5	116.3	21.7	146.7
			32.0	151.4	39.9	218.2
			41.8	198.8	53.7	299.5
			59.8	273.6	77.5	421.5
	Path 1.2: Constant [σ_m]	1.0	1.0	11.8	1.0	13.4
			1.6	15.0	1.6	17.5
			4.0	28.3	4.0	36.9
			7.4	41.3	7.4	53.4
			9.8	55.2	9.8	69.9
			13.5	63.5	13.5	80.0
			21.9	97.2	21.9	116.0
			35.0	148.7	35.0	181.9
			50.5	188.5	50.5	238.2
			68.2	242.1	68.2	304.4
Scheme 2 Polyaxial ($\sigma_1 \neq \sigma_2 \neq \sigma_3$)	Path 2.1: Constant [σ_3]	0.7	1.9	12.9	2.2	18.4
		-0.1	9.0	41.3	10.3	58.6
		0.3	11.7	54.3	13.5	77.6
		0.0	18.9	71.6	21.7	101.8
			28.3	98.1	33.0	144.2
		0.1	32.7	113.6	38.1	168.3
		-0.2	49.8	174.2	57.1	225.0
	Path 2.2: Constant [σ_m]	0.0	6.2	23.6	6.2	26.5
			14.4	40.9	14.4	51.3
			22.4	70.9	22.4	81.1
			35.0	96.3	35.0	121.0
			59.2	164.7	59.2	189.4
			89.7	235.6	89.7	275.7

Table 6.3 Strain energy density at failure and at dilation for each specimens (cont.).

Test schemes	Stress path	μ	$W_{m,d}$ (kPa)	$W_{d,d}$ (kPa)	W_m (kPa)	$W_{d,f}$ (kPa)
Scheme 3 Extension $(\sigma_1 = \sigma_2 \neq \sigma_3)$	Path 3.1: Constant $[\sigma_3]$	-1.0	3.6	12.7	7.6	26.7
			5.3	17.7	11.1	37.7
			7.3	23.5	15.3	50.3
			9.6	27.4	19.7	60.1
			15.8	42.8	32.3	95.0
			26.0	65.7	53.0	148.5
			41.1	104.7	81.0	227.2
			53.4	131.4	108.6	298.6
	Path 3.2: Constant $[\sigma_m]$	-1.0	5.9	13.5	5.9	18.9
			11.0	20.9	11.0	29.9
			14.3	25.6	14.3	36.9
			23.7	43.3	23.7	62.2
			36.7	68.4	36.7	97.9
			59.0	103.1	59.0	148.8
			79.1	135.4	79.1	196.1
			101.4	176.8	101.4	255.4
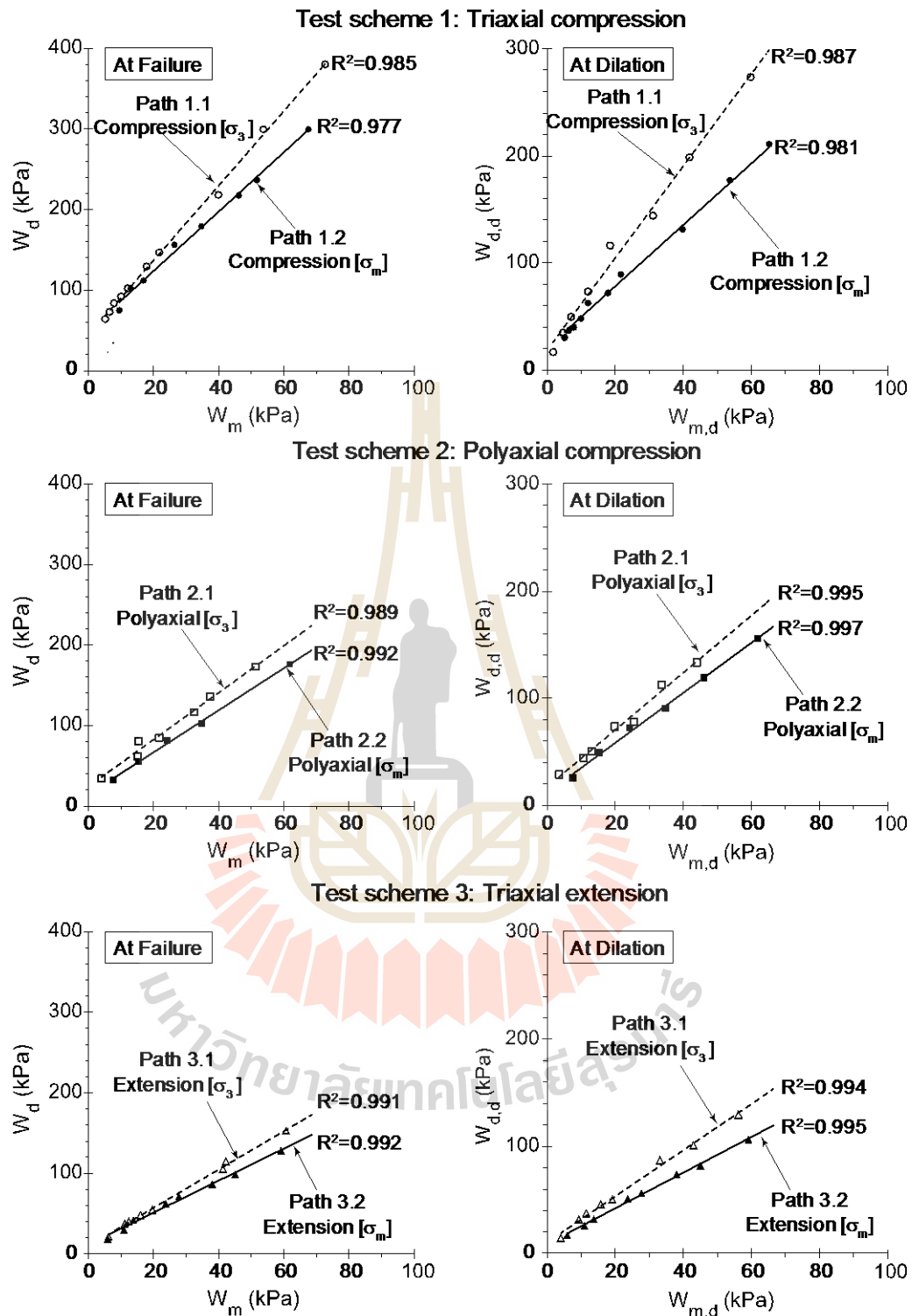
Figure 6.6 Distortional strain energy density as a function of mean mean strain energy density at failure and at dilation for all stress paths.

It is assumed that under a given mean strain energy the distortional strain energy required to dilate and to fail the specimens is constant. The results shown in Figure 6.6 indicate that the distortional strain energy linearly increases with the mean strain energy for all stress paths. Under the same test scheme the distortional strain energy on stress path with constant σ_3 yield higher values than on the stress path with constant σ_m. For the Maha Sarakham salt the C, C′, D and D′ parameters for all stress paths are defined by the regression analysis as summarized in Table 6.4.

Table 6.4 Summary of C, D, C′ and D′ parameters.

Test scheme	Stress paths	At Failure			At Dilation		
		C	**D**	**R²**	**C′**	**D′**	**R²**
Triaxial compression	Path 1.1	5.03	29.9	0.985	4.28	19.6	0.987
	Path 1.2	4.31	19.3	0.977	3.43	16.1	0.981
Polyaxial compression	Path 2.1	3.38	12.1	0.989	3.24	10.3	0.995
	Path 2.2	3.08	9.16	0.992	2.56	8.35	0.997
Triaxial extension	Path 3.1	2.68	7.54	0.991	2.38	4.91	0.994
	Path 3.2	2.47	3.55	0.992	1.70	2.82	0.995

6.6 Distortional strain energy density - Lode parameter criteria

To determine the effect of the stress path on the salt strength the applied distortional strain energy density are fitted as a function of Lode parameter (μ) for varied mean strain energy density (Figures 6.7 and 6.8). The italic numbers in their figures represent the magnitudes of mean strain energy density (W_m) where their locations in the diagram indicate the corresponding magnitudes of Lode parameter and distortional strain energy density at failure (W_d) and at dilation ($W_{d,d}$). Interpolation between these W_m points allows derivation of the $W_{d,d}$ and W_d as a function of μ under selected of W_m (20, 30, 40, 50 and 60 kPa), which can be best represented a set of linear equations:

$$W_d = \chi \cdot \mu + \omega \tag{6.18}$$

$$W_{d,d} = \chi' \cdot \mu + \omega' \tag{6.19}$$

where χ, χ', ω and ω' are mean strain energy density multipliers and distortional strain energy density constants for the salt at failure and at dilation, respectively. They are empirically defined as a function of W_m as follows:

$$\chi = \chi_1 \cdot W_m + \chi_2 \tag{6.20}$$

$$\chi' = \chi'_1 \cdot W_{m,d} + \chi'_2 \tag{6.21}$$

$$\omega = \omega_1 \cdot W_m + \omega_2 \tag{6.22}$$

$$\omega' = \omega'_1 \cdot W_{m,d} + \omega'_2 \tag{6.23}$$

where χ_1, χ_2, χ'_1, and χ'_2 are the regression analysis constants of the Lode parameter multiplier for failure and dilation criteria. The parameters ω_1, ω_2, ω'_1, and ω'_2 are the regression analysis constant of distortional strain energy constant. Summary of these parameters are presented in Table 6.5.

By substituting parameters in the equations (6.20) through (6.23) into equations (6.18) and (6.19), the distortional strain energy at failure and dilation criteria of salt for σ_3 and σ_m constant conditions can be represented in the forms of the Lode parameter and mean strain energy density as follows:

$$W_d = (\chi_1 \cdot W_m + \chi_2) \cdot \mu + (\omega_1 \cdot W_m + \omega_2) \tag{6.24}$$

$$W_{d,d} = (\chi'_1 \cdot W_{m,d} + \chi'_2) \cdot \mu + (\omega'_1 \cdot W_{m,d} + \omega'_2) \tag{6.25}$$

The strain energy density criterion explicitly considers both octahedral shear stresses and strain. Hence it can describe the salt dilation as affected by stress paths more comprehensively than the criteria developed earlier.
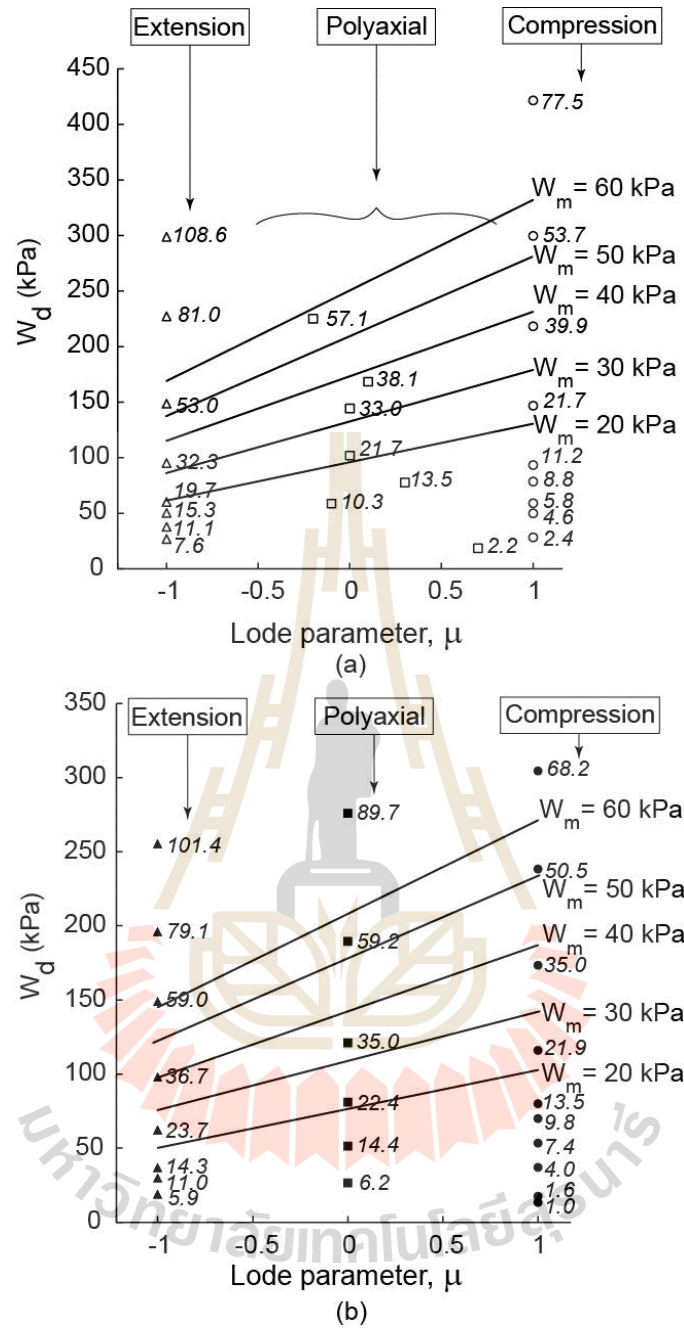
Figure 6.7 Distortional strain energy density at failure (W_d) as a function of Lode parameter (μ) for various mean strain energy density under σ_3 constant (a) and σ_m constant (b) condition. The numbers denote W_m in kPa for each data point.
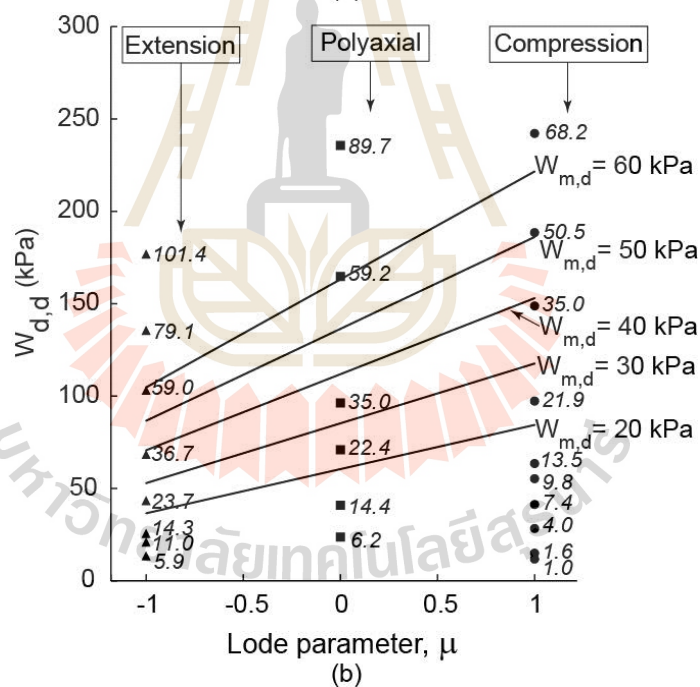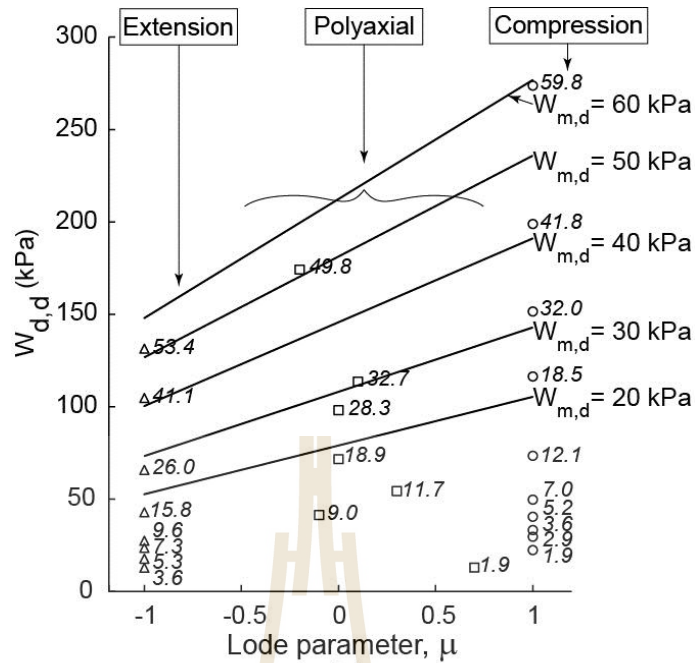
Figure 6.8 Distortional strain energy density at dilation ($W_{d,d}$) as a function of Lode

parameter (μ) for various mean strain energy density under σ_3 constant

(a) and σ_m constant (b) condition. The numbers denote $W_{m,d}$ in kPa for

each data point.

Table 6.5 Empirical constants for distortional strain energy density at failure and dilation criteria.

Stress conditions	At Failure					At Dilation				
	χ_1	χ_2	ω_1	ω_2	R^2	χ'_1	χ'_2	ω'_1	ω'_2	R^2
Constant σ_3	1.04	9.61	3.27	15.87	0.985	0.951	7.35	3.17	11.65	0.965
Constant σ_m	0.919	7.91	3.12	10.17	0.987	0.863	6.61	2.57	9.07	0.992

CHAPTER VII

DETERMINATION OF SAFE MINIMUM

STORAGE PRESSURES

7.1 Fundamental

The objective of this chapter is to demonstrate the mechanical stability evaluation of storage caverns in the Maha Sarakham salt, as affected by applying different strength and dilation criteria developed in the previous chapter. Two simplified geometry and boundary and loading conditions are used: cylindrical cavern and spherical cavern. The factor of safety under different internal (minimum) storage pressures are calculated. Relevant analytical or closed-form solutions are applied to determine the stress distribution around the openings.

7.2 Boundary and loading conditions

The two criteria are used here to calculate the factor of safety (FS) of the salt at the wall of the cavern. These include τ_{oct} - μ criterion and W_d – μ criterion. The cavern shape discussed here are spherical and cylindrical shapes. They are located at a depth of 500 m. The cavern configurations, depth and site geology used here represent a preliminary design of CAES cavern in the Khorat basin in the northeast of Thailand. The in-situ stress is assumed to be hydrostatic. Before cavern development the salt stress at the casing shoe depth (σ_{cs}), is defined as:

$$\sigma_{cs} = \gamma_r \cdot h \qquad (7.1)$$

where γ_r is specific unit weight of rock salt (21.6 kN/m^3) adopted from the testing results in chapter V, *h* is depth of overburden. The maximum cavern pressure is defined as 90% of σ_{cs}. Three cases with different uniform minimum pressures that are commonly used for the salt storage cavern are studied: 10%, 20% and 30% of σ_{cs}. Each case is simulated for the two different cavern shapes. The input parameters for calculation are given in Table 7.1.

Table 7.1 Rock salt properties and loading parameters used in calculations.

Parameters	Values
Shear modulus, G (GPa)	7.44
Bulk modulus, K (GPa)	28.4
Salt unit weight (kN/m^3)	21.6
In-situ stress at depth of 500 m, σ_{cs} (MPa)	10.8
P_i at 30% σ_{cs} (MPa)	3.24
P_i at 30% σ_{cs} (MPa)	2.16
P_i at 30% σ_{cs} (MPa)	1.08

7.3 Stress distribution around storage caverns

7.3.1 Cylindrical cavern

A cylindrical cavern of radius (a), is placed in a homogeneous, isotropic, initially elastic salt mass subjected to a uniform stress field, P_0. The cavern wall is supported by a internal pressure P_i. On the cavern boundary, the salt is in the polyaxial stress state where $\sigma_1 \neq \sigma_2 \neq \sigma_3 \neq 0$, as shown in Figure 7.1. In the Figure, σ_θ is the maximum principal (tangential) stress, σ_z is the intermediate principal stress and is often equal to the vertical in-situ stress along the cavern axis, and σ_r is
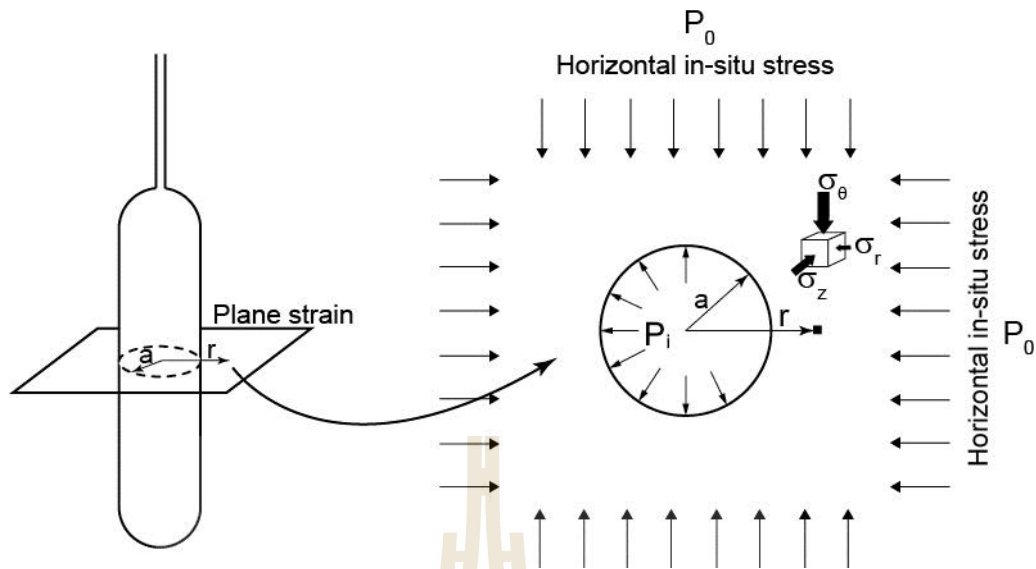
Figure 7.1 Stresses at wall of cylindrical cavern in an infinite rock mass.

the minimum principal (radial) stress. They can be calculated by using Kirsch solution (Brady and Brown, 1985):

$$\sigma_r = (1 - \frac{a^2}{r^2})\frac{(P_x + P_y)}{2} + (1 + 3\frac{a^4}{r^4} - 4\frac{a^2}{r^2})\frac{(P_x - P_y)}{2}\cos 2\theta \qquad (7.2)$$

$$\sigma_\theta = (1 + \frac{a^2}{r^2})\frac{(P_x + P_y)}{2} - (1 + 3\frac{a^4}{r^4})\frac{(P_x - P_y)}{2}\cos 2\theta \qquad (7.3)$$

$$\sigma_z = P_z - (4\nu\frac{a^2}{r^2})\frac{(P_x - P_y)}{2}\cos 2\theta \qquad (7.4)$$

For the uniform stress field assumed here $P_x = P_y = P_z = P_0$:

$$\sigma_r = \sigma_3 = P_0(1 - \frac{a^2}{r^2}) \qquad (7.5)$$

$$\sigma_\theta = \sigma_1 = P_0 (1 + \frac{a^2}{r^2}) \qquad (7.6)$$

$$\sigma_z = \sigma_2 = P_0 \qquad (7.7)$$

where σ_r is radial stress, σ_θ is tangential stress, and σ_z is stress along the cavern axis. In this case, the stress components at the wall (r=a) are calculated and assumed that the salt mass subjects to a hydrostatic stress (P_0). The effect of any internal radial pressure (P_i) acting in the hole can be taken into accounted by adding

$$\sigma_r = \sigma_3 = P_i \frac{a^2}{r^2} \; ; \qquad \sigma_\theta = \sigma_1 = -P_i \frac{a^2}{r^2}$$

The calculation results for the selected minimum pressures in terms of the octahedral shear stress $(\tau_{oct,cs})$ and distortional strain energy $(W_{d,cs})$ at the cavern wall of cylindrical cavern are summarized in Table 7.2.

Table 7.2 Stresses and strain energy density calculation results of cylindrical cavern wall for various the internal pressure (P_i) at depth of 500 m.

Internal pressure (P_i)	σ_1 (MPa)	σ_2 (MPa)	σ_3 (MPa)	$\tau_{oct,cs}$ (MPa)	$W_{d,cs}$ (kPa)
10% of σ_{cs}	20.5	10.8	1.08	7.93	13.81
20% of σ_{cs}	19.3	10.8	2.16	6.69	11.56
30% of σ_{cs}	18.2	10.8	3.24	5.78	9.98

7.3.2 Spherical cavern

A spherical cavern with radius (a) is assumed in a homogeneous infinite infinite isotropic salt mass subjected to a hydrostatic stress P_0, as shown in Figure 7.2. An internal pressure P_i uniformly acts on the cavern surface after the excavation. Due to the symmetry of the problem, the stress are only the functions of radius (r). The analytical solution of tangential (σ_θ) and radial (σ_r) can be obtained by (Hoek and Brown, 1980):

$$\sigma_r = \sigma_3 = P_0 - (P_0 - P_i)(\frac{a^3}{r^3}) \tag{7.8}$$

$$\sigma_\theta = \sigma_1 = P_0 + (P_0 - P_i)(\frac{a^3}{2r^3}) \tag{7.9}$$

where P_0 is the hydrostatic pressure at the casing shoe, P_i is minimum internal gas pressure maintain in the cavern. In this case the stress components are calculated at the cavern wall (r=a). The stress caomponents on the cavern boundary are subject to triaxial extension stress condition. Therefore, the tangential stress represents σ_1 and σ_2, and the radial stress is represents the minor principal stress (σ_3). The calculation results for the selected minimum pressures (P_i is 10%, 20% and 30% of σ_{cs}) in terms of octahedral shear stress and distortional strain energy at the cavern wall are summarized in Table 7.3.
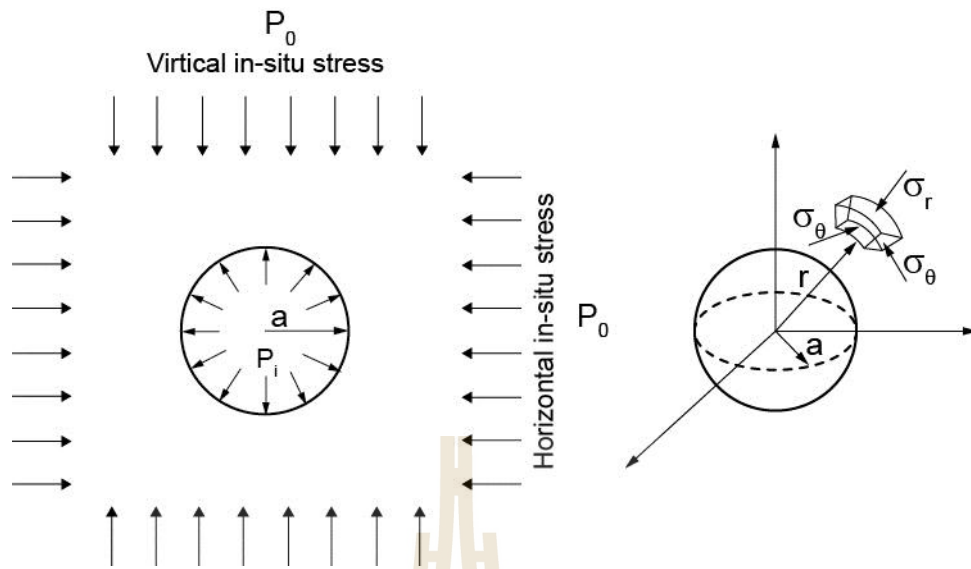
Figure 7.2 Spherical cavern in an infinite salt mass.

Table 7.3 Stresses and strain energy density calculation results at the wall of cavern

for various internal pressure (Pᵢ) at depth of 500 m.

Internal pressure (Pᵢ)	σ_θ (MPa)	σ_r (MPa)	$\tau_{oct,cs}$ (MPa)	$W_{d,cs}$ (kPa)
10% of σ_{cs}	15.6	1.08	7.36	8.86
20% of σ_{cs}	15.1	2.16	5.24	6.22
30% of σ_{cs}	14.5	3.24	4.01	4.76

7.4 Factors of safety calculation

The factor of safety (FS) is used for assessing the stability of cylindrical and spherical caverns. It is defined as the ratio of the maximum strength of material to stress occurring in it. This definition of the factor of safety is used to evaluate stability of the cavern wall. In this study, the $\tau_{oct,f}$ and $\tau_{oct,d}$ criterion is considered to estimate the FS under various magnitudes of Pᵢ as shown in Table 7.4 for both cavern shapes. From the results, the FS increases steadily with increasing the internal pressure. The criterion with

constant σ_3 gives higher value of FS than that of the criterion with constant σ_m. Most FS values from this criterion signify that the salt caverns still have a stability under various internal pressures at the depth of 500 m.

On the other hand, the FS calculated from the W_d - μ and $W_{d,d}$ - μ criterion gives more conservative results than those of octahedral shear criterion. The most conservative estimation of FS can be obtained by the $W_{d,d}$ - μ criterion. It shows the FS values lower than 1.0 when the internal pressure is less than 2.16 MPa (20% of σ_{cs}). The FS results for all internal pressures of the W_d and $W_{d,d}$ criteria are shown in Table 7.5.

For the conservative design the surrounding salt is not allowed to dilate during the operation period. Figure 7.3 compares the results of FS calculation for the cylindrical cavern calculated from different strength criteria at dilation. The results of FS on spherical storage cavern under different strength criteria at dilation are also presented in Figure 7.4. The FS as a function of P_i (% of σ_{cs}) for the dilation criteria are summarized in Table 7.6. The comparison indicates that the $W_{d,d}$ - μ criterion with constant σ_m provides the most conservative result. The safe minimum internal pressure is 30% of σ_{cs} for cylindrical cavern and 20% for spherical cavern.

Table 7.4 Factors of safety at cavern wall based on $\tau_{oct,f}$ - μ and $\tau_{oct,d}$ - μ criterion.

Cavern shapes	Internal pressure (P_i)	FS = $\tau_{oct,f}$ / $\tau_{oct,cs}$		FS = $\tau_{oct,d}$ / $\tau_{oct,cs}$	
		constant [σ_3]	constant [σ_m]	constant [σ_3]	constant [σ_m]
Cylindrical cavern	10% of σ_{cs}	1.31	1.16	1.12	0.96
	20% of σ_{cs}	1.55	1.38	1.33	1.14
	30% of σ_{cs}	1.79	1.59	1.54	1.32
Spherical cavern	10% of σ_{cs}	1.85	1.46	1.56	1.31
	20% of σ_{cs}	2.60	2.05	2.19	1.84
	30% of σ_{cs}	3.40	2.68	2.87	2.41

Table 7.5 Factors of safety at cavern wall based on W_d - μ and $W_{d,d}$ - μ criterion.

| Cavern shapes	Internal pressure (P_i)	FS = W_d / $W_{d,cs}$		FS = $W_{d,d}$ / $W_{d,cs}$	
		constant [σ_3]	constant [σ_m]	constant [σ_3]	constant [σ_m]
Cylindrical cavern	10% of σ_{cs}	0.97	0.83	0.81	0.72
	20% of σ_{cs}	1.16	0.99	0.96	0.86
	30% of σ_{cs}	1.34	1.15	1.12	1.00
Spherical cavern	10% of σ_{cs}	1.23	0.76	1.00	0.67
	20% of σ_{cs}	1.75	1.09	1.42	1.00
	30% of σ_{cs}	2.29	1.42	1.85	1.25
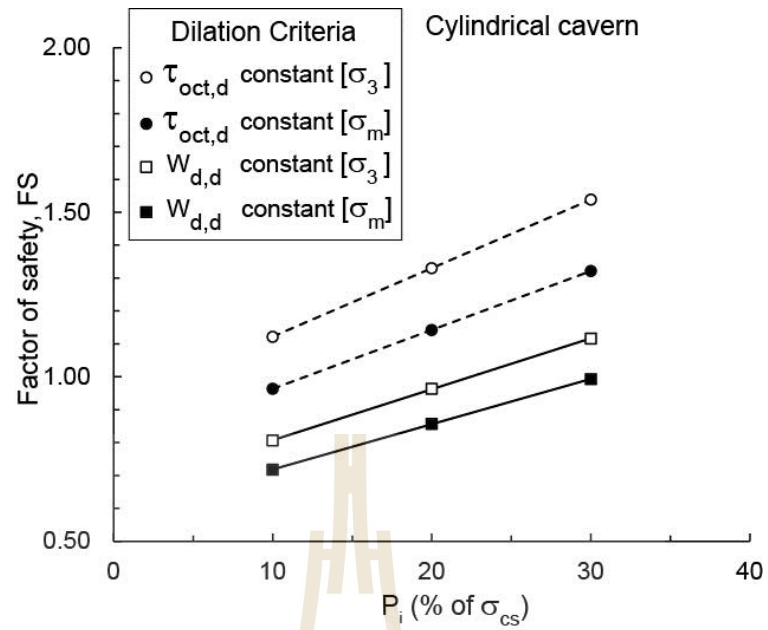
Figure 7.3 Factors of safety (FS) for cylindrical cavern as a function of internal pressure (P_i) for different strength criteria at dilation.
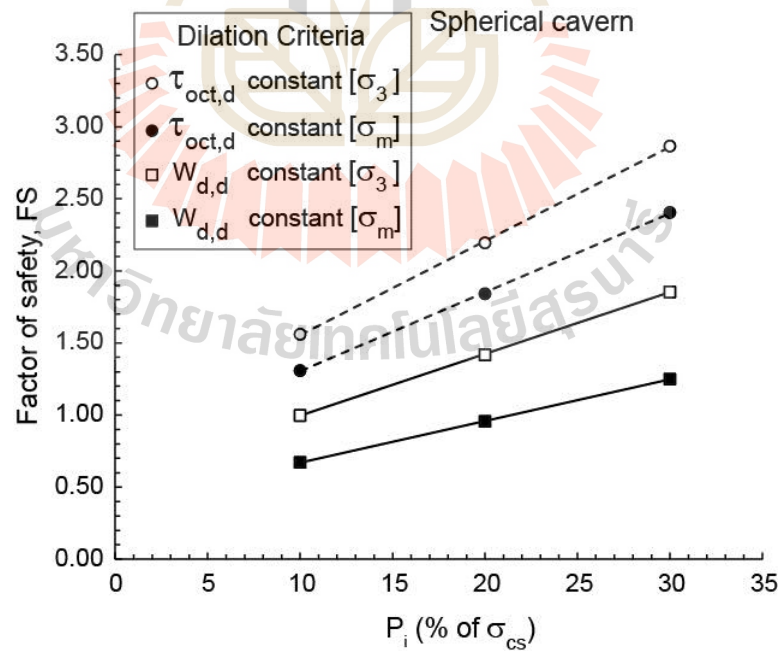
Figure 7.4 Factors of safety (FS) for spherical cavern as a function of internal pressure (P_i) for different strength criteria at dilation.

Table 7.6 Summary of FS as a function of P_i (% of σ_{cs}) for dilation criteria.

Cavern shapes	Dilation criteria	Conditions	FS
Cylindrical cavern	$\tau_{oct,d}$ - μ	Constant [σ_3]	FS = 0.0208P_i + 0.913
		Constant [σ_m]	FS = 0.0179P_i + 0.784
	$W_{d,d}$ - μ	Constant [σ_3]	FS = 0.0155P_i + 0.652
		Constant [σ_m]	FS = 0.0138P_i + 0.580
Spherical cavern	$\tau_{oct,d}$ - μ	Constant [σ_3]	FS = 0.0653P_i + 0.901
		Constant [σ_m]	FS = 0.0548P_i + 0.756
	$W_{d,d}$ - μ	Constant [σ_3]	FS = 0.0429P_i + 0.566
		Constant [σ_m]	FS = 0.0289P_i + 0.381

7.5 Evaluation of minimum storage pressures

From the previous section the $W_{d,d}$ - μ with constant σ_m criterion is the most conservative approach used in stability analysis. Using this strength criterion for the FS calculation should provide the lower values of FS than other strengths criteria. This section demonstrates the safe minimum storage pressures for CAES at various depths from ground surface: 300 m, 500 m, 800 m, and 1200 m. Both cavern shapes are used. The stresses, distortional strain energy density, and FS around these openings are summarized in Table 7.7 for the cylindrical cavern and in Table 7.8 for the spherical cavern. Figures 7.6 and 7.7 Plot the FS values as a function of cavern depths (measured at the casing shoe). As the depth increases the safe minimum storage pressures increase, which suggests that the salt strength do affect the designed minimum storage pressures of the salt caverns.

Table 7.7 Summary results of cylindrical cavern for various depth and the internal

pressure (P_i).

Depths (m)	P_i (MPa)	σ_1 (MPa)	σ_2 (MPa)	σ_3 (MPa)	$W_{d,cs}$ (kPa)	$W_{d,d}$ (kPa)	FS
300	0.65	12.30	6.47	0.65	2.29	3.84	1.67
	1.29	11.65	6.47	1.29	1.81	3.84	2.12
	1.94	11.01	6.47	1.94	1.39	3.84	2.76
	2.59	10.36	6.47	2.59	1.02	3.84	3.76
	3.24	9.71	6.47	3.24	0.71	3.84	5.42
500	1.08	20.50	10.79	1.08	6.37	5.01	0.79
	2.16	19.42	10.79	2.16	5.04	5.01	1.00
	3.24	18.34	10.79	3.24	3.86	5.01	1.30
	4.32	17.27	10.79	4.32	2.83	5.01	1.77
	5.40	16.19	10.79	5.40	1.97	5.01	2.55
800	1.73	32.80	17.27	1.73	16.31	7.88	0.48
	3.45	31.08	17.27	3.45	12.89	7.88	0.61
	5.18	29.35	17.27	5.18	9.87	7.88	0.80
	6.91	27.62	17.27	6.91	7.25	7.88	1.09
	8.63	25.90	17.27	8.63	5.04	7.88	1.56
1200	2.59	49.21	25.90	2.59	36.71	13.75	0.37
	5.18	46.62	25.90	5.18	29.00	13.75	0.47
	7.77	44.03	25.90	7.77	22.21	13.75	0.62
	10.36	41.44	25.90	10.36	16.31	13.75	0.84
	12.95	38.85	25.90	12.95	11.33	13.75	1.21

Table 7.8 Summary results of spherical cavern for various depth and the internal

pressure (P_i).

Depths (m)	P_i (MPa)	σ_1 (MPa)	σ_2 (MPa)	σ_3 (MPa)	$W_{d,cs}$ (kPa)	$W_{d,d}$ (kPa)	FS
300	0.65	9.39	9.39	0.65	1.72	2.68	1.56
	1.29	9.06	9.06	1.29	1.36	2.68	1.97
	1.94	8.74	8.74	1.94	1.04	2.68	2.57
	2.59	8.42	8.42	2.59	0.76	2.68	3.50
	3.24	8.09	8.09	3.24	0.53	2.68	5.04
500	1.08	15.65	15.65	1.08	4.78	3.67	0.77
	2.16	15.11	15.11	2.16	3.78	3.67	0.97
	3.24	14.57	14.57	3.24	2.89	3.67	1.27
	4.32	14.03	14.03	4.32	2.12	3.67	1.73
	5.40	13.49	13.49	5.40	1.48	3.67	2.49
800	1.73	25.04	25.04	1.73	12.24	6.09	0.50
	3.45	24.17	24.17	3.45	9.67	6.09	0.63
	5.18	23.31	23.31	5.18	7.40	6.09	0.82
	6.91	22.45	22.45	6.91	5.44	6.09	1.12
	8.63	21.58	21.58	8.63	3.78	6.09	1.61
1200	2.59	37.55	37.55	2.59	27.53	11.07	0.40
	5.18	36.26	36.26	5.18	21.75	11.07	0.51
	7.77	34.96	34.96	7.77	16.65	11.07	0.66
	10.36	33.67	33.67	10.36	12.24	11.07	0.90
	12.95	32.37	32.37	12.95	8.50	11.07	1.30
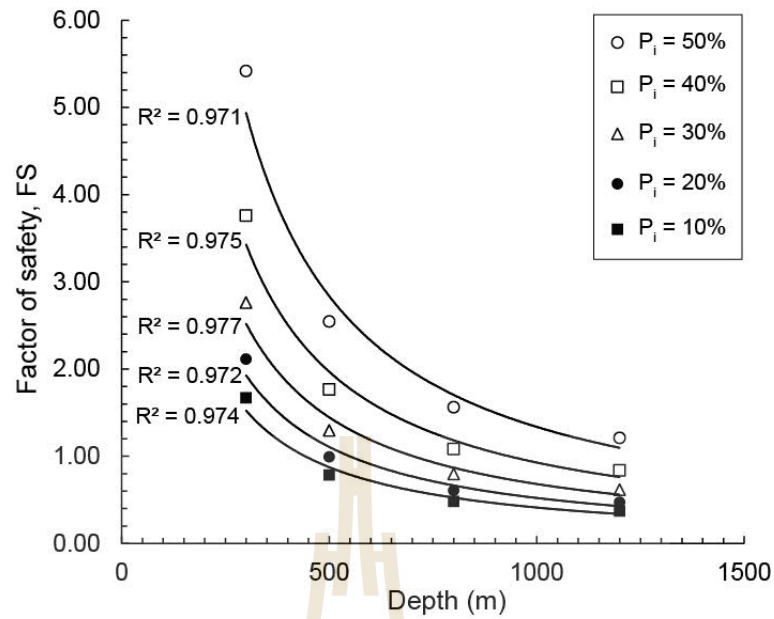
Figure 7.5 Factors of safety (FS) of cylindrical cavern as a function of cavern depths

for different storage pressures (P_i).
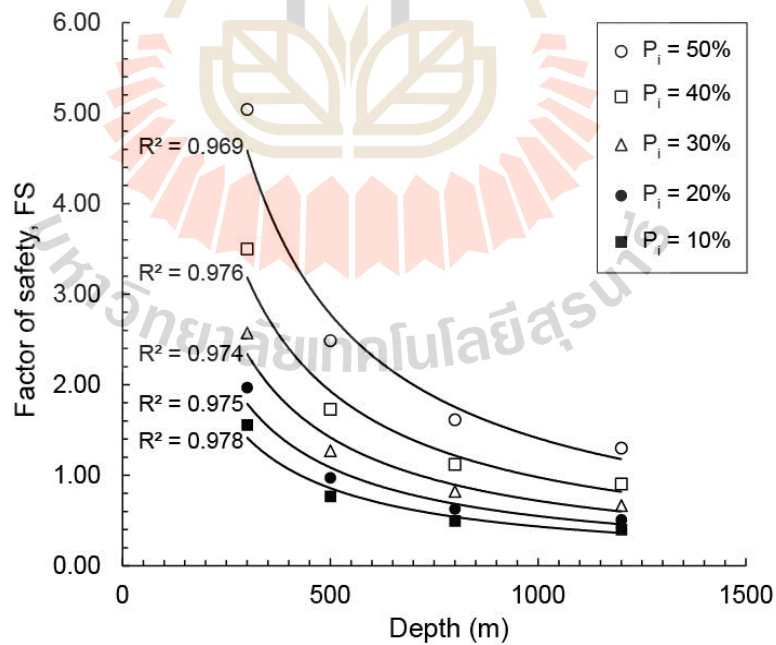
Figure 7.6 Factors of safety (FS) of spherical cavern as a function of cavern depths

for different storage pressures (P_i).

CHAPTER VIII

DISCUSSIONS, CONCLUSIONS AND

RECOMMENDATIONS FOR FUTURE STUDIES

8.1   Discussions

This section discusses the key issues relevant to the reliability of the test schemes and the adequacies of the test results. Comparisons of the results and findings from this study with those obtained elsewhere under similar test conditions have also been made.

- The numbers of the test specimens seem adequate, as evidenced by the good coefficients of correlation for all test schemes and stress paths. The minimum magnitudes of the σ_3 and σ_m are limited by the capability of the true triaxial test frame. The minimum magnitudes are governed by the salt mechanical properties that relate to the maximum difference between the major and intermediate and/or minor principal stresses at failure.

- The test results in terms of the stress-strain relations and strengths are believed to be reliable. They are agreed reasonably well with the related test results on the Maha Sarakham salt obtained by Sriapai et al. (2013) and Sartkaew (2013).

- A difficulty is the controlling the increases and decreases of the applied principal stresses to obtain the desired test schemes and stress paths. High precision pressure transducers and electronic displacement gages are used here while the pressures in the hydraulic load cells are manually controlled.   Results of the

specimens that are subjected to the stresses that deviate for the designed schemes have been discarded.

- The strengths and strain energy densities required to fail the specimens for the condition of constant σ_3 are always greater than those under constant σ_m condition. This is true for all test schemes and confinements.

- The specimens size used in this study are relatively small. Recognizing the size effects on the rock strengths (Jaeger et al., 2007), larger specimens should be used. In summary the strengths obtained here under all test schemes would overestimate the strength of the salt under in-situ condition due to the scale effect. Nevertheless, the issue of the size effect would not change the main conclusions drawn here that the salt strengths increase with the Lode parameter and that salt loaded under constant σ_3 condition would yield greater compressive strength than that under constant σ_m condition.

- The loading rate used in this study is relatively high as compared to those of the salt around the storage caverns. The loading rate here complies with that of the ASTM (D7012-04) standard practice (0.1 MPa/s). It is recognized that rock under high loading rate would give higher strength and stiffness than that under lower loading rates (Kumar, 1968; Jaeger and Cook, 1979; Farmer, 1983; Cristescu and Hunsche, 1998; Fuenkajorn et al., 2012). As a results the salt strengths and their corresponding criteria derived here may also over-estimate those of the in-situ salt where it is likely to subject to much lower loading rates.

- It should be note that the effects of temperatures have not been considered to determine the safe minimum storages pressure in the previous section. It has been recognized that the temperature can decrease the salt strengths (Hansen and Carter,

1980; Liang et al., 2006; Fuenkajorn et al., 2012). The calculation of the factor of safety presented here is under ambient and isothermal condition. The results may therefore overestimate the salt strengths around the storage cavern if it is subject to elevated temperatures resulting from the fluctuation of the cavern pressures during operation.

- The strain energy density determined here is by assuming that the stress-strain relations are linear. In reality, however, non-linear behavior has been observed for all test schemes and stress paths, in particular for the salt under large σ_3 and σ_m magnitudes. As a result the strain energy determined here is likely to underestimate the energy that the in-situ salt can absorb before dilation and failure. This makes the application of the strain energy criterion to the stability evaluation even more conservative.

- The advantage of the application of the stain energy criterion over the octahedral shear-mean stress criterion is that it considers both stress and strain at failure, and hence their results would be more comprehensive than the octahedral shear-mean stress criterion.

- The effect of σ_2 on the salt strength are obvious as explicitly shown by octahedral shear strength-Lode parameter relation (see Figures 6.2 and 6.3) and by the strain energy density at failure-Lode parameter relation (see Figure 6.7). The increase of σ_2 results in a reduction of the salt strength, which agrees with the experimental results obtained by Mogi (1967), Handin, et al. (1967), Furuzumi and Sugimoto (1986), Takahashi and Koide(1989), Kwasniewski and Mogi (1990), Pobwandee (2010) and Komenthammasopon (2014). This is true for both constant σ_3 and constant σ_m loading conditions. A possible explanation is that when the salt is subject

to high principal stresses in two direction, it tends to dilate and eventually create extension failure with the fracture planes parallel to those two directions.

- For the stress path issues, it is clear from the test results that under constant σ_m condition the salt tends to fail easier than when it is under constant σ_3 condition. This could be explained by that when the σ_2 and/or σ_3 decrease as the σ_1 increases the salt can dilate along the σ_2 and/or σ_3 directions easier than when it is subject to constant confinement while σ_1 is increased. Note that the constant σ_m condition is likely to be the same with the conditions imposed on the rock salt when a mine opening or cavern is developed.

- The proposed criteria (both octahedral shear stress and strain energy density) are capable of determination of the safe minimum storage pressures in the salt cavern. It is not intended here that the dilation associated criteria are better than the strength criteria. Depending on the site-specific requirements and load regulations, the safe minimum storage pressures may be defined by any criteria. Design consideration used in the storage industry normally include both long-term mechanical stability and storage capacity.

- Calculation of the FS for the cylindrical and spherical caverns clearly indicates that the stress distribution around the caverns in salt mass is likely to be polyaxial compression and triaxial extension rather than triaxial compression as used in the conventional laboratory test scheme. This enhances the significance of the loading configurations in the laboratory that should represent the actual in-situ conditions, such as polyaxial and triaxial extension as performed in the study.

8.2   Conclusions

All objectives and requirements of this study have been met. The results of the laboratory testing and analyses can be concluded as follows:

- The effect of stress path on the rock salt strength can be observed from the relations of the octahedral shear stresses as a function of mean stresses (Figure 5.9). it can reduce the salt strength when the salt subjects to constant mean stress condition.

- Under the same mean stress, the octahedral shear strengths obtained from triaxial compression are largest while the triaxial extension yields the lowest values. This is true for both under constant σ_3 and constant σ_m conditions.

- The direction of fracture plane on the tested specimen trends to be parallel to the σ_2 direction, particularly under high σ_2 and low σ_3 magnitudes. This behavior is supported by the post-test observations on the specimens that the triaxial extension specimens fails easier than those triaxial compression specimens. (see Figure 5.10).

- This study proposed two empirical strength criteria, octahedral shear strength-Lode parameter and distortional strain energy-Lode parameter. Both criteria can predict the salt strength under various stress conditions by substituting the Lode parameter value (see equation 6.1) into the criteria. The strain energy criterion is more conservative as it considers both stresses and strain at failure. Nevertheless, derivation of the strain energy criterion requires a more comprehensive measurements of the stress and strain at failure or at dilation during the laboratory testing.

- The proposed criteria can be applied to conservatively determine the safe minimum storage (cushion) pressure of the CAES, LPG and natural gas caverns.

8.3   Recommendations for future studies

- Larger specimen size should be used to enhance the representativeness of the test results. This is invoked by the scale effect that that normally occurs when laboratory test results are applied to the in-situ conditions.

- The results under the polyaxial compression tests should be obtained under the broader range of the Lode parameter, i.e. from −1 to +1. This will provide a more rigorous calibration of the empirical constants used in various criteria proposed here.

- The effect of temperature should assessed in the laboratory.   The specimens should be test under the range of temperatures expected to occur in the salt around the openings.

- The proposed criteria may be incorporated into numerical code, and hence the factor of safety of the salt domain can be determined directly through there algorithm of the program. In another word the salt strengths automatically calculated at individual points around the salt caverns.

- Different loading rates should be used in the test to assess the rate-dependent strength of the salt. The loading rate effects should explicitly include in the strength criteria.

- Verification of the accuracy of the proposed criteria should be made by comparing with the actual salt cavern stability.

REFERENCES

Alassi, H. T. I, Li L., Holy, R. M. (2006) Discrete element modeling of stress and strain evolution within and outside a depleting reservoir. **Pure Appl Geophys** 163: 199-209

Alexeev, A.D., Revva, V.N., Alyshev, N.A., and Zhitlyonok, D.M. (2004). True triaxial loading apparatus and its application to coal outburst prediction. **International Journal of Coal Geology.** 58(4): 245-250.

Alexeev, A.D., Revva, V.N., and Bachurin L. L. (2008). The effect of stress state factor on fracture of sandstones under true triaxial loading. **Int. J. Fract**. 149: 1-10.

Boker, R. (1915). The mechanics of the permanent shape change in crystalline built Korpern. **Ver. dtsch. Ing. Mitt. Forsch**. 175: 1- 51.

Cai, M. (2008). Influence of stress path on tunnel excavation response—Numerical tool selection and modeling strategy. **Tunnelling and Underground Space Technology.** 23: 618-628.

Cai, M., (2008). Influence of stress path on tunnel excavation response—numerical tool selection and modeling strategy. **Tunnelling and Underground Space Technology**. 23: 618–628.

Chang, C., and Haimson, B. (2005). Non-dilatant deformation and failure mechanism in two Long Valley Caldera rocks under true triaxial compression. **International Journal of Rock Mechanics and Mining Sciences.** 42: 402-414.

Colmenares, L.B., and Zoback, M.D. (2002). A statistical evaluation of intact rock failure criteria constrained by polyaxial test data for five different rocks. **International Journal of Rock Mechanics and Mining Sciences**. 39: 695-729.

Crouch, S.L. (1972). A note on post-failure stress–strain path dependence in norite. **International Journal of Rock Mechanics and Mining Sciences**. 9 (2): 197–204.

Eberhardt, E. (2001). Numerical modelling of three-dimension stress rotation ahead of an advancing tunnel face. **Int J Rock Mech Min Sci**. 38: 499–518

Ferfera, F.M.R., Sardau, J.P., and Bouteca, M. (1997). Experimental study of monophasic permeability changes under various stress paths. **International Journal of Rock Mechanics and Mining Sciences**. 34 (3–4) (paper No. 037).

Fuenkajorn, K., Sriapai, T. and Samsri, P. (2012). Effects of loading rate on strength and deformability of Maha Sarakham salt. **Engineering Geology** 135-136: 10-23.

Furuzumi, M. and Sugimoto, F. (1986). Effect of intermediate principal stress on failure of rocks and failure condition of rock under multiaxial stress. **J. Jpan Soc. Eng. Geol**. 27(1): 13-20. (in Japanese)

Haimson, B. (2006). True triaxial stresses and the brittlef of rock. **Pure and Applied Geophysics.** 163: 1101-1113.

Haimson, B., and Chang, C. (2000). A new true triaxial cell for testing mechanical properties of rock, and its use to determine rock strength and deformability of Westerly granite. **International Journal of Rock Mechanics and Mining Sciences** 37: 285-296.

Haimson, B., and Chang, C. (2002). True triaxial strength of the KTB amphibolite under borehole wall conditions and its use to estimate the maximum horizontal in situ stress. **J. Geophys. Res**. 107(B10): 2257.

Handin, J., Heard, H.C., and Magouirk J.N. (1967). Effects of the intermediate principal stress on the failure of limestone, dolomite and glass at different temperatures and strain rates. **J. Geophys. Res**. 72: 611--640.

Handin, J., Heard, H.C., and Magouirk J.N. (1967). Effect of intermediate principal stress on the failure of lime stone, dolomite and glass at different temperatures and strain rates. **J. Geophys. Res**. 72:611-640.

Handin, J., Heard, H.C., and Magouirk, J.N. (1967). Effect of the intermediate principal stress on failure of limestone, dolomite, and glass at different temperature and strain rate. **Journal of Geophysical Research.** 72(2): 611-640.

He, M., Miao, J., Li, D., and Wang, C. (2007). Experimental study on rockburst processes of granite specimen at great depth. **Chinese J. Rock Mech. Engng**. 26(5): 865-876. (in Chinese)

Hoek, E., and Franklin, J.A., (1970). Developments in triaxial testing equipment. **Rock Mechanics.** 2: 223-228.

Holt R.M., Brignoli M., Kenter C.J., (2000). Core quality: quantification of coring-induced rock alteration. Int J Rock Mech Min Sci 37: 889–907

Hoskins, E.R. (1969). The failure of thick-walled hollow cylinders of isotropic rock. **Int. J. Rock Mech. Min. Sci**. 6: 99- 125.

Jaeger, J.C., and Cook, N.G.W. (1979). Fundamentals of Rock Mechanics (3rd. Edn.), Chapman & Hall, London, pp. 105-106.Kaiser P.K., Yazici S., Maloney

S., (2001). Mining-induced stress change and consequences of stress path on excavation stability – a case study. **Int J Rock Mech Min Sci**. 38: 167–180

Karman, T., (1911). Festigkeitsversuche unter allseitigem. **Ver. dtsch. Ing**. 55: 1749- 1757.

King, M.S., Chaudhry, N.A., and Shakeel, A. (1995). Experimental ultrasonic velocities and permeability for sandstone with aligned cracks. **Int. J. Rock Mech. Min. Sci**. 32: 155- 163.

Kulatilake, P.H., Park, J., and Malama, B., (2006). A new rock mass failure criterion for biaxial loading conditions. **Geotechnical and Geological Engineering.** 24: 871-888.

Kwasniewski, M., Takahashi, M., and Li, X. (2003). Volume changes in sandstone under true triaxial compression conditions. **ISRM 2003–Technology Roadmap for Rock Mechanics.** South African Institute of Mining and Metallurgy. pp. 683-688.

Kwasniewski, M.A. and Mogi, K. (1990). Effect of intermediate principal stress on the failure of a foliated rock. In **H.-P. Rossmanith (ed), Mechanics of Jointed and Faulted Rock**, pp. 407-416. Rotterdam: Balkema.

Kwasniewski, M.A., and Mogi, K. (1990). Effect of the intermediate principal stress on the failure of a foliated rock. In H.-P. Rossmanith (ed.), **Mechanics of Jointed and Faulted Rock**, pp. 407-416. Rotterdam: Balkema.

Lavrov A (2005). Fracture-induced physical phenomena and memory effects in rocks: a review. Strain 41: 135–149

Lavrov A, Vervoort A, Wevers M, Napier JAL (2002). Experimental and numerical study of the Kaiser effect in cyclic Brazilian tests with disk rotation. **Int J Rock Mech Min Sci**. 39: 287–302

Lee, D. H., Juang C.H., Chen, J.W. (1999). Stress paths and mechanical behavior of a sandstone in hollow cylinder tests. **Int J Rock Mech Min Sci**. 36: 857–870

Lee, D.H., Juang, C.H., Chen, J.W., et al., (1999). Stress paths and mechanical behavior of a sandstone in hollow cylinder tests. **International Journal of Rock Mechanics and Mining Sciences**. 36, 857–870.

Li, x., and Xu, D. (1991). Incidence and rule of the mid-principal stress upon the rock strength. **Rock Soil Mech**. 12(1): 9-16. (in Chinese)

Lode, W. (1926). Versuche ueber den Einfluss der mittleren Hauptspannung auf das Fliessen der Metalle Eisen Kupfer und Nickel. **Mechanics. Port City Press**, **Baltimore**. pp. 3–57.

Mellegard, K. D., Devries, K. L., and Callahan, G. D. (2007). Lode angle effects on the creep of salt. **Proceeding of The 6th Conference on The Mechanical Behavior "SALTMECH6"**. Hannover, Germany. pp. 9-15.

Mogi, K. (1967). Effect of the intermediate principal stress on rock failure. **J. Geophys. Res**. 72: 5117-5131 .

Mogi, K. (1967). Effect of intermediate principal stress on rock failure. **J. Geophys. Res**. 72: 5117-5131.

Mogi, K. (1970). Effect of the triaxial stress system on rock failure. **Rock Mechanics in Japan**. 1: 53-55.

Mogi, K. (1971). Fracture and flow of rocks under high triaxial compression. **Journal of Geophysical Research.** 76: 1255- 1269.

Mogi, K. (2007). Experimental Rock Mechanics. Leiden: **Taylor and Francis/Balkema**.

Murrell, S.A.F. (1963). A criterion for brittle fracture of rocks and concrete under triaxial stress, and the effect of pore pressure on the criterion. **Proceedings 5th Symposium on Rock Mechanics** (pp. 563-577). Minnesota, USA.

Murrell, S.A.F. (1965). The effect of triaxial stress systems on the strength of rock at tmospheric temperatures. **Geophys. JR. Astr. Soc**. 10: 231-281. Niwa, Y., Koyanagi,

Rao, K.S., and Tiwari, R.P. (2004). Physical simulation of jointed model materials under biaxial and true triaxial stress states. **Research Report, IIT** Delhi, India, pp. 30.

Robertson, E.C. (1955). Experimental study of the strength of rocks. Bull. **Geol. Soc. Am**. 66: 1275- 1314.

Robertson, E.C. (1955). Experimental study of the strength of rocks. Bull. **Geol. Soc. Am**. 66: 1275- 1314.

Sartkaew, S., and Fuenkajorn, K. (2013). Efeect of stress rate on uniaxial compressive strength of rock salt under 0-100$^\text{o}$ C. **The 11$^\text{th}$ International Conference on Minerals and Petroleum Engineering**. pp 53-61.

Skoczylas, F., and Henry, J.P. (1995). A study of the intrinsic permeability of granite to gas. **Int. J Rock Mech. Min. Sci**. 32: 171- 179.

Sriapai, T., Samsri, P., and Fuenkajorn, K. (2011). Polyaxial strengths of Maha Sarakham salt. **Proceedings of the Third Thailand Rock Mechanics Symposium** (pp. 79-87). Nakhon Ratchasima, Thailand.

Sriapai, T., Walsri, C., and Fuenkajorn, K. (2012). Effect of temperature on compressive and tensile strengths of salt. **Science Asia**. 38: 166-174

Swanson, R.S., Brown, W.S., 1971. An observation of loading path independence of fracture in rock. **International Journal of Rock Mechanics and Mining Sciences**. 8 (3): 277–281.

Takahashi, M. and Koide, H. (1989). Effect of intermediate principal stress on strength and deformation behavior of sandstone and shale at depth shallower than 100m. Bull. **Geol. Survey Japan**. 40(40): 207-222. (in Japanese)

Takahashi, M., Narita, T., Tomishima, Y., and Arai, R. (2001). Various loading systems for rock true triaxial compression test. **J. Japan Soc. Eng. Geol**. 42(4): 242- 247. (in Japanese)

Takahashi, M., Sugita, Y., and Xue, Z. (1993). Three principal stress effects on permeability of Shirahama sandstoneIn case of stress state prior to dilatancy. **J Min. Mater. Proc. Inst**. Japan 109: 803- 808. (in Japanese)

Tiwari, R.P., and Rao, K.S. (2004). Physical modeling of a rock mass under a true triaxial stress state. **International Journal of Rock Mechanics and Mining Sciences**. 41(3).

Vernik, L., and Zoback M. D. (1992). Estimation of maximum horizontal principal stress magnitude from stress induced well bore breakouts in the Cajon Pass scientific research borehole. **J Geophys. Res**. 97: 5109- 5119.

Vervoort, A. (2003) Effect of tri-axial loading and unloading on fracturing of rock. **Proceedings of Rock Stress** (pp 479–484), Kumamoto, 4–6 November 2003, A.A.Balkema.

Walsri, C., Poonprakon, P., Thosuwan, R., and Fuenkajorn, K. (2009). Compressive and tensile strengths of sandstones under true triaxial stresses. **Proceedings of the Second Thailand Symposium on Rock Mechanics** (pp. 199-218). Chonburi, Thailand.

Walsri, C., Poonprakon, P., Thosuwan, R., and Fuenkajorn, K. (2009). Compressive and tensile strengths of sandstones under true triaxial stresses. **Proceedings of the Second Thailand Rock Mechanics Symposium** (pp. 199-218). Nakhon Ratchasima, Thailand.

Wang, B., Zhu, J.B., and Wu, A.Q. (2008). Experimental study on mechanical properties of Jinping marble under loading and unloading stress paths. **Chinese Journal of Rock Mechanics and Engineering**. 27 (10) : 2138–2145.

Wawersik, W.R., Carlson, L.W., Holcomb D. J., and Williams, R.J. (1997). New method for true-triaxial rock testing. **International Journal of Rock Mechanics and Mining Sciences.** 34(3): 365-365.

Wiebols, G.A., and Cook, N.G.W. (1968). An energy criterion for the strength of rock in polyaxial com pression. **International Journal of Rock Mechanics and Mining Sciences.** 5: 529-549.

Xu, D., and Geng, N. (1985). The variation law of rock strength with intermediate principal stress. **Acta Mech. Solida Sinica**, 6(1):72- 80. (in Chinese)

Xu, D., Zhang, G., and Li, T., Tham, L.G. and Tsui, Y. (2000). On the stress state in rock burst. **Chinese J Rock Mech. Engng**. 19(2): 169- 172. (in Chinese)

Xu, D.J., Geng, N.G. (1986). The various stress paths causing deformation and failure in

Yang, S.Q. (2013). Strength and deformation behavior of red sandstone under multi-stage triaxial compression. **Can. Geotech. J**. 49: 694–709

Yang, S.Q., Jing, H.W., Li, Y.S., Han, L.J. (2011). Experimental investigation on mechanical behavior of coarse marble under six different loading paths. **Experimental Mechanics**. 51 (3): 315–334.

Yang, S.Q., Jing, H.W., Wang, S.Y. (2012). Experimental investigation on the strength, deformability, failure behavior and acoustic emission locations of red sandstone under triaxial compression. **Rock Mechanics and Rock Engineering**. 45 (4): 583–606.

Yao, X.X., Geng, N.G., Chen, Y. (1980). The effect of stress path on brittleness and ductility of rocks. **Acta Geophysica Sinica** 23 (3): 312–319.

You, M. (2008). True-triaxial strength criteria for rock. **International Journal of Rock Mechanics and Mining Sciences.** 46: 115-127.

BIOGRAPHY

Mr. Kiattisak Artkhonghan was born on March 24, 1986 in Suphan Buri province, Thailand. He received his Bachelor's Degree in Engineering (Geotechnology) from Suranaree University of Technology in 2009. For him post-graduate, he continued to study with a Master's degree in the Geological Engineering Program, Institute of Engineering, Suranaree university of Technology. He achieved his Master Degree in Engineering (Geotechnology) in 2013. During graduation, 2009-2015, he was a part time worker in position of research assistant at the Geomechanics Research Unit, Institute of Engineering, Suranaree University of Technology.